UNIVERSITY OF LONDON THESIS

Degree phd Year 2007 Name of Author MARCUS CHRISTIAN NEWTON

Zinc Oxide Tetrapod Nanocrystal Diodes

Marcus Christian Newton

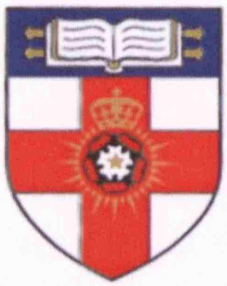

A dissertation submitted to University College London for the degree of Doctor of Philosophy.

Department of Electrical & Electronic Engineering
University College London
Torrington Place
London, WC1E 7JE
United Kingdom.

London Centre for Nanotechnology

University College London
Gordon Street
London, WC1H 0AH
United Kingdom.

April, 2007

ProQuest LLC
789 East Eisenhower Parkway
P.O. Box 1346
Ann Arbor, MI 48106-1346

Cultivate thy thought in thy early days.
Make thy body strong in thy early days.
Improve thy wisdom in thy early days.
Chain thy hope to the stars in thy early days.

Dr. Shigeyoshi Matsumae
(1901-1991)

"But you must continue in the things which you have learned and been assured of, knowing from whom you have learned them, and that from childhood you have known the Holy Scriptures, which are able to make you wise for salvation through faith which is in Christ Jesus."

2 Timothy 3:14-15

נֵר־לְרַגְלִי דְּבָרֶךָ וְאוֹר לִנְתִיבָתִי

"Thy word is a lamp unto my feet, and a light unto my path."

The acrostic psalm of David.

Acknowledgements

I would like to thank all those whose efforts have contributed to this work. To my fellow researchers, many of whom have sacrificed considerable time for this cause, I cannot thank you enough. In particular, I would like to thank Irving Ian Liaw. A truly great person is one who can see to the needs of others before those of himself.

Special thanks are given to Prof. Christopher Baker, Dr Steven Firth, Dr Tony Kenyon, Prof. Ian Boyd and Dr Mark Ellerby for their positive contributions and guidance.

I would also like to thank Dr Takashi Matsuura, Mr Kevin Lee, Mr Steven Etienne and Mr Michael Creswell for the continuing technical support that has made this work possible. Lastly I would like to thank Dr Paul Warburton who has supervised this work throughout, helped to motivate the study and shaped our perspective on scientific endeavour. For these things I am truly thankful.

I, Marcus Christian Newton, confirm that the work presented in this thesis is my own. Where information has been derived from other sources, I confirm that this has been indicated in the thesis.

Abstract

Advances in fabrication and analysis tools have allowed the synthesis and manipulation of functional materials with features comparable to fundamental physical length scales. Many interesting properties inherently due to quantum size effects have been observed in nanometre scale structures. It is hoped that these nanoscale structures will play a key role in future materials and devices that exploit their unique properties.

Zinc oxide (ZnO) is a wide band-gap transparent and piezoelectric semiconductor material. It also has a large exciton binding energy which allows for stable ultraviolet light emission at room temperature. There are therefore foreseeable applications in optoelectronic devices which include ultraviolet photosensitive devices and light emitting diodes.

Nanoscale structures formed from ZnO are intersting as they possess many of the properties inherent form the bulk but are also subject to various quantum size effects that may occur at the nanoscale. To date, the study of ZnO nanostructures is a relatively recent endevour with the vast majority of reports being made within the last five years. ZnO is unique in that it forms a family of nanoscale structures. These structures include nanoscale wires, rods, hexagons, tetrapods, ribbons, rings, flowers and helixes.

This work is focussed on the study of zinc oxide tetrapod crystalline nanoscale structures and their devices. We have synthesised ZnO tetrapods using chemical vapour transport techniques. Photoluminescence characterisation revealed the presence of optically active surface defects that could be quenched with a simple surface treatment. We have also for the first time observed resonant cavity modes in a single ZnO tetrapod nanocrystal.

An ultraviolet sensetive Schottky diode was fabricated from a single ZnO tetrapod using focussed ion-beam assisted deposition techniques. The device chracteristics observed were modelled and successfully shown to result from an illumination induced reduction in the Schottky barrier height at the metal-semiconductor interface.

Table of Contents

Literature Review and Technical Background on ZnO

List of Figures

List of Tables

List of Symbols

E = Electric field strength

D = Electric displacement

H = Magnetic field strength

B = Magnetic flux density

M = Magnetisation density

P = Polarisation density

J = Current density

ε = Dielectric tensor

ε_0 = Permittivity of free space

ρ = Charge density

μ_0 = Permeability of free space

J_n = Electron current density

J_p = Hole current density

n = Electron concentration

p = Hole concentration

μ_n = Electron mobility

μ_p = Hole mobility

D_i = Carrier diffusion coefficient

v_d = Drift velocity

G_n = Electron generation rate

G_p = Hole generation rate

U_n = Electron recombination rate

U_p = Hole recombination rate

τ_i = Excited carrier lifetime

Δn = Excited electron density

Δp = Excited hole density

E_g = Electronic band gap

E_{AB} = A-B valence band separation

E_{BC} = B-C valence band separation

m_e^* = Electron effective mass

m_h^* = Hole effective mass

μ_e = Electron hall mobility

W_F = Work Function

χ = Electron affinity

I = Ionisation energy

W_{bp} = Branch point energy

E_{ex}^b = Exciton binding energy

E_{xx}^b = Biexciton binding energy

a_{ex} = Exciton Bohr Radius

R_e = Electron polaron Radus

R_h = Hole polaron Radii

η = Refractive index

$\tilde{\alpha}$ = Polarisability

E_2^{low} = TO (E_2) phonon mode

E_2^{high} = LO (E_2) phonon mode

A_1^{LO} = LO (A_1) phonon mode

A_1^{TO} = TO (A_1) phonon mode

E_1^{LO} = LO (E_1) phonon mode

E_1^{TO} = TO (E_1) phonon mode

$FX_A^{n=1}$ = Free A-Exciton

$FX_B^{n=1}$ = Free B-Exciton

$FX_C^{n=1}$ = Free C-Exciton

ϕ = Potential

ϕ_{Bn} = Potential barrier height for n-type semiconductor

ϕ_{Bp} = Potential barrier height for p-type semiconductor

Q = Charge density per unit area

ρ = Charge density per unit volume

g_c = Density of states

L_{Th-F} = Thomas-Fermi screening length

L_D = Extrinsic Debye length

Literature Review and Technical Background on ZnO

1. Introduction

Zinc oxide (ZnO) is currently one of the most widely-studied compound semiconductor materials since either in its intrinsic state or when doped it can display a wide range of electronic, optical and magnetic properties. ZnO has wide band gap (3.37 eV) and large exciton binding energy (60 meV). The wide band gap makes ZnO a suitable material for ultraviolet optoelectronic applications making ZnO a competitor to gallium nitride, the well established industry standard. The large exciton binding energy is what, in principle, gives ZnO a fundamental advantage over GaN, since it suggests that stable excitonic stimulated emission should be achievable at room temperature.

Various crystalline nanoscale structures have shown unique and highly non-linear optical and electronic properties which can be related to quantum confinement effects. Exploiting these effects would allow a new generation of materials and devices to be made that bring with them many advantages over current state of the art. Examples of this are quantum-dot logic devices for information processing and polymer-nanocrystal light harvesting devices.

Another vibrant aspect of ZnO research is into nanoscale structures. This is partly due to the comparative ease with which ZnO forms crystalline nanostructures in a wide variety of geometries. These include nanorods, nanoribbons, nanoflowers and tetrapods. Such nanostructures are of particular interest since their dimensions can be commensurate with the wavelength of the ultraviolet emission corresponding to its wide band gap. In other words the nanocrystal can act as a self-assembled Fabry-Perot cavity.

This work is centred on the study of ZnO tetrapod nanocrystals and their devices. The aim is to study the electronic and optical properties of ZnO tetrapod nanocrystals. In doing this, devices based on a single ZnO tetrapod nanocrystal are fabricated. The study begins by reviewing the electronic and optical properties of bulk ZnO in chapters 2 and 3 with some key developments in the study of ZnO nanostructures. Chapters 4 and 5 review the properties of semiconductor surfaces and interfaces under illumination with particular emphasis on ZnO. In Chapter 6 ZnO nanostructures are introduced along with the routes we have used to synthesise ZnO tetrapod nanocrystals. Chapter 7 is focussed on characterising the ZnO tetrapod nanocrystals that we have grown. In Chapter 8 the means by which ZnO tetrapod Schottky diodes have been fabricated is outlined with various analysis techniques. Finally, a conclusion with some discussions and prospects for the future is found in Chapter 9.

2. Electronic Properties of ZnO

2.1 Introduction

ZnO is a wide band-gap II-VI semiconductor with a direct fundamental energy gap of 3.37 eV. As grown ZnO exhibits n-type conductivity largely attributed to the hydrogen impurities [1]. An understanding of the electronic structure is pivotal in determining the potential use of the material within device applications. In this chapter we review the electronic surface and bulk properties of wurtzite ZnO. We then briefly show how these properties are influenced when ZnO nanostructures are considered.

2.2 Crystal Structure of ZnO

Zinc Oxide (ZnO) is a group II-IV compound semiconductor that can be found in either the rocksalt (B1), zinc-blende (B3) or wurtzite (B4) structure. The wurtzite crystal structure of ZnO is the most energetically favourable under ambient conditions. Rocksalt ZnO belongs to the *Fm3m* space group and is six fold coordinated. This structure is however not favoured in epitaxial growth. Using *in situ* X-ray diffraction it was shown that a pressure induced phase transitions from wurtzite to rocksalt occurred when 9.6 GPa was applied to the material. Moreover this process was reversible with the wurtzite structure returning at 2 GPa [2,3]. Heteroepitaxial growth of zinc-blende ZnO is possible using cubic substrates such as ZnS which has lattice constants that are closely matched. Zinc-blende ZnO belongs to the *F43m* space group and forms with tetrahedral symmetry. Using the generalised gradient

approximation (GGA) to the exchange-correlation function with the density functional framework, Jaffe *et al.* accurately predicted the energy of cohesion for each structure [4]. They were –7.455, –7.679 and –7.692 eV for rocksalt (B1), zinc-blende (B3) and wurtzite (B4) structures respectively. Zinc-blende and wurtzite ZnO share the same tetrahedral coordination and therefore share the same nearest neighbour bond distance (figure 2.1).

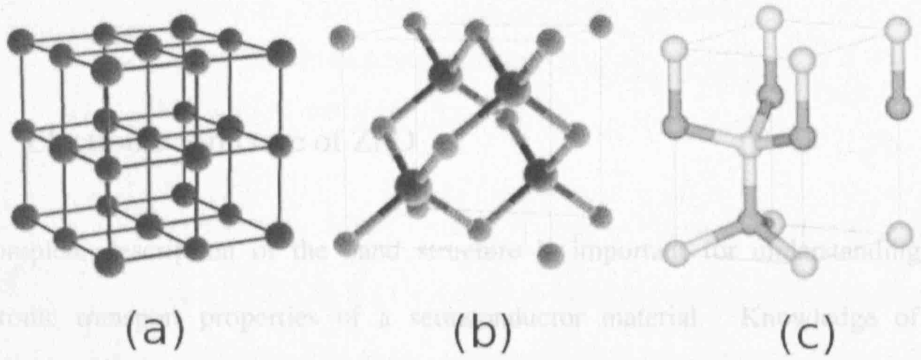

Figure 2.1. Image showing unit cell for a) rocksalt ZnO, b) zincblende ZnO and c) wurtzite ZnO.

Wurtzite ZnO belongs to the space group of $P6_3mc$ and has lattice parameters 'a' and 'c' in the ratio of $c/a=\sqrt{(8/3)}$. This structure is comprised of two interpenetrating hexagonal-close-packed (hcp) sublattices each of which has an atom of one kind surrounded by four of the other kind at tetrahedral angles. Lattice constants are most accurately measured using techniques such as 'reflection high-energy electron-diffraction' (RHEED) and 'X-ray diffraction' (XRD). Table 2.1 shows the measured and calculated lattice parameters for wurtzite ZnO. These results show good agreement of the model predictions with experimental results. The lattice constants are in the range of 3.2475 to 3.2501 Å for the 'a' parameter and from 5.2042 to 5.2075 Å for the 'c' parameter.

Table 2.1. Lattice constants for wurtzite ZnO derived from X-ray diffraction and *ab initio* methods.

a (Å)	c (Å)	c/a	u	Reference
3.2496	5.2042	1.6018	0.3819	[3]
3.2501	5.2071	1.6021	0.3817	[6]
3.2860	5.2410	1.5950	0.3830	[7]

2.3 Electronic Structure of ZnO

A complete description of the band structure is important for understanding the electronic transport properties of a semiconductor material. Knowledge of the electronic structure is also required when considering the device applications of the semiconductor material. Tetrahedrally co-ordinated compound semiconductors with zinc-blende and wurtzite structure are largely classified as covalently bonded materials. Zinc oxide however has a large ionic contribution to the bonding scheme which poses a greater challenge to accurately predicting the electronic band structure.

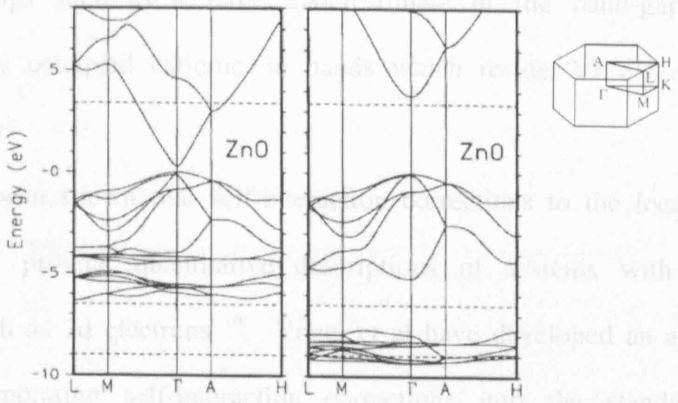

Figure 2.2. LDA bulk band structure calculations for wurtzite ZnO using standard PP (left) and SIC PP (right) (Vogel *et al.* [8]).

Theoretical calculations of the band structure of zinc oxide mostly rely on the local density approximation (LDA) to the exchange correlation function within the density functional theory. Massidda *et al.* have made comparisons between the Hartree-Fock, LDA and the GW calculation methods [9]. This can be used to predict both bulk [10] and surface [11] properties of the material. Zinc oxide is not fully amenable to a pseudopotential description of core electrons as the O 2p and the Zn 3d are of the lowest lying orbitals of their symmetry type [12]. These strongly localised electron states results in incomplete screening of the nuclear charge and therefore require a large number of plane waves for a fully convergent solution. Earlier calculations [11,13-15] based on the local density approximation treated the Zn 3d states as core electrons. Although this greatly simplified the computational task, these calculations failed to accurately predict the energy levels of the 3d states and under estimated the lattice constants by as much as 18% within wurtzite ZnO. Inclusion of the 3d electrons into the valence band yields accurate lattice constants. Even if the key electrons are properly taken into account, the results of the standard LDA calculations showed

distinct shortcomings such as a large underestimate of the band-gap and an overestimate of the occupied cationic 3d bands which reside 2.7 eV above the experimental values.

It has previously been shown that self-interaction corrections to the local density approximation can provide quantitative descriptions of systems with strongly localised states such as 3d electrons [16]. Vogel et al have developed an alternative approach to incorporating self-interaction corrections into the standard LDA calculations by employing atomic self interaction corrected pseudopotentials (SIC-PP)[8]. In this technique full SIC-LDA atomic calculations are carried out which yield better term values and wave functions than standard LDA calculations. Atomic non-local pseudopotentials are then constructed so that the same term values outside the core radius and the same eigenfunctions are predicted as in the full SIC-LDA calculations.

Figure 2.2 shows the band structure for ZnO using both the standard PP and SIC-PP. A considerable downward shift of the d bands is observed in the SIC corrected pseudopotential. The band-gap has also drastically increased and more closely resembles the experimentally measured value of 3.37 eV. Changes have also appeared in a dispersion and bandwidth of the O 2p states. The SIC-PP results do however predict the energy of the d bands to be 1 eV below the experimentally determined values. Table 2.2 summarises these predictions.

Table 2.2. LDA calculated and measured electronic energy gap E_g, cation d band position E_d and anion p valence bandwidth for wurtzite ZnO. eV units (Vogel *et al.* [8]).

	PP	SIC-PP	Experimental Values
E_g	0.23	3.77	3.37
E_d	-5.1	-8.9	-7.8
W_p	-3.99	-5.2	-5.3

A number of experimental techniques have been used to measure the band structure of ZnO. These techniques conventionally involve X-ray or UV reflection, absorption or emission spectroscopy. Energy differences between states are measured by inducing transitions between electronic levels within the material. These include transitions from the upper valence band states to the upper conduction band states and collective mode excitations from upper core states to the lower edge of the conduction band. X-ray photoelectron spectroscopy (XPS) is an important technique for investigating energy levels based on the photoelectric effect. Peaks in the XPS spectrum correspond to photo excited electron emission from core levels without inelastic scattering. The recent development of angle-resolved photoelectron spectroscopy (ARPES) techniques have provided a powerful tool for measuring bulk and surface electronic band structures under the assumption of momentum conservation and nearly free electron-like bands. Vesley et al have carried out X-ray photo electron spectroscopy on cleaved hexagonal wurtzite ZnO [17]. Their results placed the Zn 3d core level 8.5 eV below the valence band maximum. Similar results were reported by

Ley *et al.* using XPS [18]. Self-interaction corrected LDA calculations are in good agreement with these measurements.

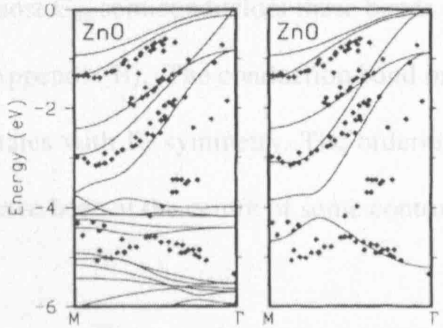

Figure 2.3. Comparison of LDA calculated and XPS measured valence electronic energy bands (Vogel *et al.* [8]).

Figure 2.3 shows a comparison between the experimentally obtained valence band structure of wurtzite ZnO [19] and LDA calculations. Experimental values were obtained using angle-resolved photoelectron spectroscopy (ARPES). Although there are some discrepancies it can be seen that SIC LDA calculations shown on the right more closely matched the experimental data.

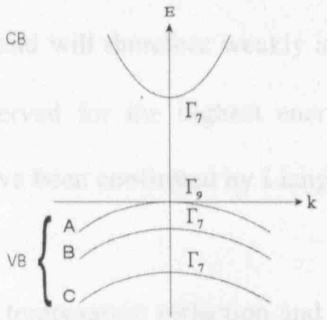

Figure 2.4. Schematic band diagram of ZnO showing 3 highest valence bands with ordered symmetry according to group theoretical arguments.

The highest six valence band states of hexagonal wurtzite semiconductors are split into three subbands due to the presence of spin-orbit coupling and the crystal field. These are usually labelled from highest to lowest and energy as A, B and C bands. In most C_{6v} semiconductors these bands have Γ_9, Γ_7 and Γ_7 symmetries respectively (see Appendix B). The conduction band in wurtzite ZnO is mainly constructed from s-like states with Γ_7 symmetry. The ordering of crystal field and spin-orbit coupling states have been at the centre of some controversy for several years.

Thomas [20] studied the fine structure of the valence band maximum using polarisation dependence of the UV absorption and reflection spectra. He concluded that the valence band ordering was anomalous when compared to other II-VI wurtzite semiconductors and that the symmetry of the highest valence band state was Γ_7 rather than Γ_9. In the absence of spin-orbit coupling, the valence band splits into a p_z-like singlet Γ_1 and a p_xp_y-like doublet state Γ_5 [21]. Transitions from the C-Γ_1 band should then be allowed in the $E \parallel c$ polarisation while the A/B-Γ_5 transitions are allowed for $E \perp c$. With spin-orbit coupling included, the Γ_7 state derived from the Γ_5 state displays a p_z-like admixture and will therefore weakly allow transitions for the $E \parallel c$ polarisation. This was observed for the highest energy transition and hence the assignment. These results have been confirmed by Liang and Yoffe [22].

Park *et al.* [23] performed low temperature reflection and absorption measurements on bulk ZnO. These results suggested that the A exciton lines, attributed by Thomas to free exciton states, were in fact due to bound excitons arising from ionised donor and neutral donor/acceptor complexes. These findings were later disputed by Segall [24]

who studied the phonon assisted absorption in ZnO. His findings once again confirmed that the A_m and A_L absorption lines were due to free excitons. Reynolds *et al.* [25] revisited this topic using second order UV photoluminescence spectroscopy. The difference in magnetic-field behaviour between $\Gamma_7 \rightarrow \Gamma_7$ and $\Gamma_7 \rightarrow \Gamma_9$ transitions was used to resolve the valence-band ordering in bulk ZnO. They also concluded that the observed spectral lines were due to free excitons but that the valence band maximum had Γ_9 symmetry and not Γ_7 as suggested by Thomas.

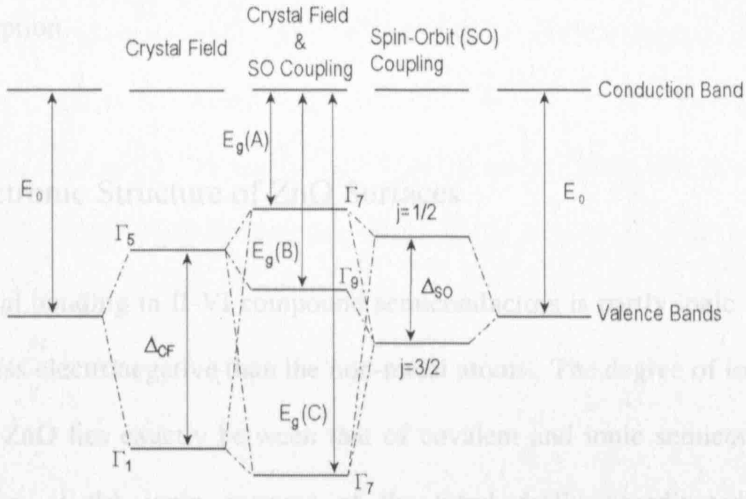

Figure 2.5. Schematic diagram of the effect of the crystal field and spin orbit coupling on the symmetry ordering of valence energy bands in Wurtzite ZnO.

Lambrecht *et al.* [26] used both the Linear Muffin-Tin Orbital (LMTO) method and the atomic sphere approximation to solve the Kohn-Sham equation within the LDA approximation. They emphasised that the observed spin-orbit splitting of the valence band was intimately related to the position of the Zn 3d bands below the valence band maximum [26,27]. By considering the electron-hole exchange interaction they solved the

Kohn-Luttinger Hamiltonian [28] for an exciton within a weak magnetic field. Effective Landé g factors were then calculated using the experimental value of the d band position as an empirical fitting parameter. Their results showed that a negative $g_{\perp}$ factor for the A exciton is necessary to explain the observed Zeeman splitting of exciton peaks. They therefore concluded that the highest valence band has Γ_7 symmetry in agreement with Thomas. Moreover, they showed that shifting the d bands until the spin-orbit splitting becomes positive (the A-Γ_9 symmetry condition) causes a significant underestimate of the crystal field splitting and is therefore not a valid assumption.

2.4 Electronic Structure of ZnO Surfaces

The chemical bonding in II-VI compound semiconductors is partly ionic as the metal atoms are less electronegative than the non-metal atoms. The degree of ionic bonding in wurtzite ZnO lies exactly between that of covalent and ionic semiconductors. It therefore lies at the ionic extreme of the tetrahedrally coordinated compound semiconductors whose zinc blend and wurtzite structure lead to their classification as covalently bonded materials. Studying the surface properties of ZnO provides information about the ionic contribution to features in the surface electronic structure. Charge transfer that occurs in partly ionic bonds leads to variations in the core level binding energies when measured with respect to the neutral atoms. The change in these binding energies can be measured using photo emission spectroscopy (PES). Using this technique, the escape length for photo excited electrons was found to have a minimum for kinetic energies near 40 eV for most semiconductors. The

experimental conditions can then vary from bulk sensitive to surface sensitive by varying the energy of the exciting photons.

The four main low-index surfaces in Wurtzite crystals are the non-polar $(10\bar{1}0)$ and $(11\bar{2}0)$ surfaces and the polar Zn-terminated (0001) and O-terminated $(000\bar{1})$ surfaces.

2.4.1 Non-polar ZnO surfaces

The non-polar $(10\bar{1}0)$ surface is of particular interest for surface chemistry studies as the surface is terminated with equal numbers of Zn and O atoms. Using angle resolved photo emission spectroscopy (ARPES) Göpel *et al.* identified surface induced features at the Γ, M and X points in the surface Brillouin Zone [29]. These peaks were attributed to O 2p dangling bond states and Zn 4s – O 2p backbones (figure 2.6).

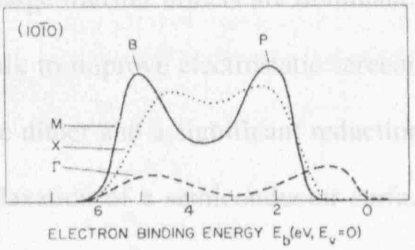

Figure 2.6. Angle resolved photoelectron spectra of Wurtzite ZnO $(10\bar{1}0)$ surface at Γ, M and X points in the surface Brillouin Zone (Cardona *et al.* [29]). At the X point, peaks at 4.5 and 2 eV are attributed to backbond emission and O 2p derived dangling bonds respectively.

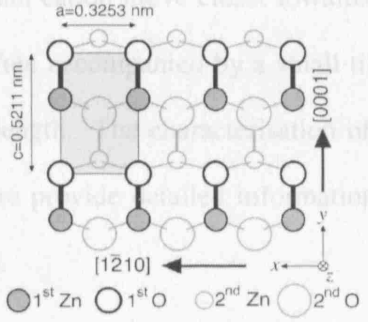

Figure 2.7. Crystal structure of Wurtzite ZnO $(10\bar{1}0)$ surface with unit cell highlighted (Ozawa *et al.* [30]).

Ozawa *et al.* performed normal photoemission spectroscopy on ZnO ($10\bar{1}0$) surfaces as a function of photon energy [30]. They identified a non dispersive peak at 3.7 eV that showed sensitivity to chemisorbed K and O_2 species. Moreover this peak was attributed to the O 2p dangling bond state, in good agreement with the results of Göpel *et al.*, due to its attenuation with O_2 adsorption.

It has been found that non-polar clean surfaces of Wurtzite II-VI semiconductors show the same basic relaxation where the surface cation moves inward while the anion stays above resulting in a tilt of the dimer. The geometry of this relaxation is largely dictated by dehybridisation and charge transfer effects. In predominantly covalently bonded semiconductors, the cation will rehybridise from sp^3 to sp^2 and will move downwards closer to the three anion neighbours. The anion will often relax outwardly. The result is a large tilt of the surface dimer. In ionic semiconductors, the charge transfer effects are dominant. Both anion and cation move closer towards the bulk to improve electrostatic screening. This is often accompanied by a small tilt of the dimer and a significant reduction in the bond length. The characterisation of the relaxation of a semiconductor surface can therefore provide detailed information on the nature of chemical bonding of the bulk material.

Low energy electron diffraction (LEED) is commonly used to study surface structure. Duke *et al.* have performed LEED on the ($10\bar{1}0$) surface of ZnO [31]. They observed a downward displacement of 0.45 +/- 0.1 Å for the top layer Zn ion and 0.05 +/- 0.1 Å for the top layer O ion which results in a tilt of 12° +/- 5°. No compelling evidence for vertical distortion of ions below the surface was obtained. The pronounced inward

relaxation of the Zn ion was later confirmed in angle resolved photo emission experiments [29].

A number of theoretical investigations into the $(10\bar{1}0)$ surface structure of ZnO have been performed using density functional theory (DFT) and Hartree-Fock methods [32-34]. These methods have employed Gaussian type orbitals as basis functions to solve the surface structure problem. Small inward relaxations of surface Zn ions were obtained leading to small tilts of the dimer in the range of 2° to 5°. It is, however, questionable whether or not these findings represent fully converged results. A recent study by Filippetti *et al.* using plane wave basis sets, which often provide more accurate results, predicted a larger relaxation with a tilt of 11.7° [35].

Table 2.3. Tilt angle ω of Zn-O dimer on the non-polar $(10\bar{1}0)$ surface. A number of calculated values are compared with Low energy electron diffraction (LEED) measurements. $C_{B,\|}$ is the percentage change in the dimer bond length parallel to the surface.

	ω (°)	$C_{B,\|}$	Reference
LEED	12 ± 5	-3 ± 6	[31]
LDA (plain wave)	11.7	-6.0	[35]
LDA (Gaussian)	3.6	-7.9	[32]
Hartree-Fock	2.3	-7.2	[33]
B3LYP	5.2	-4.9	[34]

2.4.2 Polar ZnO surfaces

Most polar surfaces show a large surface reconstruction or exhibit faceting as a means of accommodating charge transfer due to dangling bonds. Faceting is markedly

visible in the family of ZnO nanostructures [36,37]. Polar ZnO surfaces are, however, remarkably stable. Several experiments suggest that they are in an unreconstructed, clean and fully ordered state. The mechanism by which the polar ZnO surfaces are stabilised is not fully understood [38]. The polar (0001) surface of Wurtzite ZnO was studied by Gerard *et al.* using angle resolved photo emission spectroscopy (ARPES) [39]. Recording the emission spectrum in the range of 20 to 50 eV, they were able to obtain valuable information about the bulk and surface energy states. From their data, seven peaks were identified and labelled from A to G. Of these peaks, two were identified as surface related. The remaining peaks were identified as resulting from core level transitions. The two surface related peaks were attributed to O 2p – Zn 3d interaction and Zn 4s – O 2p back bonding states.

First principals calculations consistently predict a 20-30% contraction of the first Zn-O double layer for the Zn terminated surface [38,40,41]. Ion scattering experiments have not revealed a contraction and have even shown an outward relaxation of the Zn surface layer [42,43]. Using scanning tunnelling microscopy (STM) Dulub *et al.* found double atomic layer deep pits in the (0001) surface of ZnO [44]. If the edges of the pits are assumed to be O terminated, an analysis of the island and pit size distribution revealed a 25% decrease in the Zn concentration at the surface. This would provide enough charge transfer needed to stabilised the polar surface [45].

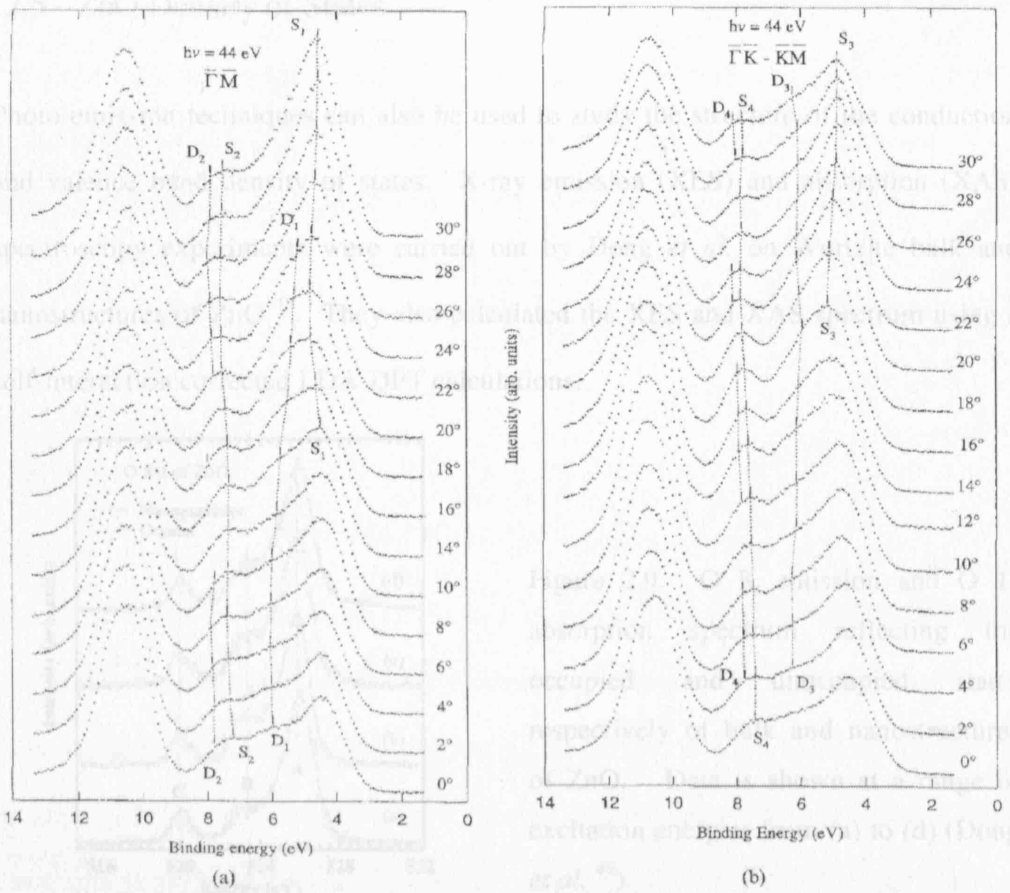

Figure 2.8. Off normal emission spectrum of (0001) ZnO surface. The presence of surface states labelled $S_{1\text{-}4}$ are revealed [39].

X-ray measurements show large relaxations for the ($000\bar{1}$) O-terminated surface where the double layer distance is reduced by approximately 50% [41]. In contrast, low energy electron diffraction (LEED) measurements have concluded that the Zn-O double layer spacing is close to that of the bulk [46]. Using He scattering, Kunat *et al.* showed that processes commonly used to prepare O terminated surfaces result in surfaces covered in H [47,48].

2.5 ZnO Density of States

Photo-emission techniques can also be used to study the structure of the conduction and valence band density of states. X-ray emission (XES) and absorption (XAS) spectroscopy experiments were carried out by Dong *et al.* on Wurtzite bulk and nanostructures of ZnO [49]. They also calculated the XES and XAS spectrum using a self-interaction corrected LDA-DFT calculations.

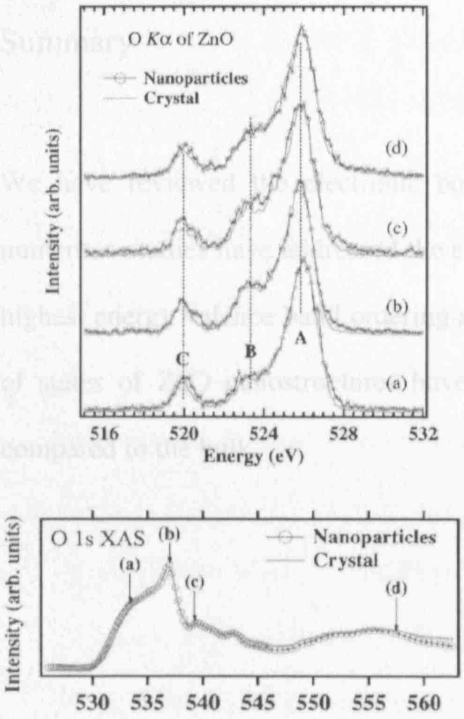

Figure 2.9. O K emission and O 1s absorption spectrum reflecting the occupied and unoccupied states respectively of bulk and nanostructures of ZnO. Data is shown at a range of excitation energies from (a) to (d) (Dong *et al.* [49]).

Their combined XES and XAS data estimated the fundamental energy band-gap as 3.3 eV in good agreement with the previously determined value of 3.37 eV [50]. The XES and XAS spectra for both bulk ZnO and ZnO nanostructures are overlayed in Figure 2.9. Three distinct features were identified in the XES and labelled A, B and C. Feature A centred at 526 eV is attributed to O 2p – Zn 4p bonding states. Feature B centred at 523 eV is attributed to O 2p – Zn 4s mixed states while feature C centred

at 520 eV is due to O 2p – Zn 3d hybridisation [39]. By taking the difference of spectra for ZnO bulk and nanocrystals, they were able to identify a significant relative enhancement of the 520 eV C peak. This implies that there is an increase in the strength of 4s-2p-3d hybridisation in ZnO nanostructures when compared to the bulk [51].

Summary

We have reviewed the electronic bulk and surface structure of ZnO. Although numerous studies have addressed the electronic structure of ZnO, features such as the highest energy valence band ordering are still in debate. Studies made on the density of states of ZnO nanostructures have shown an enhanced p-d hybridisation when compared to the bulk.

Reference List

[1] C. G. Van de Walle, Phys. Rev. Lett. **85**, 1012 (2000)

[2] S. Desgreniers, Phys. Rev. B **58**, 14102 (1998)

[3] H. Karzel, W. Potzel, M. Köfferlein, W. Schiessl, M. Steiner, U. Hiller, G. M. Kalvius, D. W. Mitchell, T. P. Das, P. Blaha, K. Schwarz, and M. P. Pasternak, Phys. Rev. B **53**, 11425 (1996)

[4] J. E. Jaffe, J. A. Snyder, Z. Lin, and A. C. Hess, Phys. Rev. B **62**, 1660 (2000)

[5] U. Ozgur, Y. Alivov, C. Liu, A. Teke, M. A. Reshchikov, S. Dogan, V. Avrutin, S. J. Cho, and H. Morkoc, J. Appl. Phys. **98**, 041301 (2005)

[6] E. H. Kisi and M. M. Elcombe, Acta Cryst. C **45**, 1867 (1989)

[7] M. Catti, Y. Noel, and R. Dovesi, J. Phys. Chem. Solids **64**, 2183 (2003)

[8] D. Vogel, P. Krüger, and J. Pollmann, Phys. Rev. B **52**, R14316 (1995)

[9] S. Massidda, R. Resta, M. Posternak, and A. Baldereschi, Phys. Rev. B **52**, R16977 (1995)

[10] Y. N. Xu and W. Y. Ching, Phys. Rev. B **48**, 4335 (1993)

[11] I. Ivanov and J. Pollmann, Phys. Rev. B **24**, 7275 (1981)

[12] S. H. Wei and A. Zunger, Phys. Rev. B **37**, 8958 (1988)

[13] S. Bloom and I. Ortenbur, Phys. Status Solidi B **58**, 561 (1973)

[14] J. R. Chelikowsky, Solid State Commun. **22**, 351 (1977)

[15] D. H. Lee and J. D. Joannopoulos, Phys. Rev. B **24**, 6899 (1981)

[16] J. P. Perdew and A. Zunger, Phys. Rev. B **23**, 5048 (1981)

[17] C. J. Vesely, R. L. Hengehold, and D. W. Langer, Phys. Rev. B **5**, 2296 (1972)

[18] L. Ley, R. A. Pollak, F. R. McFeely, S. P. Kowalczyk, and D. A. Shirley, Phys. Rev. B **9**, 600 (1974)

[19] G. Zwicker and K. Jacobi, Solid State Commun. **54**, 701 (1985)

[20] D. G. Thomas, J. Phys. Chem. Solids **15**, 86 (1960)

[21] A. Mang, K. Reimann, and S. Rubenacke, Solid State Commun. **94**, 251 (1995)

[22] W. Y. Liang and A. D. Yoffe, Phys. Rev. Lett. **20**, 59 (1968)

[23] Y. S. Park, C. W. Litton, T. C. Collins, and D. C. Reynolds, Phys. Rev. **143**, 512 (1966)

[24] B. Segall, Phys. Rev. **163**, 769 (1967)

[25] D. C. Reynolds, D. C. Look, B. Jogai, C. W. Litton, G. Cantwell, and W. C. Harsch, Phys. Rev. B **60**, 2340 (1999)

[26] W. R. L. Lambrecht, A. V. Rodina, S. Limpijumnong, B. Segall, and B. K. Meyer, Phys. Rev. B **65**, 075207 (2002)

[27] M. Cardona, Phys. Rev. **129**, 69 (1963)

[28] J. M. Luttinger and W. Kohn, Phys. Rev. **97**, 869 (1955)

[29] W. Göpel, J. Pollmann, I. Ivanov, and B. Reihl, Phys. Rev. B **26**, 3144 (1982)

[30] K. Ozawa, K. Sawada, Y. Shirotori, K. Edamoto, and M. Nakatake, Phys. Rev. B **68**, 125417 (2003)

[31] C. B. Duke, R. J. Meyer, A. Paton, and P. Mark, Phys. Rev. B **18**, 4225 (1978)

[32] P. Schröer, P. Krüger, and J. Pollmann, Phys. Rev. B **49**, 17092 (1994)

[33] J. E. Jaffe, N. M. Harrison, and A. C. Hess, Phys. Rev. B **49**, 11153 (1994)

[34] A. Wander and N. M. Harrison, Surf. Sci. **457**, L342-L346 (2000)

[35] A. Filippetti, V. Fiorentini, G. Cappellini, and A. Bosin, Phys. Rev. B **59**, 8026 (1999)

[36] M. C. Newton, S. Firth, T. Matsuura, and P. A. Warburton, J. Phys. Conf. Ser. **26**, 251 (2006)

[37] H. Yan, R. He, J. Pham, and P. Yang, Adv. Mater. **15**, 402 (2003)

[38] C. Noguera, J. Phys. : Condens. Matter **12**, R367-R410 (2000)

[39] R. T. Girard, O. Tjernberg, G. Chiaia, S. Soderholm, U. O. Karlsson, C. Wigren, H. Nylen, and I. Lindau, Surf. Sci. **373**, 409 (1997)

[40] J. M. Carlsson, Computational Materials Science **22**, 24 (2001)

[41] A. Wander, F. Schedin, P. Steadman, A. Norris, R. McGrath, T. S. Turner, G. Thornton, and N. M. Harrison, Phys. Rev. Lett. **86**, 3811 (2001)

[42] H. Maki, N. Ichinose, N. Ohashi, H. Haneda, and J. Tanaka, Surf. Sci. **457**, 377 (2000)

[43] M. Sambi, G. Granozzi, G. A. Rizzi, M. Casarin, and E. Tondello, Surf. Sci. **319**, 149 (1994)

[44] O. Dulub, U. Diebold, and G. Kresse, Phys. Rev. Lett. **90**, 016102 (2003)

[45] N. Jedrecy, M. Sauvage-Simkin, and R. Pinchaux, Appl. Surf. Sci. **162-163**, 69 (2000)

[46] C. B. Duke and A. R. Lubinsky, Surf. Sci. **50**, 605 (1975)

[47] M. Kunat, S. Gil Girol, T. Becker, U. Burghaus, and C. Wöll, Phys. Rev. B **66**, 081402 (2002)

[48] A. Wander and N. M. Harrison, J. Chem. Phys. **115**, 2312 (2001)

[49] C. L. Dong, C. Persson, L. Vayssieres, A. Augustsson, T. Schmitt, M. Mattesini, R. Ahuja, C. L. Chang, and J. H. Guo, Phys. Rev. B **70**, 195325 (2004)

[50] V. A. Karpina, V. I. Lazorenko, C. V. Lashkarev, V. D. Dobrowolski, L. I. Kopylova, V. A. Baturin, S. A. Pustovoytov, A. J. Karpenko, S. A. Eremin, P. M. Lytvyn, V. P. Ovsyannikov, and E. A. Mazurenko, Cryst. Res. Technol. **39**, 980 (2004)

[51] J. H. Guo, L. Vayssieres, C. Persson, R. Ahuja, B. Johansson, and J. Nordgren, J. Phys. : Condens. Matter **14**, 6969 (2002)

3. Optical Properties of ZnO

3.1 Introduction

Many interesting optical properties have been observed in ZnO using experimental techniques such as optical absorption, transmission, reflection, photoluminescence and cathodoluminescence spectroscopy. ZnO displays a number of optically excitable energy states many of which can be observed in luminescence measurements. As a result it can become difficult to relate the observed spectra to a particular transition without an adequate account of the physical processes that may occur. For this reason we begin by introducing light-matter interactions in semiconductors with particular emphasis on polar and anisotropic materials such as ZnO. Mathematical formalisms used to describe optically excited quasi-particles such as excitons are also introduced. At this point we take care to refrain from exhaustive derivations where no further physical insight is attained and instead refer the reader to more detailed text where this can be found. We then present the results of optical measurements on ZnO and relate the observations to physical processes we have described.

3.2 Macroscopic Optical Properties of Semiconductors

Using Maxwell's equations in the absence of free space charges $\rho = 0$ we can derive the following equations for the electric field within a semiconductor [1,2]:

$$\nabla^2 \boldsymbol{E} - \mu_0 \varepsilon_0 \ddot{\boldsymbol{E}} = \mu_0 \ddot{\boldsymbol{P}} + \mu_0 \dot{\boldsymbol{J}} + \nabla \times \dot{\boldsymbol{M}} \tag{3.1}$$

$$\boldsymbol{D} = \varepsilon_0 \boldsymbol{E} + \boldsymbol{P} \tag{3.2}$$

A number of additional assumptions can also be made for further simplification. For all II-VI semiconductors assumption of a non-magnetic material can be made. The current density $\boldsymbol{J}$ is directly related to the electric field through the conductivity σ. For intrinsic semiconductors or those that are lightly doped, the carrier density and hence the conductivity is small. In this limit the influence of the conductivity on the optical properties can be neglected. If a linear relationship between the polarisation and the electric field is assumed through the dielectric function $\varepsilon(\omega)$:

$$\boldsymbol{P} = \varepsilon_0 (\varepsilon(\omega) - 1) \boldsymbol{E} \tag{3.3}$$

we arrive at the following equation for the electric field:

$$\nabla^2 \boldsymbol{E} - \mu_0 \varepsilon_0 \varepsilon(\omega) \ddot{\boldsymbol{E}} = 0 \tag{3.4}$$

If it is also assumed that the electric field takes the form of plane waves:

$$\boldsymbol{E} = \boldsymbol{E}_0 \exp[\mathrm{i}(\boldsymbol{k} \cdot \boldsymbol{r} - \omega t)] \tag{3.5}$$

by substituting the following relationship is obtained:

$$\begin{aligned} \boldsymbol{k} &= \boldsymbol{k}_v\sqrt{\varepsilon(\omega)}, \\ |\boldsymbol{k}_v| &= \frac{\omega}{c} \end{aligned} \tag{3.6}$$

In the above, $\boldsymbol{k}_v$ represents the wave vector of an electromagnetic wave propagating within a vacuum. On entering a semiconducting material, this wave vector is altered by an amount equal to the square root of the dielectric function $\varepsilon(\omega)$. To simplify (3.6) we can define the complex index of refraction:

$$\tilde{n}(\omega) = n(\omega) + \mathrm{i}\kappa(\omega) = \sqrt{\varepsilon(\omega)} \tag{3.7}$$

The oscillating and spatially propagating wave within the semiconductor is associated with $n(\omega)$. This of course is known as the refractive index. $\kappa(\omega)$ describes the damping of a wave in the direction of propagation. This damping is associated with absorption and scattering. The decay in intensity I of the light is usually exponential with distance d into the material with absorption coefficient $\alpha(\omega)$:

$$I = I_0 e^{-\alpha(\omega)d} \tag{3.8}$$

Considering (3.6-8) the absorption coefficient may be written as:

$$\alpha(\omega) = \frac{2\omega}{c}\kappa(\omega) \tag{3.9}$$

Materials for which $\alpha > 0$ are known as passive. Light entering these materials is attenuated with the distance travelled into the material. Materials for which $\alpha < 0$ are

known as active, lasing or inverted materials. When these materials are excited within a certain frequency range light amplification is produced.

During the absorption process the energy of the light is converted into forms such as heat, chemical energy, mechanical energy and incoherent frequency shifted electromagnetism or photoluminescence. Other coherent energy dissipation routes include Rayleigh Scattering due to lattice disorder and frequency shifted Raman scattering. Coherent scattering phenomena can be used to study the crystal properties of semiconductors. More detailed treatments can be found in later chapters.

Many crystals have anisotropic symmetry. These include the hexagonal wurtzite structure of semiconductors such as ZnO, CdS and GaN. For these crystals, the oscillator strength and hence the coupling to the electromagnetic field will depend on the direction of the polarisation. To describe this situation the dielectric function is recovered in its most general tensor form. The relationship between the electric displacement and electric field in rectilinear coordinates is then:

$$D_i = \varepsilon_0 \sum_j \varepsilon_{ij} E_j , \quad i, j = x, y, z \tag{3.10}$$

Conservation of the electromagnetic field requires that $\varepsilon_{ij} = \varepsilon_{ji}$. If the coordinates are chosen so that $\varepsilon_{ij} = 0$ when $i \neq j$, we are left with three independent elements ε_{xx}, ε_{yy} and ε_{zz}. In uniaxial crystals $\varepsilon_{xx} = \varepsilon_{yy}$ and the z-axis is identified with the crystallographic **c**-axis. For cubic crystals all three elements are equal and we recover the scalar relationship for the dielectric function.

Dichroism is an immediate consequence of the tensor character of the dielectric function. This simply means that the observed absorption spectra will depend on the direction of the polarisation. Recently this effect has also been observed in ZnO nanoscale structures [3]. Generally the oscillator strength will be frequency dependent. From the Kramers-Kronig relations, it can therefore be seen that the refractive index $n(\omega)$ will also depend on the orientation of the electric field with the crystal c-axis. This effect is known as birefringence. For uniaxial materials the incident light beam can always be decomposed into electric field components parallel and perpendicular to the plane defined by the c-axis and in the incident wave vector (the main section). Light polarised perpendicular to this plane is known as ordinary (o). Its complex index of refraction $\tilde{n}(\omega)$ is independent of the orientation and is described by Snells' law. Light with polarisation within the plane is known as extraordinary (eo). The two components $\boldsymbol{E} \parallel \boldsymbol{c}$ and $\boldsymbol{E} \perp \boldsymbol{c}$ of the polarisation depend on the angle $\gamma = \angle(\boldsymbol{k}, \boldsymbol{c})$ between the incident light and the crystal c-axis.

Mollwo and Bond [4] have performed optical reflection measurements on bulk ZnO with light polarised parallel and perpendicular to the c-axis of ZnO. Using the Kramers-Kronig analysis method, they were able to deduce the refractive index as a function of the energy of the incident light. Their measurements were performed around the fundamental absorption region. Their results are summarised in the work of Yoshikawa and Adachi [4] who obtained similar results using spectroscopic ellipsometry. From Fig. 3.1 it can be seen that the refractive index for $\boldsymbol{E} \parallel \boldsymbol{c}$ and $\boldsymbol{E} \perp \boldsymbol{c}$ share a similar line shape. There are however slight differences between the two that lead to some birefringence in ZnO.

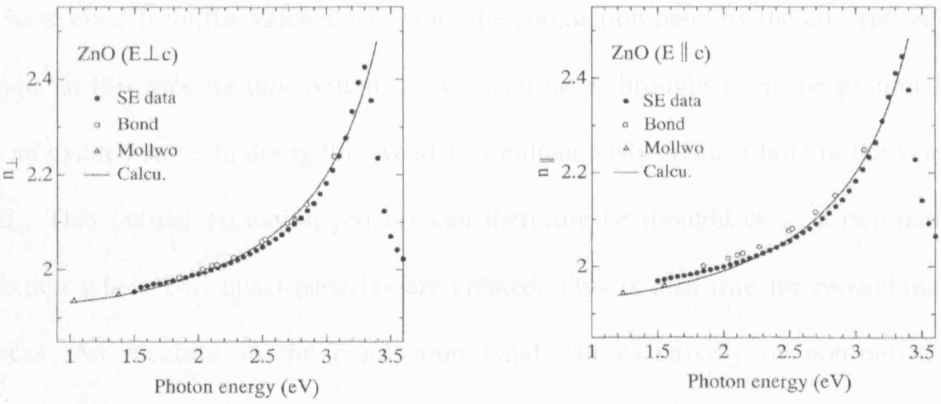

Figure 3.1. Dispersion of refractive index in ZnO obtained using spectroscopic ellipsometry (SE) for $\boldsymbol{E} \parallel \boldsymbol{c}$ and $\boldsymbol{E} \perp \boldsymbol{c}$ [4]. Open circles and triangles are data points from Bond and Mollwo respectively. Closed circles are data points from Yoshikawa and Adachi.

3.3 Free Excitons

When a semiconductor absorbs a photon with energy larger than the principal energy band gap, an electron is excited from the valence band into an otherwise empty state in the conduction band. There is therefore the absence of an electron in the valence band or hole left behind. Electron-hole pairs in their energetically lowest state are known as excitons. Excitons can be formed by the association of free electric charge carriers or by direct photo-excitation. Luminescence that follows charge association is the primary means by which light emitting diodes operate. Excitons formed by photo excitation can be made to disassociate into unbound electrons and holes and play a central role in photovoltaic and solar cell devices.

The ground state of the electronic system within an ideal semiconductor is a completely filled valence band and a completely empty conduction band. An electron

can be excited from the valence band into the conduction band by the absorption of a photon. In this process this system of N electrons is brought from the ground state into an excited state. In doing this we also simultaneously create a hole in the valence band. This optical excitation process can therefore be thought of as a two-particle transition where two quasi-particles are created. This is also true for recombination process. An electron in the conduction band can radiatively or non-radiatively combine with a hole in the valence band. Two quasi-particles are annihilated in the recombination process. This concept of particle–hole pair excitation is used successfully in several other physical disciplines. For example, a quantitative description of the transition energies of a neutron or proton from a deeper lying state into a higher empty state is only obtained if the particle in the excited state and the hole left behind are taken into account.

The conduction band of Wurtzite ZnO is mainly constructed from s-like states whereas the valence band is a p-like state split into three bands due to the effects of the crystal-field and spin-orbit interactions [5]. A discussion on the band structure of ZnO has been given in the previous chapter. Free exciton transitions between the conduction band and three valence bands are therefore governed by band edge intrinsic absorption and emission.

There are a number of ways to describe excitons within direct band gap semiconductor materials [6,7]. The effective mass approximation provides an intuitive description for many semiconductor materials. Within this approximation the interaction between the electron and hole leads to a Coulomb potential term within the Hamiltonian and a hydrogen-like solution. Neglecting electronic spin the Hamiltonian for the system may be written as:

$$H = \langle \psi(x) | H_0 | \psi(x) \rangle + \tfrac{1}{2} \langle \psi(x)\psi(y) | V(x-y) | \psi(y)\psi(x) \rangle \tag{3.11}$$

where H_0 and $V(x) = e^2/|x|$ are the Hamiltonian for a single electron and the Coulomb interaction potential respectively. In the simple picture of a single conduction and valence band and considering the periodicity of the lattice, the wave function can be expanded into a linear combination of Bloch type functions of H_0 such that:

$$\begin{aligned} \psi(x) &= \sum_{j=c,v} a_{kj} \psi_{kj}(x), \\ \psi_{kj}(x) &= u_{kj}(x) \exp(ik \bullet x)/\sqrt{N} \end{aligned} \tag{3.12}$$

The Hamiltonian therefore becomes:

$$\begin{aligned} H = {} & E_0 + \sum E_e(k) a_k^\dagger a_k + \sum E_h(k) b_k^\dagger b_k + \tfrac{1}{2} \sum \langle k_{i1}^c, k_{j2}^c | V | k_{l3}^c, k_{m4}^c \rangle a_{k_1}^\dagger a_{k_2}^\dagger a_{k_3} a_{k_4} \\ & + \tfrac{1}{2} \sum \langle -k_{i1}^v, -k_{j2}^v | V | -k_{l3}^v, -k_{m4}^v \rangle b_{k_1}^\dagger b_{k_2}^\dagger b_{k_3} b_{k_4} \\ & - \sum \left(\langle k_{i1}^c, k_{j2}^v | V | k_{l3}^v, k_{m4}^c \rangle - \langle k_{i1}^c, k_{j2}^v | V | k_{l3}^c, k_{m4}^v \rangle \right) a_{k_1}^\dagger b_{k_2}^\dagger b_{k_3} a_{k_4} \end{aligned} \tag{3.13}$$

where we have used the Fermi creation and annihilation operators, a_{k_j} and $a_{k_j}^\dagger$ respectively, in the language of second quantisation. Hole operators are defined so that the annihilation of a valence band electron in a state k corresponds to the creation of a hole in the valence band in state $-k$:

$$a_{k_e} = b^{\dagger}_{-k} \tag{3.14}$$

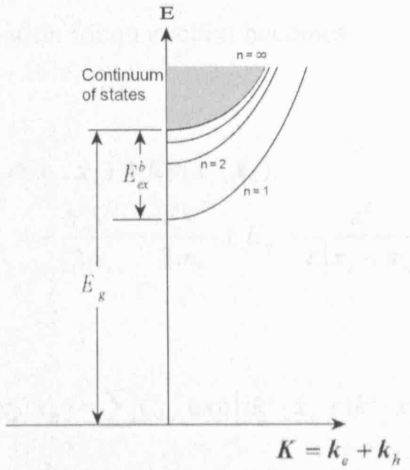

Figure 3.2. Schematic diagram of the dispersion relation of Wannier excitons within a direct band gap semiconductor. These states have discrete band with principal quantum number n. The continuum of conduction band ionised states are shown in the shaded region.

In the effective mass approximation, the constant energy term is neglected and the following approximations are made:

$$E_e(k) = E_g + \frac{\hbar^2 k^2}{2m_e}, \qquad E_h(k) = \frac{\hbar^2 k^2}{2m_h} \tag{3.15}$$

The effective mass of the electron and hole are m_e and m_h respectively. The most general eigenfunction of an electron-hole pair state is obtained by considering a superposition of states:

$$|p\rangle = \sum C_{kk'} a_k^{\dagger} a_{k'}^{\dagger} |p_0\rangle \tag{3.16}$$

Where p_0 corresponds to the ground state with an empty conduction band and a full valence band. An equation for the $C_{kk'}$ coefficients can be obtained by considering $H|p\rangle = E|p\rangle$. Taking the Fourier transform of equation (3.16), the Wannier equation for an exciton becomes:

$$H_{ex}\phi(\boldsymbol{x}_e,\boldsymbol{x}_h) = E\phi(\boldsymbol{x}_e,\boldsymbol{x}_h),$$
$$H_{ex} = -\frac{\hbar^2\nabla^2}{2m_e} - \frac{\hbar^2\nabla^2}{2m_h} + E_g - \frac{e^2}{\varepsilon|\boldsymbol{x}_e - \boldsymbol{x}_h|} \tag{3.17}$$

$$\phi(\boldsymbol{x}_e,\boldsymbol{x}_h) = \sum C_{kk'} \exp[i\boldsymbol{k}'\cdot\boldsymbol{x}_e + i\boldsymbol{k}'\cdot\boldsymbol{x}_h] \tag{3.18}$$

In arriving at this equation we have made a number of assumptions. We have assumed that the Coulomb potential is a slowly varying function which changes very little within a unit cell. This was first introduced by Wannier and is justified for weakly bound exciton states where the separation between the electron and hole are large when compared to the lattice constant. The polarisation of the electronic orbitals has been taken into account by introducing a static dielectric constant.

For a direct band gap semiconductor the relative motion of electron and hole can be separated to yield a dispersion relation:

$$E_{ex}(n,\boldsymbol{k}) = E_g - \frac{e^2}{2\varepsilon a_{ex} n^2} + \frac{h^2\boldsymbol{k}^2}{2M} \tag{3.19}$$

Where $n \in \mathbb{N}$, $M = m_e + m_h$ and $\boldsymbol{k} = k_e + k_h$.

The exciton Bohr radius and reduced mass are respectively given by:

$$a_{ex} = \frac{\hbar^2 \varepsilon}{\mu e^2} \tag{3.20}$$

$$\mu = \frac{m_e m_h}{m_e + m_h} \tag{3.21}$$

As is the case of the hydrogen atom, the exciton states converge for $n \rightarrow \infty$ towards the ionisation continuum which coincides with the conduction band at E_g.

For most semiconductors the following conditions are usually met:

$$50\,\text{nm} \geq a_{ex} \geq 1\,\text{nm} \geq a_{\textit{lattice constant}} \tag{3.22}$$

The exciton Bohr radius a_{ex} is usually much larger than the lattice constant. Electron-hole pairs that therefore have a common centre of mass that average over a number of unit cells are called Wannier-Mott Excitons. In this limit, excitons can be described in the framework of semiconductor Bloch equations where the effective mass approximation is valid. There are some materials, such as NaCl and some organic crystals, where the exciton wave functions are confined to a single unit cell. These are known as Frankel excitons and cannot be described by the effective mass approximation.

In many semiconductors the Exciton binding energy is small compared to the optical phonon energies $E_{ex} < \hbar\omega_{LO}$. As a consequence the exciton Bohr radius is much

larger than the polaron radius. In this limit the use of a static value for the dielectric constant is valid. In many wide band gap semiconductors including ZnO this is true only for the higher states $n>1$ but doesn't hold for the ground state exciton. An interpolated value for the dielectric constant between the static constant and the background limit is appropriate and depicts the partial polarisation of the lattice with the motion of the exciton. The Haken potential [8] makes a useful approximation to the dielectric function that is dependent on the distance between the electron and hole.

The features of excitons are enhanced in regions where electron and hole group velocities are equal. Excitons form at the Γ point where $\boldsymbol{k}=0$ and both group velocities are zero in direct band gap semiconductors such as ZnO.
Semiconductors in their ground state have angular momentum, spin, and total angular momentum equal to zero. If an electron is excited from the valence band into the conduction band by an electric dipole transition, the spin of the excited electron will not change because the electric field of the light does not act on the spin state. The total spin of electron hole pair will therefore remain as zero corresponding to a spin singlet state. If the excited electron interacts with the magnetic component of the light field causing the spin to flip, a triplet state is formed with a total spin of one.

The polarisation of an exciton is determined by both the symmetry of the Bloch functions a_{kj} and the wave function of its relative motion. Excitons are described as either transverse or longitudinal dependent on whether the polarisation is perpendicular or parallel to the wave vector of the centre of mass. Only transverse excitons couple directly to the transverse electromagnetic. The strength of this

coupling determines the radiative lifetime of the excitons. This can be evaluated by considering the interaction Hamiltonian as a perturbation the electronic excitations:

$$H_I = \langle \psi_c(\boldsymbol{x}) | -\frac{e}{cm_0} \boldsymbol{A}(\boldsymbol{x}) \cdot \boldsymbol{p} | \psi_v(\boldsymbol{x}) \rangle,$$
$$\boldsymbol{A}(\boldsymbol{x}) = \sum_{\boldsymbol{k}} \left(\frac{2\pi\hbar c^2}{\omega_{\boldsymbol{K}} n^2} \right)^{0.5} \boldsymbol{e}_{\boldsymbol{K}} e^{i\boldsymbol{K}\cdot\boldsymbol{x}} (c_{\boldsymbol{K}} + c^{\dagger}_{-\boldsymbol{K}}) \tag{3.23}$$

In the above ψ is the electron creation and annihilation operator for states in the conduction and valence band respectively. $\boldsymbol{A}(\boldsymbol{x})$ is the vector potential in the coulomb gauge where $\omega_{\boldsymbol{K}}$ is the photon frequency. The Hamiltonian describes direct transitions and can be evaluated by considering equation (3.23). The Matrix element that describes the probability of finding an electron and hole at the same location also describes the transition probability between the conduction and valence band. When this matrix element is non-zero, the transition is described as optically allowed. If the symmetry of the conduction and valence band causes the same matrix element to be zero, the transition is only weakly allowed and is said to be optically forbidden.

Forbidden transitions within direct band gap semiconductors are also due to additional intrinsic properties such as triplet states, spin-flip which affects the valence band ordering, longitudinal excitons and symmetry forbidden transitions (appendix B). These exciton states can however be observed in higher order perturbation theory where electric quadrupole or magnetic dipole transitions are considered.

3.4 Polaritons

There are various levels of sophistication which can be used to describe the interaction of light with a matter. In the previous section we have used a perturbative treatment to describe the properties of excitons in semiconductor materials. In this weak-coupling limit the electromagnetic field and the excitation of the matter are considered as independent quantities. Although this is sufficient for several purposes, many physical processes cannot be described within the weak-coupling limit. Moreover the optical excitation of matter is accompanied necessarily by some polarisation. If this were not the case, the electronic transition would not couple to the electromagnetic field via the dipole operator and would therefore be optically forbidden. It is also known that every oscillating polarisation will emit an electromagnetic wave which may then act back on the incident electromagnetic field. If we assume a linear relationship between the electric field and polarisation within matter, as is done throughout linear optics, we have the following relationship:

$$\boldsymbol{P} = \varepsilon_0[\varepsilon(\omega,\boldsymbol{k})-1]\boldsymbol{E} \tag{3.3}$$

It can be seen from this approximation that a polarisation wave will accompany the electric field provided $\varepsilon(\omega,\boldsymbol{k})$ deviates from unity. This is satisfied for the whole spectral range of ω up to the highest eigenfrequencies situated in the X-ray region. The quanta of mixed states of electromagnetic and polarisation waves are known as polaritons. They are the quasi-particles of light in matter.

In his study on the absorption of light by excited states of semiconductors, Hopfield used the formalisms of quantum electrodynamics to present a more complete view of the absorption of light within semiconductor materials [9]. It was shown that in the low density regime excitons are approximate bosons. The eigenstates of a system of

crystal and radiation fields were also shown to be a mixture of photons and excitons. It was also qualitatively shown that light within a semiconductor couples strongly with excitons to produce propagating modes with both exciton and photon like character. Absorption in this system therefore takes place when additional states are excited by the exciton-like part of the propagating mode. The Hamiltonian that describes the interaction between photons and other quasi-particles may be written as:

$$H = \sum_{k} \hbar\omega_k(\boldsymbol{k}) c_k^{\dagger} c_k + \sum_{k} E_t(\boldsymbol{k}) t_k^{\dagger} t_k + \sum_{k} g^1(\boldsymbol{k}, \tilde{a}, E_t)(c_k^{\dagger} + c_{-k})(c_{-k}^{\dagger} + c_k) + \sum_{k} g^2(\boldsymbol{k}, \tilde{a}, E_t)(t_k^{\dagger} + t_{-k})(c_{-k} + c_k^{\dagger}) \tag{3.24}$$

The first and second terms represent the photon and quasi-particle operators respectively, while $\tilde{a}$ is the polarisability. Remaining terms describe the interaction between the two including the annihilation of photons and the creation of quasi-particles. If these terms are described as a perturbation a solution in the weak coupling limit is obtained. This Hamiltonian can be diagonalised by choosing the appropriate linear combination of creation and annihilation operators for both photons and quasi-particles. Using the following linear transformation to a polariton operator:

$$p_k = u_1 c_k + u_2 t_k + u_3 c_{-k}^{\dagger} + u_4 t_{-k}^{\dagger} \tag{3.25}$$

the Hamiltonian can be diagonalised to yield:

$$H = \sum_{k,i=1,2} E_i(\boldsymbol{k}) p_{ki}^{\dagger} p_{ki} \tag{3.26}$$

From this the polariton dispersion relation may be written as:

$$\frac{c^2k^2}{\omega^2} = \varepsilon_b + \frac{4\pi\tilde{a}}{1-(\hbar\omega/E_t)^2} \tag{3.27}$$

In the vicinity of a single resonance the dispersion relation may be written in Helmholtz-Ketteler form:

$$\frac{c^2k^2}{\omega^2} = \varepsilon_b + \frac{f}{\omega_0^2 - \omega^2 + i\omega\gamma} \tag{3.28}$$

where f is the oscillator strength (a characteristic of the quasi-particle eigenenergy) and γ is the damping constant. For anisotropic crystals the tensor characteristics of the dielectric function causes these parameters to depend on the orientation of the crystal field relative to the crystal axis. Figure 3.3 shows the dispersion relationship with and without finite damping.

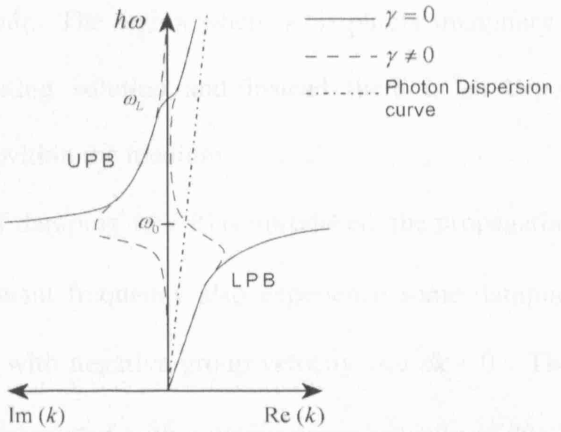

Figure 3.3. Schematic of the polariton dispersion relation within the vicinity of a single resonance. The consequence of finite damping ($\gamma \neq 0$) is that there is now at least one propagating mode within the vicinity of ω_0 with both real and imaginary parts.

The dispersion curve begins at $\omega = 0$ as a straight line with a gradient of $\hbar c(\varepsilon_b + f/\omega_0)^{-1/2}$. This region is known as the lower polariton branch (LPB). As the dispersion of a photon is also a straight line with gradient $\hbar c$, the polariton dispersion relation is said to be photon-like when it is a straight line. As the curve approaches the resonant frequency, it begins to flatten. In this region the dispersion is described as phonon-like or exciton-like according to the nature of the resonance. Within the present approximation of uncoupled oscillators, there appears a forbidden region between the transverse and longitudinal eigenfrequencies where there are no propagating modes. The longitudinal branch at $\hbar\omega_L$ usually does not couple strongly to the electromagnetic field. This is also the point at which the upper polariton branch (UPB) begins. The bands begin to bend upward with a gradient of $\hbar c\varepsilon^{-1/2}$ and show

photon-like behaviour. The region where $\boldsymbol{k}$ is purely imaginary means that there is no spatially oscillating solution and instead there is an exponentially decaying amplitude spatially within the medium.

If a finite amount of damping ($\gamma \neq 0$) is introduced, the propagating modes within the vicinity of the resonant frequency also experience some damping. The result is a region that appears with negative group velocity $d\omega/d\boldsymbol{k} < 0$. The strong absorption that is necessarily associated with a native group velocity within this spectral region provides a means of alleviating this seemingly unphysical result. The negative group velocity can be interpreted as a wave that is damped to the extent that it is prevented from propagating.

In crystals with C_{6v} symmetry, the dipole-allowed transitions generally couple strongly to the electromagnetic field and therefore necessitate the polariton model. Dipole-allowed levels that involve spin-energy flip such as the Γ_5 triplet excitons in ZnO (see section 2.3) have their oscillator strengths drastically reduced and interact to a lesser extent with the electromagnetic field.

In wurtzite materials that have uniaxial symmetry, the oscillator can either be excited with the same frequency in the xy plane normal to the crystallographic c axis or with a different frequency parallel to the z-axis. In the former a two-fold degenerate upper and lower polariton branch is obtained, but no longitudinal branch is seen for $\boldsymbol{k} \parallel z$ because both oscillators in the xy plane are transverse. When $\boldsymbol{k} \parallel x$ a transverse polariton branch is present for $\boldsymbol{E} \parallel y$ and a longitudinal branch exists for oscillations with orientation in the x direction. When $\boldsymbol{k} \parallel x$ and $\boldsymbol{E} \parallel z$ the crystal oscillators do not couple the electromagnetic field. If light propagates with an angle $\alpha = \measuredangle(\boldsymbol{c},\boldsymbol{k})$ that is

neither parallel nor perpendicular relative to the c-axis, the electric field can be decomposed into two components $E \| c$ and $E \perp c$, the relative strength of which depends on α. In such a case, mixed mode polaritons are formed where the "quantisation axis" for the electromagnetic field is the crystal c-axis. The corresponding dispersion curve is situated between the purely transverse and purely longitudinal case.

The degeneracy of the valence bands within C_{6v} semiconductors gives rise to a number of symmetry breaking effects which are neglected within the weak-coupling limit of the exciton model. For example, it is generally not possible to separate the relative motion of the electron and hole of an excitonic polariton from the motion of the exciton centre of mass. Certain symmetry states also become mixed which relaxes the selection rules allowing dipole forbidden states to receive an admixture of dipole-allowed states. The result is a more or less pronounced polariton effect [10].

3.5 Exciton Molecules

The exchange interaction between the electron hole pair of a Wannier exciton is small due to the relatively large exciton Bohr radius. Wannier excitons are therefore in many ways analogous to hydrogen atoms. Excitons however are quasi-particles and have a finite lifetime of the order of 10^{-10} s in a direct band gap semiconductor. With moderate excitation excitons are created with a concentration in which their mean distance is much greater than the exciton Bohr radius a_{ex}. In this limit, the exciton operator obeys the Bose commutation relation and their interaction can be neglected. Electron beam and laser excitation of semiconductors can generate electron hole pairs

in a concentration comparable to the exciton Bohr radius. At higher excitation densities, excitons no longer behave as ideal bosons. The effective interaction potential is attractive for excitons in the relative singlet state and repulsive for those in the relative triplet state. We may therefore expect excitonic molecules to form in analogy with the hydrogen molecule. Exciton molecules formed from two excitons are known as biexcitons and have been observed in a number of semiconductors including ZnO [11]. Additional molecules can also form including trions which consist of a pair of electrons (holes) bound to a single hole (electron). If the lifetime of excitonic molecules is long enough for the system to reach a quasi-equilibrium, the system can be described using thermodynamics. In dense systems a quasi-equilibrium is often reached in a short time.

In many semiconductors the ratio of the electron to hole mass $\sigma = m_e/m_h$ is much greater than that of the electron-proton mass ratio of the hydrogen atom. For ZnO $\sigma_{ZnO} = 0.30$ is more than 500 times larger. For larger values of σ it therefore seems possible that the exciton molecule would not be stable. To address this problem Akimoto *et al.* evaluated the binding energy of two excitons within the effective mass approximation as a function of the effective mass ratio [12]. Considering a four particle state wave function, the biexciton Hamiltonian can be written in a similar form to the Wannier equation shown above:

$$H_{xx} = -\frac{\hbar^2}{2m_e}(\nabla_{e1}^2 + \nabla_{e2}^2) - \frac{\hbar^2\nabla^2}{2m_h}(\nabla_{h1}^2 + \nabla_{h2}^2) + V_{xx},$$
$$V_{xx} = \frac{2E_{xx}^{b}e^2}{\varepsilon_0 a_{ex}}\left(\frac{1}{r_{e1e2}} + \frac{1}{r_{h1h2}} - \frac{1}{r_{e1h1}} - \frac{1}{r_{e1h2}} - \frac{1}{r_{e2h2}} - \frac{1}{r_{e2h1}}\right) \tag{3.29}$$

Within the effective mass approximation, the biexciton dispersion relation is given by:

$$E_{xx} = 2E_{ex}(n,\boldsymbol{k}) - E_{xx}^{b} + \frac{h^2\boldsymbol{k}^2}{2M} \tag{3.30}$$

The expectation value of the biexciton Hamiltonian can then be evaluated and minimised with respect to the variational parameters. This yields the ground state energy of the biexciton system as a function of the electron hole mass ratio σ. The biexciton binding energy can then be evaluated by considering:

$$E_{xx}^{b} = -E(\sigma) - 2E_{ex}^{b} \tag{3.31}$$

Figure 3.4 shows the normalised biexciton binding energy as a function of the electron hole mass ratio. The biexciton binding energy is shown to decrease monotonically with σ. From this it can be concluded that the exciton molecule is stable for all values of σ. It however must not be assumed that biexciton molecules in direct semiconductor materials will always form and can therefore be observed.

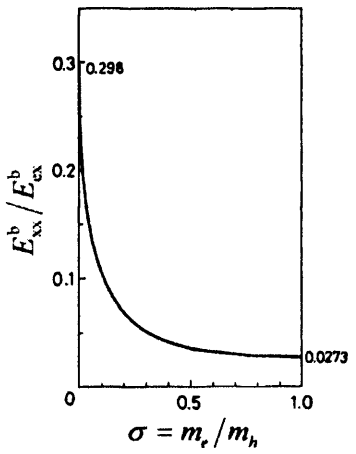

Figure 3.4. Biexciton binding energy shown as a function of electron hole mass ratio σ. From the abscissa it can be seen that the biexciton binding energy is always greater than zero and therefore the biexciton molecule is a stable structure (Okimoto *et al.* [12]).

The interaction potential between two excitons is often influenced by the electronic polarisation of the crystal lattice produced by the relative displacement of ions. This is especially true for strongly polar semiconductor materials such as ZnO. Within the quasi-static limit, polarisation effects brought about by electronic polarisation and electronic orbital interactions are routinely taken into account through the static or low frequency dielectric constant ε_0. In general this can only partly describe the interactions between exciton molecules and the polar crystal lattice. We therefore aim to provide a fuller description and hence a more complete understanding of the formation of exciton molecules. Replacing the static dielectric constant ε_0 with the high frequency equivalent ε_∞, the exciton Hamiltonian is coupled to the longitudinal optical phonons through the Fröhlich interaction Hamiltonian [13,14]:

$$H_{ex\text{-}L} = H_{ex} + H_L + \sum a_k H_{Fr} e^{ik\cdot R} \tag{3.32}$$

$$H_L = \sum_k \hbar\omega a_k^\dagger a_k \tag{3.33}$$

$$H_{\mathrm{Fr}} = -i\left(\frac{e^2 h\omega_{LO}}{V}\left(\varepsilon_\infty^{-1} - \varepsilon_0^{-1}\right)\right)^{1/2} \sum_k \frac{1}{k}\left(a_k e^{ik\cdot r} - a_k^\dagger e^{-ik\cdot r}\right) \tag{3.34}$$

where a_k and $a_k^\dagger$ are the phonon creation and annihilation operators respectively. Within the intermediate coupling regime, Lee *et al.* [15] were able to eliminate the phonon coordinates and minimize the energy of the system to obtain:

$$H_{\mathrm{ex}}^{eff} = -\frac{\hbar^2 \nabla_r^2}{2m_r} + V(r) \tag{3.35}$$

The Haken Potential $V(r)$ is given by [8]:

$$V(r) = \frac{e^2}{\varepsilon_0 r} - \frac{e^2}{2r}\left(\varepsilon_\infty^{-1} - \varepsilon_0^{-1}\right)\left(e^{-u_e r} + e^{-u_h r}\right), \tag{3.36}$$
$$u_i = (2m_i\omega/\hbar)^{1/2}, \quad i = e,h$$

This procedure may be extended to describe the interaction between two excitons. The biexciton Hamiltonian then becomes [16]:

$$H_{\mathrm{xx\text{-}L}} = H_{\mathrm{xx}} + H_{\mathrm{L}} + \sum\left\{a_k\left(H_{\mathrm{Fr}}(r_{e1h1})e^{ik\cdot R_{e1h1}} + H_{\mathrm{Fr}}(r_{e2h2})e^{ik\cdot R_{e2h2}}\right)\right\} \tag{3.37}$$

The interaction potential between two excitons in the relative singlet state can then be obtained by variation of the four-particle wave function. The effective Hamiltonian for the biexciton system becomes:

$$H_{xx}^{eff} = H_{ex}^{eff}(\boldsymbol{r}_{e1h1}) + H_{ex}^{eff}(\boldsymbol{r}_{e2h2}) + V^{eff} \tag{3.38}$$

$$V^{eff} = V(\boldsymbol{r}_{e1h2}) + V(\boldsymbol{r}_{e1h2}) + \frac{e^2}{r_{e1e2}}\left(\frac{1}{\varepsilon_0} + (\varepsilon_\infty^{-1} - \varepsilon_0^{-1})e^{-u_e r_{e1e2}}\right) + \frac{e^2}{r_{h1h2}}\left(\frac{1}{\varepsilon_0} + \varepsilon_\infty^{-1} - \varepsilon_0^{-1}e^{-u_h r_{h1h2}}\right) \tag{3.39}$$

Applying the Heitler-London covalency theory yields the energy of two interacting excitons as a function of their distance $\boldsymbol{R} = \boldsymbol{R}_{e1h1} - \boldsymbol{R}_{e2h2}$. Numerical calculations have shown that a predominantly attractive interaction potential is obtained between two excitons in polar crystals [17]. Moreover, carrier phonon interactions are shown to further enhance the stability of biexcitons [18]. At larger distances away from the biexciton Bohr radius an additional Van der Waals potential provides a further attractive contribution. It may therefore be said that the interaction between two excitons in the relative singlet state is always attractive within polar semiconductors.

Biexcitons have also been observed in quantum well structures, quantum dots and nanowires [19,20]. A significant enhancement of the biexciton binding energy has also been observed in structures of reduced dimensionality due to confinement effects [18,21]. The calculations of Singh *et al.* have shown that biexciton binding energy in quantum well structures should be approximately 22% of the exciton binding energy independent of well geometry [22]. A biexciton binding energy of 28 meV has been found in ZnO quantum wells [19]. Given the above this suggests that there is also a significant enhancement of the exciton binding energy in ZnO quantum well structures.

It has also been predicted that trions will form bound states in quantum well structures [23]. These states also contribute to the luminescence below the free exciton energy. Trion formation is favoured with moderately doped quantum well structures where localisation effects can play a role [24,25].

3.6 Two Photon Absorption Processes

In many semiconductors the probability of absorption by two photons is substantial enough for the resulting transitions to be observed in photoluminescence measurements. The process of two photon absorption (TPA), described within the strong coupling limit, occurs when two photon-polaritons merge to form an exciton-polariton [26]. It is said to have "giant" oscillator strength when the light is in resonance with the biexciton state such that $\hbar\omega_{ex} \approx E_{xx}/2$.

Two photon selection rules differ form those of single-photon transitions. As a direct result it is often possible for states to be occupied which are forbidden by one photon absorption (Appendix B).

Biexcitons within a semiconductor can either be created directly by TPA or indirectly by utilising intermediate states. In the former, light with energy $\hbar\omega_{ex}$ incident in the material populates states on the lower polariton branch (LPB). A second polariton with energy $\hbar\omega_{ex2} = E_{xx} - \hbar\omega_{ex}$ can then cause further transitions to the biexciton states. This additional transition appears as a peak in the absorption spectrum at $\hbar\omega_{ex2}$ with intensity that increases with an increase in the in the population at $\hbar\omega_{ex}$ on the lower polariton branch. The second biexciton formation begins with an

(incoherent) population of exciton-polaritons on the LPB. A photon of energy $\hbar\omega'_{ex2}$ is absorbed by an exciton causing a transition into a biexciton state. In the latter case, one of the polaritons is at the exciton-polariton part of the LPB. The decay of a biexciton into an exciton and photon polariton is simply the reverse of this two stage process. Luminescence bands due to biexciton decay are called M-bands and have an inverted Boltzmann curvature. The emission bands due to biexcitons generally occurs in the same spectral range as bound exciton complexes. In II-VI semiconductors, biexcitons appear with less structure due to mode mixing. The emission spectra of biexcitons often coincides with that of bound-exciton complexes (BEC) and other scattering processes. A proof of biexciton emission is therefore difficult to obtain solely from PL measurements [27].

3.7 Relaxation Processes

Excitons and biexcitons can be formed resonantly by optical absorption. If the absorbed light is not in resonance with either of the states, free electrons and holes are initially generated. In polar semiconductors such as ZnO, electrons couple strongly to optical phonons. Moreover, coupling to the longitudinal optical (LO) phonons as opposed to the transverse or the acoustic phonons is favoured as the corresponding lattice distortions of the polaron can be described by a superposition of LO phonons. Free carriers can therefore relax by emitting optical phonons while moving into an energy region below that of the optical phonon away from the band edge. Typical relaxation times are of the order of 100 fs. Further relaxation is possible with the emission of acoustic phonons. This coupling is described by a deformation potential

and through the piezoelectric effect. This is a considerably slower process as acoustic phonons are significantly lower in energy.

If the binding energy E_{ex}^{b} of the exciton is smaller than that of the optical phonon the electron-hole pair can relax by emission of a LO-phonon to form an exciton state. Measurements performed on a number of II-VI semiconductors have confirmed that excitons form before the complete relaxation of the free carriers [28]. It was also found that exciton formation increases in efficiency with an increase in the carrier density.

Another efficient means of exciton formation occurs from the cascade capture of electrons from a dense spectrum of excited states [13,29]. This process is highly efficient in semiconductors due to the long range Coulomb interaction potential between electron and hole.

In the intermediate density regime, where sufficiently high concentrations of excitons are present, excitons begin to interact. Scattering processes between excitons take place and in many cases lead to the formation of exciton molecules. Excess energy is transferred via acoustic phonons and other electronic excitation to bring the system into a quasi-thermal equilibrium. In order to apply thermodynamics to exciton molecule systems, a quasi-equilibrium must be reached within the lifetime of the excitation. Using simple thermodynamic arguments the relaxation time for an exciton molecule system at 20 K in ZnO is estimated at 3×10^{-12} s. A system of excitonic molecules is therefore brought into quasi equilibrium within a relatively short period of time.

3.8 Scattering Processes at Intermediate Excitation

At elevated optical excitation the interaction of excitons with phonons and other particles within their immediate environment must be considered. These many particle effects result in optical nonlinearities. The corresponding optical properties can no longer be determined by single electron hole pairs.

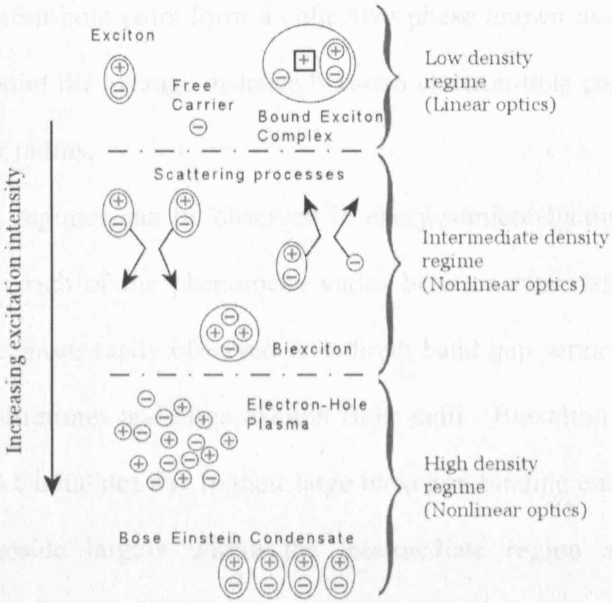

Figure 3.5. Many particle effects in optically excited semiconductors

In Figure 3.5 the various effects that may occur within increasing excitation intensity are divided into three categories. They are namely the low, intermediate and high density excitation regimes. The point at which each regime is reached is highly dependent on the quality of the sample. Within the low density regime, the optical properties can be understood by considering non interacting electron-hole pairs. In this limit the assumption of (3.3) is valid. At certain conditions excitons may also be bound to ionised defects in the form of bound exciton complexes (BEC). If the intensity of illumination is increased, the intermediate density regime is reached and excitons begin to interact. It is still assumed that the exciton is still a valid quasi-

particle. Elastic and inelastic scattering processes occur between excitons and between excitons and free carriers. As a result new luminescence bands appear and some broadening of exciton resonances may occur. Transitions to the exciton molecule via incoherent interactions are also favoured as previously discussed. If the sample is illuminated at an even greater intensity, the high density regime is reached. At this point electron-hole pairs form a collective phase known as the electron-hole plasma. At this point the average distance between electron-hole pairs is comparable to that of the Bohr radius.

Each of the three regimes can be observed in every semiconducting material. The ability to observe each of the phenomena varies between materials. Electron-hole plasma effects are more easily observed in indirect band gap semiconductors due to their long carrier lifetimes and large exciton Bohr radii. Biexciton effects are more easily observed in Cu halides due to their large biexciton binding energies. The II-VI semiconductors reside largely within the intermediate region allowing for the observation of all the effects outlined in figure 3.5. The disadvantage of this is that it is often difficult to separate the various contributions from each regime within resonant spectroscopy measurements. For example, the prospect of Bose-Einstein condensation of excitons in ZnO is one that has attracted much attention. Results so far are however inconclusive partly due to the inability in distinguishing the observed resonance peaks [30].

Scattering processes can be categorised as either elastic or inelastic. For elastic scattering processes, both momentum and energy are conserved for the initial set of particles. This process mainly causes homogeneous broadening. Inelastic scattering between excitons results in an exciton promotion to a higher state with principal

quantum number $n \geq 2$, while the other exciton is scattered onto the photon-polariton region of the LPB. The emission bands that result from exciton-exciton inelastic scattering events are usually called P-bands. In the simplest approximation it is expected that the luminescence intensity of these processes varies quadratically with the density of excitons. There is therefore a superlinear increase in intensity with excitation power.

Excitons that bear some thermal ionisation can interact with carriers within the semiconductor material. In this inelastic process, an exciton-polariton is scattered onto the photon-polariton region while the free carrier is excited into a higher state. A characteristic feature of this effect is a broad band that shifts to the lower energy region faster than the peak due to the band gap [31].

Exciton recombination can also occur with the simultaneous emission of a longitudinal optical phonon. This process can be observed at low excitation intensity as it does not rely on interaction with additional quasi-particles. Optical gain is often observed if the material is excited homogeneously.

The biexciton molecule decays into a photon-polariton and either a LO-exciton or an exciton on the LPB. This provides positive gain if the biexciton binding energy is large compared to the thermal energy [32].

Several inelastic scattering processes can occur within a semiconductor material and can involve additional quasi-particles [33]. Many of these processes give rise to optical gain and the appearance of new emission bands. The gain spectra for all of the inelastic processes can be obtained by formulating a rate equation according to the laser theory for the polaritons and all other excitation that are included. A complete description of this technique is provided by Haug *et al.* [34].

3.9 Luminescence Spectroscopy of ZnO

Determining the origin of luminescence in semiconductors is often difficult due to the various competing methods of radiative decay. Emission from these states can be difficult to resolve even at low temperatures with high quality samples. The reason for this is that the main recombination channel is non-radiative and largely involves defect centres. For wurtzite crystals A, B, and C exciton selection rules (Appendix B) for one photon processes can be summarised as follows. All excitons are allowed in the $\sigma(\boldsymbol{E} \perp c, \boldsymbol{k} \perp c)$ polarization, but the C-exciton is only weakly observable. The C-exciton is allowed in the π polarization ($\boldsymbol{E} \parallel c, \boldsymbol{k} \perp c$) but the A-exciton is forbidden and the B-exciton is weakly observable. In the α polarization ($\boldsymbol{E} \perp c, \boldsymbol{k} \parallel c$) all three transitions can be observed.

Teke *et al.* [35] studied the fine structure of free excitons in bulk ZnO at 10 K using photoluminescence (PL) spectroscopy in the $\boldsymbol{E} \perp c$ polarisation geometry (Fig. 3.6). They were able to observe the free A-exciton in the ground state ($n=1$) at $FX_A = 3.3771\,eV$. The B-exciton was also observed at $FX_B = 3.3898\,eV$. In polar semiconductors such as ZnO, transverse excitons couple to the photons to form polaritons. Polaritons can in principle form anywhere along their dispersion curve. Peaks are however observed at positions where the polariton lifetimes are high. The free A-exciton therefore has two components. A higher energy component is observed at 3.3810 eV and is attributed to recombination of the longitudinal exciton on the upper polariton branch (UPB_A). The low energy component is observed at 3.3742 eV and is attributed to recombination occurring on the Lower polariton branch (LPB_A). The separation between the UPB_A and the LPB_A from the free A-exciton is

measured as 3.6 meV and 2.9 meV respectively. This is consistent with theoretical predictions and previous experimental observations [36].

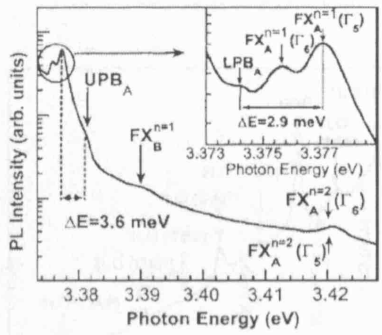

Figure 3.6. Free exciton photoluminescence spectra of ZnO obtained at 10 K (Teke *et al.* [35]).

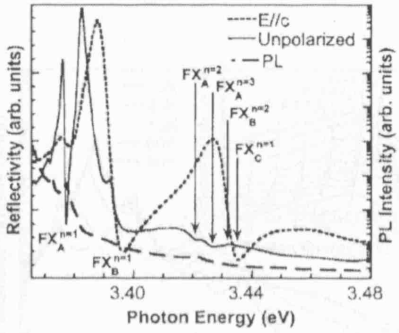

Figure 3.7. Reflectivity measurements performed at 10 K for unpolarised and π polarised light. The PL spectrum is of Fig. 3.6 is superimposed on the same graph to show the agreement in the peak positions (Teke *et al.* [35]).

Teke *et al.* also performed low temperature reflectivity measurements with unpolarised and π polarised light (Fig. 3.7). For unpolarised light A and B-exciton peaks are observed in good agreement with PL measurements. In the π polarisation the C-exciton is more pronounced and is visible at $FX_C = 3.435\,eV$.

Another luminescent channel of polaritons in semiconductors is brought about by the scattering of an exciton-polariton on the LPB onto the photon-polariton curve with the emission of a number of LO-phonons. The corresponding emission peaks are known as LO-phonon replicas. Once the polariton has reached the photon curve, it can travel through the material with limited interaction toward the surface. At this point it may

leave or be reflected back into the material by total internal reflection. In polar semiconductors the LO-phonon replicas are further pronounced due to increased lattice coupling. Figure 3.8 show the PL spectrum containing donor-acceptor pair (DAP) transitions and LO-phonon replicas taken at 10 K.

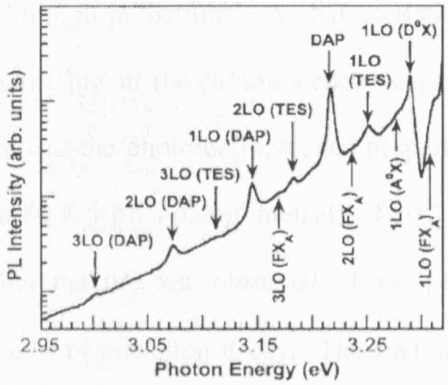

Figure 3.8. PL spectrum of ZnO obtained at 10 K (Teke *et al.* [35]).

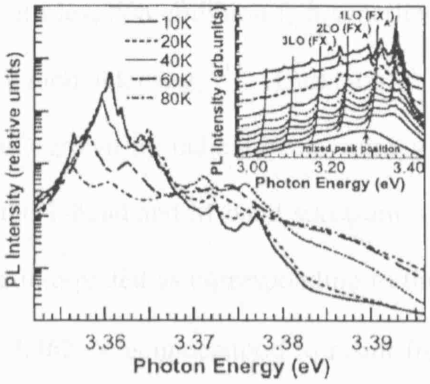

Figure 3.9. Temperature dependent PL spectrum of ZnO in the range of 10 – 160 K (Teke *et al.* [35]).

Peaks due to LO-phonon replicas occur at 71-73 meV intervals corresponding to the LO-phonon energy. The 1LO-phonon replica occurs at $1\mathrm{LO}(\mathrm{FX}_A) = 3.306\,\mathrm{eV}$. Some peaks appear as mixed states. Their origin was verified using temperature dependent measurements. The A and B-exciton peaks increase in intensity up to 40 and 80 K respectively and then decrease, hence their assignment. Bound states decreased in intensity and were gradually quenched with increasing temperature.

Luminescence due to inelastic scattering of excitons with carriers has been extensively studied in II-VI semiconductors [7,37]. A characteristic feature of this process is that the peak maximum corresponding to the emission shifts to lower photon energies with increasing temperature faster than the band gap.

Biexcitons are expected to occur as bound states in semiconductors. There are various routes to the decay of a biexciton [38]. The process of decay into a photon-like and an exciton-like polariton has previously been observed in Cu-halides. The decay of a biexciton into one polariton on the lower and upper polariton branch also occurs with high probability. A characteristic feature of biexciton emission is a superlinear increasing in the luminescence peak with excitation intensity [7,19]. Butkhuzi *et al.* studied the photoluminescence properties of ZnO grown by radical beam epitaxy [39]. At 80 K with a pump intensity of 10^{14} W/cm^2, the T-band and M-band spectrum with three maxima was observed. These peaks were interpreted as corresponding to three routes of biexciton decay. The first peak $M_1 = 3.362\,\text{eV}$ is understood to result from the decay of a biexciton into a photon-polariton and a exciton-polariton on the LPB. The second peak found at $M_2 = 3.348\,\text{eV}$ results from decay of a biexciton into a photon-polariton on the LPB and longitudinal exciton on the UPB. The final decay route results in the formation of two photon-polaritons which both leave the crystal with energies $M_3 = 3.322$ and $T_2 = 3.412\,\text{eV}$.

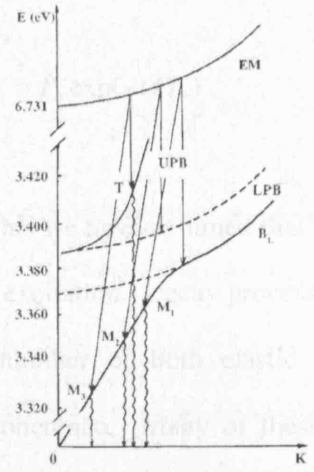

Figure 3.10. Dispersion curve of excitons and biexcitons. Luminescent decay routes from the biexciton curve to the lower polariton branch (LPB) are shown (Butkhuzi *et al.* [39]).

3.10 Time-resolved Photoluminescence

The development of femto second laser pulses has allowed the decay dynamics of optically excited processes in semiconductors to be measured directly in the time domain. Free exciton lifetimes are commonly measured using time-resolved photoluminescence as this provides a non-destructive means of characterisation. The exciton lifetime varies between samples and is dependent on the nature and density of defect states. The efficiency of radiative recombination is therefore strongly related to the decay time of the transition.

When an electromagnetic field is incident on a semiconductor the resulting polarisation is initially in phase with the field. Initial scattering processes within the exciton continuum of states destroy this coherence. The time in which the proportion of this polarisation that is in phase with the excitation reduces to $1/e$ is known as the decoherence or phase-relaxation time T_2. The coherent polarisation is then written as:

$$\boldsymbol{P}_{coh} = \boldsymbol{P}_0 \exp(-t/T_2) \tag{3.40}$$

In this we have assumed that the decay of the polarisation proceeds immediately after the excitation. Decay processes with exponential relation are known as Markovian [40]. A number of both elastic and inelastic scattering process can result in phase decoherence. Many of these processes have been outlined above and include the following:

1) The scattering with phonons proceeds via the Fröhlich interaction with longitudinal optical phonons and the piezo coupling to acoustic and optical phonons. This process has increasing importance with temperature.
2) Scattering with other electronic excitations such as exciton-exciton and exciton-electron interactions. This process depends on the optical excitation density.
3) Scattering with impurities, lattice defects and crystal interfaces. This process depends on both temperature and the nature of the excited species.

In the absence of phase breaking processes the phase will eventually be lost during the recombination process. The characteristic lifetime T_1 for the excited particle species with density ΔN can be given by:

$$\Delta N = \Delta N_0 \exp(-t/T_1) \tag{3.41}$$

As the number density is proportional to the square of the polarisation amplitude, considering (3.40) the following inequality holds:

$$T_2 \leq 2T_1 \tag{3.42}$$

In general there is an ensemble of characteristic times that describe the phase relaxation. If the corresponding oscillators have the same eigenfrequency then the decay time of each oscillator is the same and can be described by a Lorentzian energy distribution. If every oscillator has a different eigenfrequency distribution over an energy interval according to a Gaussian line shape, the decay of the ensemble is

shorter than each decoherence time. This is brought about by destructive interference between the phase shifted oscillators that cancels the polarisation. The amplitude of the radiation for inhomogeneous broadening therefore decays due to dephasing of the ensemble.

Interband relaxation as described above is largely characterised by a time constant T_3. If the excess energy is larger than the longitudinal optical phonon energy then the relaxation proceeds via this route due to the strong coupling. This process typically occurs on the sub pico-second scale. Further energy dissipation occurs via acoustic phonon emission which is much slower and takes progressively longer as the bottom of the energy band is approached.

It is possible to distinguish between homogeneous and inhomogeneous broadening using third order processes such as four wave mixing (FWM) allowing the decoherence time T_2 to be deduced.

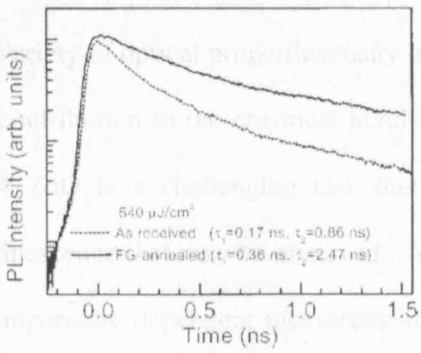

Figure 3.11. Room temperature time resolved PL data for the as received and the FG treated samples (Teke *et al.* [35]).

Room temperature time-resolved PL measurements were performed on as-received and annealed bulk ZnO samples by Teke *et al.* [35] . For as received samples with an

excitation energy density of 540 $\mu J/cm^2$ they observed a fast decay constant of 107.4 ps due to non-radiative processes (Figure 3.11). The slow decay component of 863.9 ps was attributed to the radiative lifetime of free excitons in good agreement with previous measurements [41,42]. Samples annealed in forming gas showed an increase in fast and free exciton decay constant to 358.7 ps and 2469 ps respectively. When the excitation density was decreased by an order of magnitude, a blue-shift of 15 meV was observed in the PL peak position. This can be attributed to band gap renormalisation. For as received samples the decay constants reduced slightly while those treated with forming gas showed an increase in decay lifetimes.

Summary

Zinc oxide shows a rich variety of optical properties many of which are brought about by the significant ionic contribution to the chemical bonding scheme. The study of the optical properties of ZnO is a challenging task due to the many competing processes leading to luminescence that may be observed. A number of spectroscopic techniques along with temperature dependent measurements are often used to verify findings. Optical transitions due to excitons-polaritons and biexciton molecules are readily observed in ZnO.

Reference List

[1] P. Morse and H Feshbach, *Methods of Theoretical Physics*, (McGraw Hill, 1953).

[2] C. Klingshirn, *Semiconductor Optics*, (Springer, Berlin, 2005).

[3] Z. Fan, P. c. Chang, J. G. Lu, E. C. Walter, R. M. Penner, C. h. Lin, and H. P. Lee, Appl. Phys. Lett. **85**, 6128 (2004)

[4] H. Yoshikawa and S. Adachi, **36**, 6237 (1997)

[5] J. L. Birman, Phys. Rev. **114**, 1490 (1959)

[6] R. J. Elliott, Phys. Rev. **108**, 1384 (1957)

[7] Masayasu Ueta, *Excitonic Processes in Solids*, (Springer-Verlag Berlin and Heidelberg GmbH & Co. KG, 1986).

[8] H. Haken, Nuovo Cimento **3**, 1230 (1956)

[9] J. J. Hopfield, Phys. Rev. **112**, 1555 (1958)

[10] K. Cho, Topics in Current Physics **14**, 1 (1979)

[11] G. B. Hvam, Phys. Status Solidi B **118**, 179 (1983)

[12] O. Akimoto and E. Hanamura, Solid State Commun. **10**, 253-& (1972)

[13] M. Lax, Phys. Rev. **119**, 1502 (1960)

[14] M. A. Stroscio and M. Dutta, *Phonons in Nanostructures*, (Cambridge University Press, 2001).

[15] T. D. Lee, F. E. Low, and D. Pines, Phys. Rev. **90**, 297 (1953)

[16] J. Pollmann and H. Buttner, Solid State Commun. **17**, 1171 (1975)

[17] D. B. Tran Thoai, Z. Phys. B **V26**, 115 (1977)

[18] V. I. V. Bobrysheva, Phys. Status Solidi B **88**, 315 (1978)

[19] H. D. Sun, Y. Segawa, T. Makino, C. H. Chia, M. Kawasaki, A. Ohtomo, K. Tamura, and H. Koinuma, Phys. Status Solidi B **229**, 867 (2002)

[20] A. Yamamoto, K. Miyajima, T. Goto, H. J. Ko, and T. Yao, Phys. Status Solidi B **229**, 871 (2002)

[21] D. A. Kleinman, Phys. Rev. B **28**, 871 (1983)

[22] J. Singh, D. Birkedal, V. G. Lyssenko, and J. M. Hvam, Phys. Rev. B **53**, 15909 (1996)

[23] B. Stebe, G. Munschy, L. Stauffer, F. Dujardin, and J. Murat, Phys. Rev. B **56**, 12454 (1997)

[24] D. M. Finlayson, *Localization and Interaction*, (Institute of Physics Publishing, 1986).

[25] F. Kreller, H. J. Wunsche, J. Puls, and F. Henneberger, J. Cryst. Growth **184-185**, 614 (1998)

[26] D. Boggett and R. Loudon, J. Phys. C **6**, 1763 (1973)

[27] H. J. Ko, Y. F. Chen, T. Yao, K. Miyajima, A. Yamamoto, and T. Goto, Appl. Phys. Lett. **77**, 537 (2000)

[28] H. Haug and P. Mengel, J. Lumin. **12-13**, 629 (1976)

[29] Z. S. Kachlishvili, M. G. Khizanishvili, and G. Khizanishvili, **V49**, 154 (2004)

[30] M. Zamfirescu, A. Kavokin, B. Gil, G. Malpuech, and M. Kaliteevski, Phys. Rev. B **65**, (2002)

[31] C.Klingshirn, Advanced Materials for Optics and Electronics **3**, 103 (1994)

[32] S. Shionoya, H. Saito, E. Hanamura, and O. Akimoto, Solid State Commun. **12**, 223 (1973)

[33] C. B. la Guillaume, J. M. Debever, and F. Salvan, Phys. Rev. **177**, 567 (1969)

[34] H. Haug and S. Koch, Phys. Status Solidi B **82**, 531 (1977)

[35] A. Teke, U. Ozgur, S. Dogan, X. Gu, H. Morkoc, B. Nemeth, J. Nause, and H. O. Everitt, Phys. Rev. B **70**, 195207 (2004)

[36] K. Hummer and P. Gebhardt, Phys. Status Solidi B **85**, 271 (1978)

[37] P. Zu, Z. K. Tang, G. K. L. Wong, M. Kawasaki, A. Ohtomo, H. Koinuma, and Y. Segawa, Solid State Commun. **103**, 459 (1997)

[38] R. Levy and C. Klingshirn, Phys. Status Solidi B **77**, 381 (1976)

[39] T. V. Butkhuzi, T. G. Chelidze, A. N. Georgobiani, D. L. Jashiashvili, T. G. Khulordava, and B. E. Tsekvava, Phys. Rev. B **58**, 10692 (1998)

[40] B. D Bartolo, *Frontiers of Optical Spectroscopy*, (Springer, 2005).

[41] T. Koida, S. F. Chichibu, A. Uedono, A. Tsukazaki, M. Kawasaki, T. Sota, Y. Segawa, and H. Koinuma, Appl. Phys. Lett. **82**, 532 (2003)

[42] S. W. Jung, W. I. Park, H. D. Cheong, G. C. Yi, H. M. Jang, S. Hong, and T. Joo, Appl. Phys. Lett. **80**, 1924 (2002)

4. Electronic Properties of Semiconductor Surfaces and Interfaces

4.1 Introduction

ZnO is used widely in catalysis, gas sensing and electronic device fabrication. An understanding of the geometric, electric and defect surface structure is therefore important for an understanding of their influence in these processes. The study and development of semiconductor surface and interface science is closely linked to advances in semiconductor device physics. Reports of rectifying behaviour at metal-semiconductor contacts are dated as early as 1874 where Braun [1] and Schuster [2] separately observed 'unipolar conductivity' in metal sulphides. Thirty years later solid-state rectifiers found application in telecommunications. Today they form an integral part of many semiconductor devices. The rectifying properties of metal-semiconductor contacts are named in honour of Walter H. Schottky [3] who in 1938 published a conclusive study identifying the presence of space-charge layers at the semiconductor surface. In this chapter, the electronic properties of semiconductor surfaces and interfaces are introduced. We discuss the effects that occur when a semiconductor is placed in contact with a metal or another semiconductor and the resulting transport properties. We then describe the various processes that occur when a semiconductor junction is brought into an excited state by illumination.

4.2 Surface Properties of ZnO

In ambient conditions, ZnO condenses into the wurtzite crystal structure in which each oxygen (zinc) ion is surrounded by a tetrahedron of four zinc (oxygen) ions. Cleaving perpendicular to the c-axis results in two polar surfaces with different structure. The basal surfaces are known as the (0001) -Zn terminated and the $(000\bar{1})$ -O terminated surfaces. These two surfaces have different chemical and physical properties.

Low energy electron diffraction (LEED) is commonly used to determine the atomic arrangements on semiconductor surfaces. Davisson and Germer [4] first used this technique to demonstrate the wave nature of matter using clean Ni surfaces. More recently, angle resolved photoemission spectroscopy (ARPES) has been used to obtain wavevector resolved surface band structures. Lüth *et al.* have compiled a review of modern surface analysis techniques [5].

Both surfaces exhibit (1×1) LEED patterns indicating that the polar surfaces of ZnO are unreconstructed [6,7]. High quality LEED patterns are obtained after a sequence of surface preparation techniques which include Ar ion sputtering and annealing at 600-700 °C. Annealing at higher temperatures results in a $(\sqrt{3}\times\sqrt{3})$ reconstruction that is due possibly to surface contamination or bulk impurities.

Ionic crystals formed from alternating layers of oppositely charges ions produce an accumulating dipole moment. Electrostatic considerations show that such a configuration results in highly unstable surfaces. Moreover it can be shown that the energy of the electrostatic field perpendicular to the surface can be shown to diverge within increasing thickness [8]. Many crystals therefore undergo large surface

reconstructions. In some cases, polar crystals are stable. The mechanism by which polar surfaces are stabilised is in debate [9]. The basal planes of ZnO are an example of stable polar surfaces. To compensate for the net dipole moment a rearrangement of charge on both the surface layers is required to cancel the polarity. The Zn and O terminated surfaces must reduce in charge density by a factor of ~0.75 to alleviate the macroscopic dipole moment. There are three principle means by which this can occur. In the first, surface states are formed that result in the transfer of negative charge from the O to the Zn surface. The second occurs with the removal of atoms form the surface to reduce the charge density. The third occurs when positively (negatively) charged impurity atoms are adsorbed onto the O (Zn) surface. In ZnO it is still not clear which mechanism prevails. Wander *et al.* [10] performed *ab initio* calculations using the B3LYP exchange and correlation functional [11]. In their study they showed that the stabilization mechanism of the polar surfaces involves a strong coupling between the two faces of the material via charge transfer. The observed surface properties of one surface of a polar crystal were found to be strongly dependent on the state of the other surface of the crystal, in favour of the first method. These calculations predict an outward relaxation of the surface ions which is in agreement with experimental measurements for the $(000\bar{1})$-O terminated surface. Maki *et al.* have however demonstrated that an outward relaxation occurs for the (0001)-Zn terminated surface [12]. Surface x-ray diffraction (SXRD) was used by Jedrecy *et al.* to study the properties of both polar surfaces of ZnO [13]. Their analysis of the results was performed in the context of x-ray kinematical theory. For the unreconstructed Zn terminated surface, they were able to show that a surface partial occupancy with probability of 0.74 best fits the observed data. Their findings are therefore in favour of the second stabilisation mechanism. How this stabilisation mechanism proceeds

was not addressed [14]. Energy calculations have suggested that the absorption of H (OH) on the surface of O (Zn) is energetically unfavourable at high coverage [10]. Diebold *et al.* have recently performed both scanning tunnelling microscopy (STM) and LEED measurements on the low-index planes of ZnO [15].

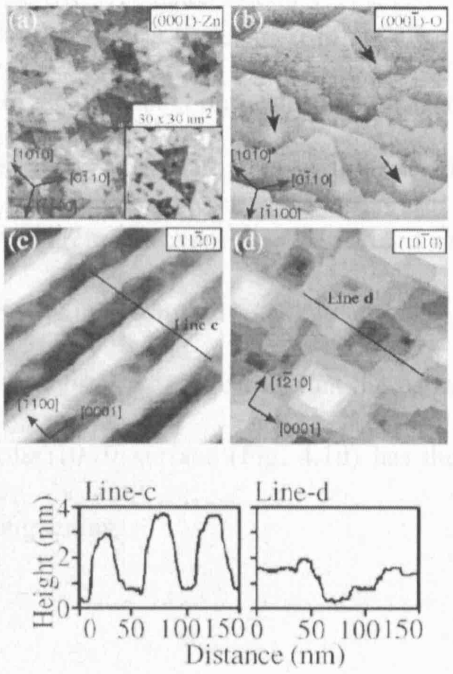

Figure 4.1. Scanning tunnelling microscopy (STM) image of the surface of ZnO after Ar ion sputtering and annealing in ultra high vacuum. All surfaces show (1×1) termination in LEED measurements. The Zn-terminated surface is characterized by many triangular islands with monatomic step height. Step edges are O-terminated, and the resulting non-stoichiometry stabilizes this polar surface. The O-terminated surface exhibits stoichiometric doublesteps with a 120° angle. The bright spots marked with arrows are attributed to subsurface impurities. The as grown $(11\bar{2}0)$ surface exhibits deep, regular ridges as indicated in the line profile. The $(10\bar{1}0)$ surface has a regular terrace step structure with rectangular islands. 200 nm × 200 nm images (Diebold *et al.* [15]).

It was found that the (0001) -Zn terminated surfaces (Fig. 4.1a) display a high density of triangular holes while maintaining the (1×1) periodicity in LEED. All holes were found to have a monatomic step height and are terminated with O atoms. The removal of Zn atoms therefore removes the macroscopic dipole moment supporting the second stabilisation mechanism. The $(000\bar{1})$ -O terminated surface appears smoother than the Zn-terminated with step edges that are two atomic layers in height. This surface is understood to stabilise through the presence of foreign atoms on the surface. Kunat *et al.* performed measurements that suggest that O-terminated surfaces are always saturated with hydrogen [16], in support of the third stabilisation mechanism. Measurements were also performed on non-polar surfaces. The non-polar $(11\bar{2}0)$ is shown in figure 4.1c. Regular deep grooves (35-65 Å) with (0001) oriented sides were observed suggesting that the surface is unstable and prone to faceting. The non-polar $(10\bar{1}0)$ surface (Fig. 4.1d) has the lowest cleavage energy and is less prone to roughening.

4.3 Electronic Surface States

At the surface of a semiconductor crystal the surface atoms have fewer atomic bonds than those of the bulk. The energy required to break these bonds and to form a surface is known as the surface energy. Many macroscopic effects such as the chemical reactivity are strongly related to the surface energy. We would therefore expect the electronic structure near to the surface to differ from that of the bulk. A general approach to understanding the surface electronic structure is to solve the Schrödinger equation within the one electron approximation near to the surface. Although translational symmetry remains parallel to the surface, this periodicity

breaks down perpendicular to the surface. The result is that mathematical formalisms such as Bloch's theorem commonly used within bulk materials break down and much more complex and computationally demanding methods are required. Moreover to compute the surface band structure, a complete knowledge of the atomic coordinates at the surface is required. As we have shown above, surfaces commonly undergo relaxation and reconstruction processes that often give rise to atomic scale features that are not homogeneously sized or distributed. Techniques such as low energy electron diffraction (LEED) and scanning tunnelling microscopy (STM) can provide some information on the surface structure and topography. There is however no straightforward means to experimentally determine the atomic structure of the surface layers and hence the surface band structure. To obtain a realistic surface band structure, a structural model of the surface must be constructed and the resulting band structure compared with experimental results.

4.3.1 Intrinsic Surface States

Surface energy states that result from clean and well ordered surfaces are known as intrinsic surface states. Energy states that arise from surface relaxation and reconstruction are also considered intrinsic. The two dimensional translational symmetry within the plane of the surface allows the component of the wave-function parallel to the surface to take plane wave form:

$$\phi_{ss} = (r_{\|}, z) = u_{k_{\|}}(r_{\|}, z)\exp(ik_{\|} \bullet r_{\|}) \tag{4.1}$$

To describe real surface states the wave-function normal to the surface must decay exponentially into the bulk ($z > 0$) and tail exponentially into the vacuum. This leads to the continuity condition [17] for the wave-function at the interface ($z = 0$):

$$\frac{1}{\psi_{vac}}\frac{\partial \psi_{vac}}{\partial z}\bigg|_{z=0} = \frac{1}{\psi_{z<0}}\frac{\partial \psi_{z<0}}{\partial z}\bigg|_{z=0} \tag{4.2}$$

The energy eigenvalues are therefore functions of the complex wave vector $k_{\perp} = \pi/a - iq$ normal to the surface and wave vector $k_{||} = (k_x, k_y)$ parallel to the surface. The result is a two-dimensional band structure for the electronic surface states. True surface state energy bands are characterised by energy levels E_{ss} that are not degenerate with bulk bands. Surface state energy bands are also able to penetrate into a part of the surface Brillouin zone where bulk states exist and interact with some degeneracy. Such states can penetrate into the bulk to form surface resonances.

The wave-functions of intrinsic surface states are compose of contributions from the semiconductor conduction and valence band wave-functions. They are therefore found within the forbidden band region and in the absence of a surface, would contribute to the bulk states. The position of the surface state within the band-gap is determined by the relative contribution of the conduction and valence band wave-functions. Surface energy states that are closer to the conduction band have conduction band character where those closer to the valence band have valence band character. Conduction band states will have negative charge if occupied by electrons where as valence band states will have positive charge if unoccupied. According to the definition of shallow impurities, the properties of the surfaces state varies from predominantly acceptor type to predominantly donor type from the conduction to

valence band respectively. The point at which the contribution from each is equal in magnitude is known as the branch point W_{bp}. At this point the decay length of the intrinsic interface state assumes its minimal value. In the simplest 1-dimensional model this is midway in the band-gap. In real crystals the position of the branch point is determined by the weighted contribution of the conduction and valence band density of states of the three-dimensional band structure.

4.3.2 Extrinsic Surface States

Electronic surface states that arise due to imperfections or adsorbed atoms at the surface are known as extrinsic surface states. An atom vacancy or interstitial at the surface will result in a redistribution of charge and a corresponding change in the bonding geometry. This is easily understood for ionic crystals such as GaAs and ZnO. A missing O^- ion at the surface creates an accumulation of positive charge at the vacancy which forms localised electronic defect states which an electron can occupy. The O^- vacancy therefore has acceptor like character.

Atoms adsorbed at an otherwise unperturbed surface cause changes in the chemical bonds in the local vicinity affecting the intrinsic surface states. Additional electronic surface states are formed due to the bonding states of the adsorbed species at the surface. Chemisorbed atoms or molecules may also form a 2-dimensional lattice along the surface with translational symmetry. In such cases a 2-dimensional band structure may be formed as is the case for intrinsic states.

4.4 Surface Space-charge

Electronic energy states at a semiconductor surface differing from those of the bulk originate from broken bonds and bonds formed with adsorbates at the surface. When a metal is brought into intimate and abrupt contact with a semiconductor, the electron wave-functions of the metal decay into the semiconductor. These wave-functions generally overlap with the band-gap of the semiconductor and create metal-induced interface states within the semiconductor. Equivalent effects occur for semiconductor heterostructures. Surface and interface states may therefore become charged resulting in a space-charge region that decays from the surface into the semiconductor. This effect occurs in semiconductors (as opposed to metals, where often the effect may be neglected) due to the low densities of free carriers and non-degenerate doping which leads to large carrier screening lengths.

4.4.1 Surface Space-charge and Surface States

One of the most important properties of any material surface is its work function. This is a measure of the energy required to disassociate an electron from the Fermi level within the material to the vacuum level:

$$\Phi = W_{\infty} - W_F \tag{4.3}$$

In a semiconductor the electron affinity and the ionisation energy are a measure of the difference in energy between the vacuum level and the surface of both the conduction and valence bands respectively:

$$\chi = W_{\infty} - W_{cs} \tag{4.4}$$

$$I = W_{\infty} - W_{vs} \tag{4.5}$$

Figure 4.2 shows the energy diagram of an n-type semiconductor brought into contact with a metal. The barrier height ϕ_{Bn} as defined by Schottky is the difference between the metal work function and the electron affinity of the semiconductor:

$$\phi_{Bn} = \phi_m - \chi \tag{4.6}$$

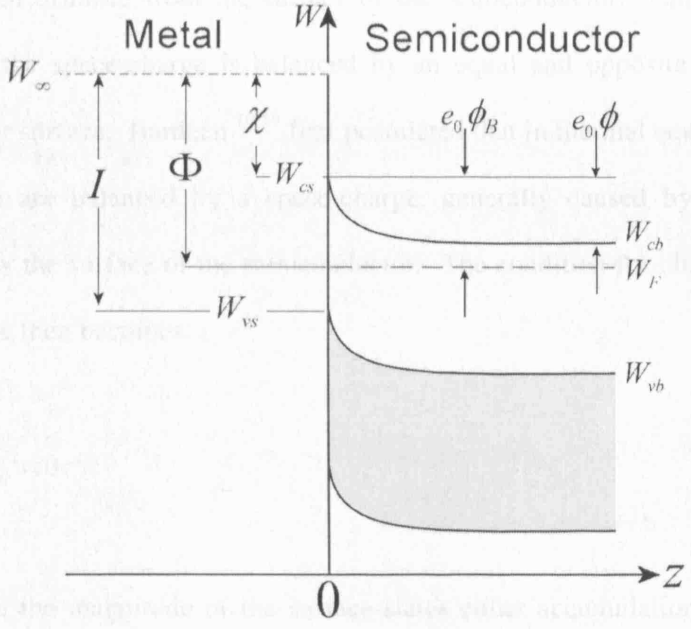

Figure 4.2. Energy diagram of the interface between a metal and an n-type semiconductor showing upward band bending at the surface.

For a p-type semiconductor it follows that the barrier height is the difference between the ionisation energy of the semiconductor and the metal work function:

$$\phi_{Bp} = E_g - (\phi_m - \chi) \tag{4.7}$$

It is this barrier that limits the flow of charge from the metal into the semiconductor and causes rectification at metal semiconductor interface.

Differing energy states at semiconductor surfaces and interfaces result in space-charge layers that extend into the semiconductor. If we consider a semi-infinite semiconductor material, the space-charge density Q_{sc} is the induced charge per unit area at a given distance from the surface of the semiconductor. Charge neutrality requires that the space-charge is balanced by an equal and opposite charge at the semiconductor surface. Bardeen [18,19] first postulated that in thermal equilibrium these surface states are balanced by a space-charge, generally caused by energy band bending below the surface of the semiconductor. The condition for charge neutrality at the interface then becomes:

$$Q_{tot} = Q_{ss} + Q_{sc} = 0 \tag{4.8}$$

Depending on the magnitude of the surface states either accumulation, depletion or inversion layers are possible within the space-charge region. The degree of band bending is determined by solving Poisson's equation for the system.

When a metal semiconductor system is in equilibrium, the Fermi level of the semiconductor must align relative to that of the metal with an offset equal to the

contact potential ϕ. If the density of surface states is large enough to accommodate additional surface charge that results from the finite contact potential without altering the Fermi level position, the space-charge will remain unchanged. As a result the barrier height will be a property of the semiconductor surface and is independent of the metal work function. This effect is known as *pinning of the Fermi level* at the surface. For example, a monolayer of adsorbates with acceptor like properties at the surface of an n-type semiconductor will cause a net negative charge which is compensated by the positive space-charge within the semiconductor. For a p-type semiconductor their energy position is above the Fermi level and they are therefore neutral. The space-charge and therefore the net surface states remain constant with a change in the metal work function up to the adsorbate acceptor level.

4.4.2 Space-charge Layers at Metal Semiconductor Interfaces

Garrett and Brattain reported the first detailed study of the electronic properties of semiconductor surfaces and interfaces [20]. The developed theoretical concepts were then used to describe contact potential measurements performed on Ge. Progress in surface studies is lead by developments in experimental techniques for studying surfaces. Due to the relatively low carrier density, spatially extended space-charge layers may exist within a semiconductor when brought into intimate contact with a metal. In thermal equilibrium this space-charge is balanced by the electronic surface and interface states. The resulting build up of charge within the space-charge region causes a local bending of the energy bands to form an accumulation, depletion or

inversion region for majority carriers. Large carrier concentrations in accumulation and inversion layers can lead to quantum size effects.

In the following we consider a semi-infinite semiconducting material with a single interface to derive the properties of the space-charge region. These ideas are easily extended into three dimensions. We refrain form doing so at this point as the additional complexity is not accompanied by further physical insight.

The presence of a space-charge region within a semiconductor material can be described by a spatially varying potential or band bending within the space-charge region (Fig. 4.2):

$$\phi(z) = \frac{1}{e_0}\left(W_{cb} - W_c(z - z_s)\right) = \frac{1}{e_0}\left(W_{vb} - W_v(z - z_s)\right) \tag{4.9}$$

The potential is bounded and typically has a maximum at the surface. The variable z is a point within the semiconductor. In equilibrium the surface band bending is given by:

$$\phi_s = \frac{1}{e_0}\left(W_{cb} - W_{cs}\right) = \frac{1}{e_0}\left(W_{vb} - W_{vs}\right) \tag{4.10}$$

where the subscripts b and s denote properties in the bulk and at the surface respectively. It is assumed that the potential vanishes into the bulk. The degree of band bending at the surface uniquely determines the space-charge density and the potential distribution within the space-charge layer. A negative (positive) potential causes upward (downward) band bending and results in a positive (negative) space-

charge. The potential is related to the space-charge density through the Poisson equation:

$$\varepsilon \cdot \nabla^2 \phi(z) = -\rho(z) \tag{4.11}$$

The dielectric function in general has tensor form causing the resulting charge density to be directly dependent on the crystal orientation and choice of surface. The space-charge region can be considered to consist of positive and negative charge due to static impurities and mobile electrons and holes. For an ionised semiconductor with shallow evenly distributed donors N_d and acceptor N_a levels this then becomes:

$$\rho(z) = e_0\{N_d - N_a - n(z) + p(z)\} \tag{4.12}$$

Using a parabolic density of states distribution function g_c we define the number of electrons in the conduction band per unit volume:

$$n = \int_{W_c}^{W_\infty} g_c(W) \cdot f_0(W) dW \tag{4.13}$$

$$g_c = 4\pi M_c \left(2m^*/h^2\right)^{1.5} \left(W - W_c\right)^{0.5} \tag{4.14}$$

$$f_0(W) = \left(\exp\left(\left[W - W_F\right]/k_B T\right) + 1\right)^{-1} \tag{4.15}$$

f_0 is the Fermi-Dirac distribution function, M_c is the number of equivalent conduction band minima and m_e^* is the electron effective mass. Substituting into (4.13) yields the carrier concentration and the conduction band density of states:

$$n = \left(2/\sqrt{\pi}\right) N_c F_{1/2}\left(-[W_c - W_F]/k_B T\right) \tag{4.16}$$

$$N_c = 2M_c\left(2\pi m^* k_B T/h^2\right)^{1.5} \tag{4.17}$$

$$F_{1/2}(y_F) = \int_0^\infty \frac{y^{0.5}}{\exp(y - y_F) + 1}\, dy \tag{4.18}$$

Further simplifying (4.16) recovers the classical Maxwell-Boltzmann distribution for electrons in the conduction band:

$$n_c = N_c \exp\left(-[W_c - W_F]/k_B T\right) \tag{4.19}$$

Following an analogous procedure, the distribution of holes in the valence band is given by:

$$p_v = N_v \exp\left([W_v - W_F]/k_B T\right) \tag{4.20}$$

In this classical limit the bulk carrier densities therefore become:

$$n_{cb} = N_c \exp\left(-[W_{cb} - W_F]/k_B T\right) \tag{4.21}$$

$$p_{vb} = N_v \exp\left([W_{vb} - W_F]/k_B T\right) \tag{4.22}$$

Substituting (4.19–4.22) and (4.9) into (4.12) and considering that $N_d - N_a = n_{cb} - p_{vb}$, the charge density may be written as:

$$\begin{aligned}\rho(z) &= e_0\left\{\left(n_c(z) - n_{cb}\right) + \left(p_v(z) - p_{vb}\right)\right\} \\ &= e_0\left\{n_{cb} - n_{cb}e^{\upsilon} - p_{vb} + p_{vb}e^{-\upsilon}\right\}\end{aligned} \tag{4.23}$$

where:

$$\upsilon(z) = e_0\phi(z)/k_B T \tag{4.24}$$

There are a number of methods that exist that enable the above to be solved, the choice of which is much dependent on the geometry of the system and choice of boundary conditions. For example, a finite difference method is well suited for arbitrarily shaped surfaces while a Green's function method is generally suited for a system that possesses some degree of symmetry [21].

If the dielectric material is considered semi-infinite with an abrupt surface at $z = 0$ we then have [20]:

$$\varepsilon \frac{d^2}{dz^2}\upsilon(z) = \frac{-e_0^2}{k_B T}\left\{n_{cb} - n_{cb}e^{\upsilon} - p_{vb} + p_{vb}e^{-\upsilon}\right\} \tag{4.25}$$

As equation (4.25) depends only on the potential υ, its direct integration is possible. Neglecting terms due to static impurities we have:

$$\varepsilon \int \frac{d\upsilon}{dz} \cdot d\frac{d\upsilon}{dz} = \frac{-e_0^2}{k_B T} \int_0^{\upsilon} \left\{ n_{cb} - n_{cb} e^{\upsilon} - p_{vb} + p_{vb} e^{-\upsilon} \right\} d\upsilon \tag{4.26}$$

$$\Rightarrow$$

$$\frac{d\upsilon}{dz} = \mp F / L_D \tag{4.27}$$

$$z / L_D = \int_{\upsilon_s}^{\upsilon} \mp F^{-1} \, d\upsilon \tag{4.28}$$

where the extrinsic Debye length L_D and the space-charge function F are given by:

$$L_D^2 = \varepsilon k_B T / e_0^2 \left(n_{cb} + p_{vb} \right) \tag{4.29}$$

$$F^2 = 2\left\{ p_{vb}(\upsilon + e^{-\upsilon}) - n_{cb}(\upsilon - e^{\upsilon}) \right\} / \left\{ n_{cb} + p_{vb} \right\} - 2 \tag{4.30}$$

The sign conventions in equation (4.28) are such that the upper sign refers to the case when the potential $\upsilon > 0$ and the lower for $\upsilon < 0$. By considering Gauß' law the space-charge density defined as the total charge per unit surface area is given by:

$$Q_{sc} = \varepsilon E_s = \varepsilon \left. \frac{d\phi}{dz} \right|_{z=0} = \mp e_0 \left(n_{cb} + p_{vb} \right) L_D F(\upsilon_s) \quad \text{C/m}^2 \tag{4.31}$$

Positive values of υ_s indicate a downward bending of the bands at the interface causing the conduction band to move closer to the Fermi level. For an n-type semiconductor this results in an accumulation of majority carriers at the interface and a negative space-charge. Similarly a negative value of υ_s results in an upward bending of the bands at the interface and an increase in the distance of the conduction band from the Fermi level. This leads to the depletion of majority carrier at the surface of an n-type semiconductor. If υ_s is further increased until the intrinsic level rises above the Fermi level at the surface, the density of minority carriers becomes larger than the intrinsic carrier density. At this point and inversion layer is present at the surface.

The shape of the space-charge region may be obtained though evaluation of equation (4.28). In depletion layers minority carriers do not play a significant role. The space-charge function may then be approximated by:

$$F \simeq F_{dep}(\upsilon) = \sqrt{2}\left\{e^{\upsilon} - \upsilon - 1\right\}^{0.5} \tag{4.32}$$

Upon substitution into equation (4.28) the potential may be written as:

$$|\upsilon| \approx \tfrac{1}{2}\left\{\sqrt{2\left(|\upsilon_s| - 1\right)} - z/L_D\right\}^2 + 1 \tag{4.33}$$

For $|\upsilon_s| \gg 1$ a simplified expression is obtained of the form:

$$|\upsilon| \approx |\upsilon_s|\left(1 - z/z_{dep}\right)^2 \tag{4.34}$$

The depletion layer thickness may then be estimated by:

$$z_{dep} = L_D \left(2|\upsilon_s|\right)^{0.5} \tag{4.35}$$

As the charge formed within the space-charge region is balanced by an equal and opposite charge at the surface, the electric field also penetrates some distance into the metal. This length is the Thomas-Fermi screening length [22] defined as:

$$L_{Th-F} = \left\{ \frac{e^2}{\varepsilon} g_m(W_F) \right\}^{-0.5} \tag{4.36}$$

where $g_m(W_F)$ is the density of states at the Fermi Level within the metal. A quantitative comparison of each characteristic length, we may consider the space-charge present at the Pt-ZnO interface region. For ZnO we assume that $\varepsilon/\varepsilon_0 = 9$ and $n_{cb} = 10^{17}$ cm^{-3}. With a surface potential of 1.3 eV, the width of the depletion region $z_{dep} = 110$ nm. For the metal, the density of states at the Fermi level is taken as $g_m = 3.45 \times 10^{22}$ cm^{-3} eV^{-1} which corresponds to Pt. The screening length becomes $L_{Th-F} = 4 \times 10^{-2}$ nm. This is clearly much smaller than the depletion layer width. It is therefore sufficient to study the properties of the space-charge region within the semiconductor neglecting effects within the metal.

4.5 Metal Semiconductor Interfacial Energy States

When a metal and semiconductor are brought into intimate contact in thermal equilibrium the Fermi levels of the two materials must align. This matching of the Fermi levels causes a flow of charge from one material to the other resulting in a dipole layer at the interface. Depletion, accumulation or inversion layers may occur depending on the difference between the metal work function and the semiconductor electron affinity χ. According to (4.6) a knowledge of the metal work function and the semiconductor electron affinity would allow the Schottky barrier height to be predicted. Experiments performed on Si metal-semiconductor junctions showed that the Schottky rule required a much greater variation in barrier height with metal work function than was observed experimentally. Moreover, when a metal comes into close contact with a semiconductor chemical bonds are formed with a strength that is dependent on the surface properties. Strong interactions will result in the formation of alloys and inter-diffusion. The distribution of the intrinsic surface states will be altered resulting in the additional transfer of charge between the materials. This can be described by the formation of a dipole layer at the interface with atomic dimensions. This gives rise to new interface states which have either donor or acceptor like character depending on the position of the Fermi level. The interface width δ_i is typically of the order of 1-2 Å. With this inclusion the total charge balance at the metal-semiconductor interface includes contributions from the charge in the metal, the interface states and the space-charge region in the semiconductor. Interestingly this scheme does not allow current to flow across the junction in thermal equilibrium. The immediate result of this is that the Schottky barrier height is highly dependent on the nature of the interface states.

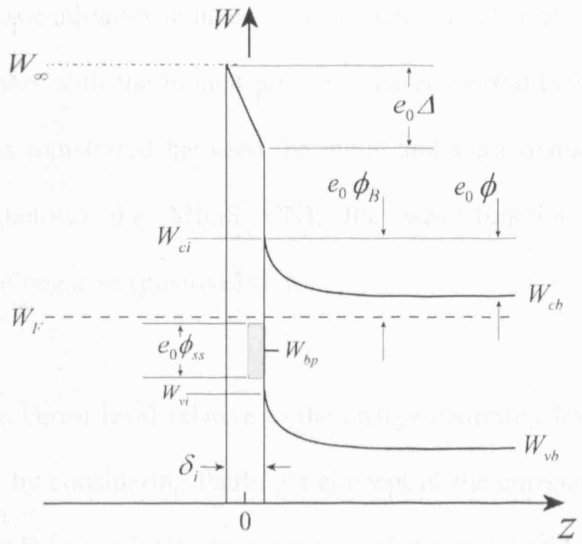

Figure 4.3. Energy diagram of the interface between a metal and an n-type semiconductor in the presence of interfacial energy states.

Bardeen [18] was the first to realise the existence of electronic interface states within the band-gap of a semiconductor Schottky junction. The condition for charge neutrality was given as:

$$Q_m + Q_s = Q_m + Q_{is} + Q_{ss} = 0 \tag{4.37}$$

The resulting energy band diagram is shown in figure 4.3. For clean metal surfaces the electron wave-functions decay exponentially into the vacuum. If this vacuum space is replaced by a semiconductor the properties of the metal wave-functions that propagate into the semiconductor are derived from the complex band structure of the semiconductor interface or virtual gap states (ViGS) [23]. These metal induced gap

states (MIGS) are an intrinsic property of the semiconductor. Their branch point, as with the intrinsic and ad-atom induced surface states, is also of importance. If the Fermi level coincides with the branch point or charge neutrality level (CNL) of the MIGS no charge is transferred between the metal and semiconductor. If the Fermi level is above (below) the MIGS CNL the wave-function decays into the semiconductor with negative (positive) sign.

The position of the Fermi level relative to the charge neutrality level of the MIGS is further understood by considering Pauling's concept of the correlation between bond ionicities and the difference in electronegativity of the metal and semiconductor. If the metal and semiconductor brought into contact have the same electronegativity no charge transfer occurs across the interface and the Fermi level will coincide with the branch point. The barrier height at the interface is then given by:

$$\phi_{bp}^{n} = W_{ci} - W_{bp} \tag{4.38}$$

If the MIGS are assumed to have a constant density of states D_{MIGS} across the band-gap the net charge density is either negative or positive when the Fermi level is above or below the MIGS branch point respectively. The net charge density may then be written as:

$$Q_{MIGS} = e_0 D_{MIGS}(W_{bp} - W_F) = e_0 D_{MIGS}(\phi_{Bn} - \phi_{bp}^{n}) \tag{4.39}$$

The net charge density Q_{MIGS} can be replaced with the electronegativity difference $(X_m - X_s)$. Chemical trends in the barrier height can then be given by:

$$\phi_{Bn} = \phi_{bp}^{n} + S_X (X_m - X_s) \tag{4.40}$$

Within this model the barrier heights are described by a zero charge transfer barrier height ϕ_{bp}^{n} and a linear gradient parameter:

$$S_X = \frac{d\phi_{Bn}}{dX_m} \tag{4.41}$$

Both quantities are characteristic of the semiconductor. The charge transfer between either side of the interface is therefore characterised by the respective electronegativity difference such that:

$$-Q_m = Q_s \propto (X_m - X_s) \tag{4.42}$$

The presence of metal induced gap states have been confirmed by a number of *ab initio* density functional methods performed for a range of semiconductors and metals. Louie and Cohen identified four different types of electronic states at the interface between Si (111) and Al jellium [24]. The first kind was found to be bulk like within both materials. The second kind were bulk like semiconductor states penetrating into the metal below the bottom of the conduction band in the metal. The third are localised interface states found within the low lying semiconductor band-gaps. The fourth are found where the metal conduction band overlaps with the semiconductor

fundamental band-gap. Metals induced gap states were found at this region to decay into the semiconductor.

4.6 Electronic Transport at Metal Semiconductor Interfaces

The transport mechanisms across metal semiconductor junctions are mainly due to majority carriers. There are four major processes that can lead to current transport under forward bias of a metal semiconductor (MS) junction [25]. Process (1) results from the transport of electrons from the semiconductor over the barrier into the metal. This is the dominant process in Schottky diodes where moderately doped semiconductors are used. For high mobility semiconductors this process is adequately described by the thermionic emission theory. In process (2) carriers are able to tunnel quantum mechanically through the barrier. This is important for heavily doped semiconductors and is often a dominant factor in Ohmic contact formation. Process (3) occurs when holes form the metal recombine with electrons within the space-charge region. This is the equivalent process to recombination in a p-n junction. Holes from the metal may also recombine with electrons within the neutral region of the semiconductor as in process (4).

4.6.1 Thermionic Emission Theory

The thermionic emission of electrons over the barrier was first described by Bethe [25,26]. It assumes that the barrier height is much larger than the thermal energy and that a thermal equilibrium is established. It is also assumed that the net current flow does

not affect the equilibrium. The current flow therefore depends solely on the barrier height. It is composed of two current fluxes, one from the semiconductor into the metal and the other from the metal into the semiconductor. In the following we consider an n-type semiconductor in contact with a metal. The current density that flows from the semiconductor into the metal may be written as (Appendix C):

$$J_{SM} = \int_{W_F + e_0\phi_B}^{W_\infty} dn\, e_0 v_z \tag{4.43}$$

$$dn = dW\, g_c(W) f_0(W) \tag{4.44}$$

Where v_z is the thermal velocity. The energy of the electrons in the conduction band can be considered as completely kinetic so that:

$$W - W_c = \tfrac{1}{2} m^* v^2 \tag{4.45}$$

$$dW = m^* v dv \tag{4.46}$$

Considering (4.14) and (4.15) equation (4.44) can be written as:

$$dn = 2\left(\frac{m^*}{h}\right)^3 \exp\left(-\frac{W_{cb} - W_F}{k_B T}\right) \exp\left(-\frac{m^* v^2}{2k_B T}\right)\left(4\pi v^2 dv\right) \tag{4.47}$$

This describes the number of electrons per unit volume with speed in the range of v to $v+dv$ for all spatial directions. To obtain the component of the drift velocity in the z direction the following transformation is applied:

$$4\pi v^2 dv = dv_x dv_y dv_z \tag{4.48}$$

The current density is therefore written as:

$$J_{SM} = 2e_0\left(\frac{m^*}{h}\right)^3 \exp\left(-\frac{W_{cb}-W_F}{k_B T}\right)\prod_{i=x,y,z}\int_{v_0}^{\infty} dv_i\, v_i \exp\left(-\frac{m^* v_i^2}{2k_B T}\right) \tag{4.49}$$

The drift velocity v_0 is the minimum velocity required for a carrier to overcome the potential barrier in the z direction. This is related to the potential ϕ through the energy relationship:

$$\tfrac{1}{2}m^* v_0^2 = e_0(\phi - V) \tag{4.50}$$

Substituting yields the following current density:

$$J_{SM} = A^* T^2 \exp\left(-\frac{e_0\phi_B}{k_B T}\right)\exp\left(-\frac{e_0 V}{k_B T}\right) \tag{4.51}$$

$$A^* = \frac{4\pi e_0 m^* k^2}{h^3} \simeq 1.2\times10^6 \frac{m^*_{n,p}}{m_0} \quad (\mathrm{A\,m^{-2}\,K^{-2}}) \tag{4.52}$$

The current flowing from the metal into the semiconductor is unaffected by the applied bias voltage. It must therefore equate to the current flowing from the semiconductor into the metal in the absence of an applied voltage. Considering equation (4.51) this may be written as:

$$J_{MS} = A^* T^2 \exp\left(-\frac{e_0 \phi_B}{k_B T}\right) \tag{4.53}$$

The transport equation for the total current density is therefore the sum of J_{SM} and J_{MS} :

$$J_n = A^* T^2 \exp\left(-\frac{e_0 \phi_B}{k_B T}\right) \exp\left(\frac{e_0 V}{k_B T} - 1\right) \tag{4.54}$$

4.6.2 Tunnelling Current

For semiconductors that are heavily doped the tunnelling current through the potential barrier may become the dominant transport process. This method of transport is often used to form Ohmic contacts to a semiconductor. The current flowing from the semiconductor into the metal is proportional to the quantum transmission coefficient and occupation probability in the semiconductor, and the unoccupied probability in the metal.

$$J_{SM} = \frac{A^* T}{k_B} \int_0^\infty T(\zeta) \exp\left(\frac{-e_0(\phi_{Bn} + \zeta - \Delta\phi)}{k_B T}\right) d\zeta + \frac{A^* T}{k_B} \int_0^{e_0(\phi - \Delta\phi)} f_s T(\xi)(1 - f_m) d\xi \tag{4.55}$$

$$J_{MS} = -\frac{A^*T}{k_B}\exp\left(-\frac{e_0\phi_{Bn}}{k_BT}\right)\int_0^{\infty} T(\zeta)\exp\left(\frac{-e_0\zeta}{k_BT}\right)d\zeta \\ -\frac{A^*T}{k_B}\int_0^{e_0(\phi-\Delta\phi)} f_m T(\xi)(1-f_s)d\xi \tag{4.56}$$

In the above $T(\zeta)$, $T(\xi)$, f_s and f_m represent the transmission coefficients above and below the potential barrier, and the Fermi-Dirac distribution functions for the semiconductor and metal respectively. The total current is given by the sum of equations (4.55) and (4.56). The tunnelling coefficient below the potential barrier generally has the form:

$$T(\xi) \simeq \exp\left(-\frac{e_0\phi_{Bn}}{E_T}\right) \tag{4.57}$$

$$E_T \equiv \frac{e_0\hbar}{2}\left(\frac{N_D}{\varepsilon_s m^*}\right)^{1/2} \tag{4.58}$$

where N_D is the donor concentration and ε_s is the permittivity of the semiconductor. It can be seen from the above that the transmission coefficient increases exponentially with the donor concentration.

4.6.3 Minority Carrier Injection

Under moderate carrier injection the metal-semiconductor junction or Schottky diode is a majority carrier device. If the forward bias voltage is sufficiently increased the contribution from minority carriers becomes significant. The ratio of minority carriers to the total current is increased due to an increase in the drift velocity component which exceeds the diffusion current. For an n-type semiconductor the continuity and current density equations for minority carriers can be written as (Appendix C):

$$\boldsymbol{J}_p = e_0 \mu_p p \boldsymbol{E} + e_0 D_p \nabla p \tag{4.59}$$

$$0 = \frac{1}{e_0} \nabla \cdot \boldsymbol{J}_p + \frac{p_n - p_{n0}}{\tau_p} \tag{4.60}$$

From the theory of rectification the minority carrier density in the semiconductor is given by:

$$p_n = p_{n0} \exp\left(\frac{e_0 V}{k_B T} - 1\right) \simeq \frac{n_i^2}{N_D} \exp\left(\frac{e_0 V}{k_B T} - 1\right) \tag{4.61}$$

In order to obtain the minority carrier density we can define a transport velocity as the ratio between the diffusion constant D_p and diffusion length L_p such that:

$$v_T = \frac{D_p}{L_p} \tag{4.62}$$

At low injection conditions the drift component of the current density in equation (4.59) is small compared to the diffusion component. If the minority carrier diffusion length is much smaller than the width of the quasi-neutral region where the recombination occurs, the minority carrier density may then be written as:

$$J_p = e_0 v_T p_n = e_0 \frac{D_p}{L_p} \frac{n_i^2}{N_D} \exp\left(\frac{e_0 V}{k_B T} - 1\right) \tag{4.63}$$

Considering equations (4.54) and (4.63) the injection ratio γ may then be written as:

$$\gamma \equiv \frac{J_p}{J_n + J_p} \simeq \frac{J_p}{J_n} = \frac{e_0 n_i^2 D_p}{N_D L_p A^* T^2 \exp(-e_0 \phi_{Bn} / k_B T)} \tag{4.64}$$

4.7 Metal Semiconductor Barrier Height Calculations

Rectification that occurs at a metal semiconductor junction is caused by the presence of a depletion layer at the semiconductor surface. A characteristic parameter of the space-charge region is the interface band bending or the barrier height ϕ_B. The barrier height of a metal semiconductor junction or Schottky diode can be evaluated from the current-voltage characteristics, capacitance-voltage characteristics, internal photoresponse and ballistic electron emission microscopy (BEEM). As mentioned in the previous sections there are four methods by which charge may travel across a

metal semiconductor junction. Of these transport mechanisms, thermionic emission is dominant at the Schottky junction for moderately doped semiconductors.

Experimentally obtained forward bias current-voltage (I-V) characteristics of semiconductors with carrier densities below 10^{18} are well described by thermionic emission over the potential barrier. The barrier heights of real MS junctions differ from those that are described by equation (4.54). Electrons that travel outside of the metal experience an image force that causes the potential barrier to be lowered by an amount proportional to the applied bias voltage. The image force lowering of the barrier height and also the barrier height will depend on the applied voltage [27]. This effect is accounted for by introducing an 'ideality factor' η into equation (4.54). The ideality factor is defined as:

$$\eta \equiv \frac{e_0}{kT}\frac{\partial V}{\partial(\ln J)} \tag{4.65}$$

In order to introduce the voltage dependence, the barrier height is expanded into a Maclaurin series yielding the following:

$$\begin{aligned} &\phi_B^{eff} = \phi_B + \frac{\partial \phi_B}{\partial e_0 V} e_0 V + \ldots = \phi_B + (1 - 1/\eta) e_0 V + \ldots \\ &\Rightarrow \\ &\phi_B = \phi_B^{eff} - (1 - 1/\eta) e_0 V \end{aligned} \tag{4.66}$$

where ϕ_n is the zero bias barrier height. Substituting into equation (4.54) yields the standard equation for thermionic emission parameterised by the effective barrier height and the ideality factor:

$$J_n = A^* T^2 \exp\left(-\frac{e_0 \phi_B^{eff}}{k_B T}\right) \exp\left(\frac{e_0 V}{\eta k_B T}\right) \tag{4.67}$$

Ideality factors are typically in the range of 1.01-1.4 and are always greater than unity due to the voltage dependence of the barrier height. Experimental I-V curves can be related directly to equation (4.67) by considering the natural logarithm of the current. By applying linear graph theory, the extrapolated intercept on the abscissa can be related to the barrier height while the gradient is related to the ideality factor.

For Schottky diodes fabricated under identical conditions variations in the barrier height and ideality factor are often found. This suggests that the barrier height depends more strongly on the applied voltage than predicted by the image force effect. The ideality factor and barrier height however do not vary randomly. One of the earliest observations of this relationship was reported by Schmitsdorf *et al.* [28] for Ag-Si Schottky diodes. They observed a linear relationship between the ideality factor and barrier height.

Capacitance voltage (C-V) measurements can also be used to determine the potential barrier height of Schottky diode. An externally applied bias alters the shape of the depletion layer and also the space-charge at the semiconductor interface. This can be understood by considering equation (4.31) for the space-charge at the semiconductor surface. The corresponding differential capacitance is obtained as:

$$C_{sc} = \frac{\partial Q_{sc}}{\partial V_{sc}} = \left\{ \frac{e_0^2 \varepsilon \left(n_{cb} + p_{vb} \right)}{2\left(e_0 \phi - k_B T - e_0 V_{sc} \right)} \right\}^{1/2} \tag{4.68}$$

Extrapolating the intercept of the abscissa of $1/C_{sc}^2$ against $V \approx V_{sc}$ yields the interface potential and hence the barrier height, according to the following for n-type and p-type semiconductors.

$$\begin{aligned} \phi_{Bn} &= \phi + \left(W_{cb} - W_F \right)/e_0 \\ \phi_{Bp} &= \phi + \left(W_F - W_{vb} \right)/e_0 \end{aligned} \tag{4.69}$$

Internal photoemission spectroscopy can also be used to calculate the barrier height of n-type Schottky diodes. Photons that have energy large than the potential barrier height can excite electrons from the metal Fermi level into the conduction band of the semiconductor. If monochromatic light is used to excite electrons from the metal Fermi level a photo current is generated providing detailed information on the surface potential barrier. This method is therefore able to measure the zero bias barrier height of metal-semiconductor junctions provided that the ideality factor corresponds to that obtained by the image force effect. Deviations from this value caused by impurity levels at the metal-semiconductor interface would lead to additional photon absorption processes. Data obtained from internal emission would require further interpretation with a knowledge of the nature of surface impurity levels.

The barrier heights of Metal-Semiconductor junctions can also be measured using ballistic electron emission microscopy (BEEM) [29]. This technique applies scanning

tunnelling electron microscopy (STEM) to spectroscopic studies of buried semiconductor interfaces with high spatial resolution (~ 1 nm). Mono-energetic electrons are injected into the metal film by tunnelling. If the mean free path of the electrons is greater than the film thickness the electrons will travel ballistically through the metal and semiconductor interface to the collector. If the mean free path of the electrons is assumed to be voltage independent, the threshold voltage for emission corresponds to the zero bias barrier height. This provides a non contact means of determining the potential barrier height. Assuming a constant tunnel current and conservation of momentum, the collector current obeys the following relationship:

$$I_{coll} = R^{-1}(V_{tip} + \phi_{Bn})^m \tag{4.70}$$

If the conduction bands of the semiconductor are assumed to be parabolic the exponent of $m = 2$ is obtained.

The chemical reaction between the deposited metal and the semiconductor surface is a well know problem hindering the formation of Schottky junctions at semiconductor surfaces. Au has been widely used to form Schottky contacts at ZnO surfaces. Other metals such as Ag, Pd and Pt have been found to form relatively high Schottky barriers in the range of 0.6-0.89 eV. Table 4.1 summarises the barrier heights and ideality factors reported for ZnO metal-semiconductor junctions. It is seen that in most cases the ideality factor is significantly greater than unity. Various explanations have been given for this such as the presence of interfacial layers [30] and tunnelling effects [31]. The origin of the enlarged ideality factors however still remains unclear.

Table 4.1. Barrier heights and ideality factors of Schottky contacts made to ZnO.

Metal	Barrier Height (eV)	Ideality Factor	Ref.
Ag	0.69	1.33	30
Ag	0.84	1.5	32
Au	0.5	1.3-1.6	33
Au	0.65	1.6-1.8	34
Pt	0.89	1.15	35
Pt	0.7	1.5	36
Pt	0.61 (as deposited)	1.70	37
Pt	0.42 (annealed)	4.29	37

4.8 Semiconductor Heterostructures

A heterojunction is formed when two (often dissimilar) semiconductors are brought into intimate contact. One of the most important types of heterostructures is the p-n junction. The basic theory of the current transport at the p-n junction was first described by Shockley [38]. Since then heterojunctions have been extensively studied and have found many important applications.

4.8.1 Energy Band Model for Semiconductor Heterostructures

The electronic properties of the junction are determined by the alignment of the energy bands across the interface and the existence of space-charge layers. As is the case for metal-semiconductor junctions, interface induced gap states (IFIGS) are present at the semiconductor-semiconductor interface. The branch point of the

interface induced gap states for both semiconductors will determine the band alignment [39]. As the bonding at a heterostructure interface is partly ionic, the valence band discontinuities are contributed to by the interface dipole layer Δ_{ss}. The valence band discontinuities at the interface can then be written as:

$$\Delta W_v = \phi_{bp1} - \phi_{bp2} + \Delta_{ss} \tag{4.71}$$

$$\Delta_{ss} = D_X (X_{s1} - X_{s2}) \tag{4.72}$$

Where ϕ_{bp} is the branch point energy and D_X is a proportionality constant. This dipole contribution describes the charge transfer between the semiconductors due to the difference in electronegativity. The average electronegativity of a binary semiconductor X_{12} may be expressed as $(X_1 X_2)^{1/2}$ [40]. As group III-V and II-VI compound semiconductors exhibit electronegativities of approximately 2 Pauling units, the dipole contribution is often neglected.

The Anderson model [41,42], developed to describe the properties of the heterojunction, makes this basic assumption in deriving the energy band discontinuities at the interface. This model can adequately explain most transport properties with only minor modifications needed to describe non-intrinsic interface states. Figure 4.4 shows the energy band diagram of the heterojunction interface between two dissimilar semiconductors where intimate contact is made.

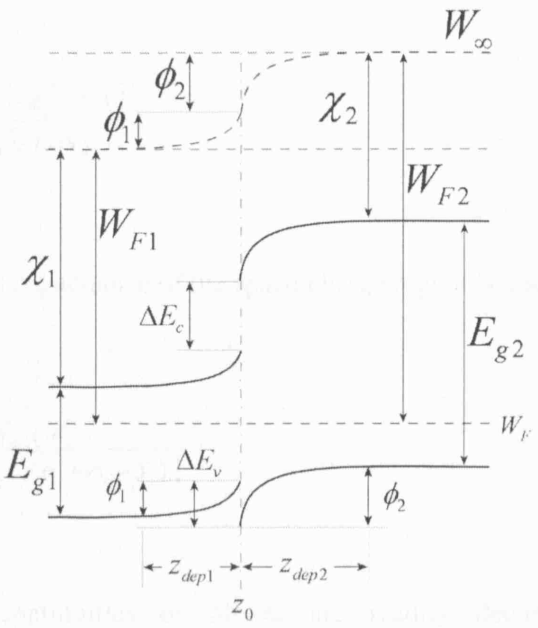

Figure 4.4. Heterojunction interface between two dissimilar semiconductors

The difference in the conduction band edges ΔE_c equates to that of the difference in electron affinity of the two semiconductors $(\chi_{s1} - \chi_{s2})$. Although this condition may not be precisely true, the choice of ΔE_c as an empirical quantity leaves the Anderson model unchanged [42]. As with the metal-semiconductor junctions described previously, when the two semiconductors are brought into intimate contact in thermal equilibrium the Fermi levels of each material must coincide. The depletion layer width can be obtained by solving Poisson's equation with boundary conditions. Adhering to the continuity of electric displacement across the interface $\varepsilon_1 E_1 = \varepsilon_2 E_2$, the depletion layer width for each material is given by:

$$z_{dep1} = \left\{ \frac{2N_{a2}\varepsilon_1\varepsilon_2(\phi_1 + \phi_2 - V)}{e_0 N_{d1}(\varepsilon_1 N_{d1} + \varepsilon_2 N_{a2})} \right\}^{1/2} \tag{4.73}$$

$$z_{dep2} = \left\{ \frac{2N_{d1}\varepsilon_1\varepsilon_2(\phi_1 + \phi_2 - V)}{e_0 N_{a2}(\varepsilon_1 N_{d1} + \varepsilon_2 N_{a2})} \right\}^{1/2} \tag{4.74}$$

The total differential capacitance of the space-charge region is also given by:

$$C = \left\{ \frac{e_0 N_{d1} N_{a2} \varepsilon_1 \varepsilon_2}{2(\varepsilon_1 N_{d1} + \varepsilon_2 N_{a2})(\phi_1 + \phi_2 - V)} \right\}^{1/2} \tag{4.75}$$

Valence band discontinuities or offsets are readily determined from X-ray Photoelectron spectroscopy (XPS). By considering the energy distance from the known excited core levels to the top of the valence band, the energy band offsets can be determined. As the escape depth of the photoelectrons is ~2 nm one of the two semiconductors must be made sufficiently thin.

4.9 Electronic Transport at Semiconductor Heterostructures

Semiconductor heterostructures can be categorised in the following manner. If the two semiconductors have the same conductivity type the junction is named an isotype heterojunction. If the two types differ (p-n junction), they are named anisotype heterojunctions.

The current voltage characteristics of a p-n heterostructure junction are derived with the following assumptions. 1. The built in potential and applied voltages are acting on

a dipole layer with abrupt boundaries. Outside the space-charge region the semiconductor is assumed to be neutral. 2. Throughout the depletion region Boltzmann statistics apply. 3. Injected minority carriers into the space-charge region are small in density compared to the majority carriers. 4. Electrons and holes are not generated by additional means (e.g. photo excitation) within the space-charge region. The total current is then given by [38]:

$$J = J_p + J_p = J_s\left(\exp(e_0 V/k_B T) - 1\right) \tag{4.76}$$

$$J_s \equiv \frac{e_0 D_p p_{n0}}{L_p} + \frac{e_0 D_n n_{p0}}{L_n} \tag{4.77}$$

The current voltage characteristics of an n-n junction are governed by the thermionic emission theory. The current voltage characteristics are given by [43]:

$$J = J_0\left(1 - \frac{V}{\phi_1 + \phi_2}\right)\left(\exp\left(\frac{e_0 V}{k_B T}\right) - 1\right) \tag{4.78}$$

$$J_0 \equiv \frac{e_0 A^* T(\phi_1 + \phi_2)}{k_B}\exp\left(-\frac{e_0(\phi_1 + \phi_2)}{k_B T}\right) \tag{4.79}$$

The above equation differs from that of the metal-semiconductor junction in that a further temperature dependence is found in J_0 . Moreover the reverse bias voltage never saturates but increases linearly with voltage for large values of V .

Summary

In summary, the properties of semiconductor surface and interfaces have been reviewed with emphasis on polar materials such as ZnO. Various electronic states are found to exist at semiconductor surfaces and metal-semiconductor interfaces. Transport properties across metal-semiconductor and semiconductor-semiconductor junctions are found to be influenced by the presence of interfacial energy states.

Reference List

[1] F. Braun, Pogg. Ann. **153**, 556 (1874)

[2] A. Schuster, Phil. Mag. **48**, 251 (1874)

[3] W. Schottky, Z. Phys. A **113**, 367 (1939)

[4] C. Davisson and L. H. Germer, Phys. Rev. **30**, 705 (1927)

[5] H. Lüth, *Solid Surfaces, Interfaces and Thin Films*, (Springer, 2001).

[6] C. B. Duke and A. R. Lubinsky, Surf. Sci. **50**, 605 (1975)

[7] M. Sambi, G. Granozzi, G. A. Rizzi, M. Casarin, and E. Tondello, Surf. Sci. **319**, 149 (1994)

[8] P. W. Tasker, J. Phys. C **12**, 4977 (1979)

[9] C. Noguera, J. Phys. : Condens. Matter **12**, R367-R410 (2000)

[10] A. Wander and N. M. Harrison, J. Chem. Phys. **115**, 2312 (2001)

[11] J. Muscat, A. Wander, and N. M. Harrison, Chem. Phys. Lett. **342**, 397 (2001)

[12] H. Maki, N. Ichinose, N. Ohashi, H. Haneda, and J. Tanaka, Surf. Sci. **457**, 377 (2000)

[13] N. Jedrecy, M. Sauvage-Simkin, and R. Pinchaux, Appl. Surf. Sci. **162-163**, 69 (2000)

[14] W. Göpel, J. Pollmann, I. Ivanov, and B. Reihl, Phys. Rev. B **26**, 3144 (1982)

[15] U. Diebold, L. V. Koplitz, and O. Dulub, Appl. Surf. Sci. **237**, 336 (2004)

[16] M. Kunat, S. Gil Girol, T. Becker, U. Burghaus, and C. Wöll, Phys. Rev. B **66**, 081402 (2002)

[17] W. Monch, *Semiconductor Surfaces and Interfaces*, pp. 67 (Springer-Verlag, 2001).

[18] J. Bardeen, Phys. Rev. **71**, 717 (1947)

[19] W. Shockley and G. L. Pearson, Phys. Rev. **74**, 232 (1948)

[20] C. G. B. Garrett and W. H. Brattain, Phys. Rev. **99**, 376 (1955)

[21] S Hassani, *Mathematical Physics*, (Springer-Verlag, New York, 1998).

[22] D. K. Ferry and S. M. Goodnick, *Transport in Nanostructures*, 1997).

[23] V. Heine, Phys. Rev. **138**, A1689 (1965)

[24] S. G. Louie and M. L. Cohen, Phys. Rev. B **13**, 2461 (1976)

[25] S. M. Sze, *Physics of Semiconductor Devices*, (Wiley, 1981).

[26] A. Many, *Semiconductor Surfaces*, (North-Holland, 1971).

[27] E. H. Rhoderick and R. H. Williams, *Metal-Semiconductor Contacts*, (Oxford University Press, 1988).

[28] R. F. Schmitsdorf, T. U. Kampen, and W. Monch, Surf. Sci. **324**, 249 (1995)

[29] M. Prietsch, Phys. Rep. **253**, 163 (1995)

[30] H. Sheng, S. Muthukumar, N. W. Emanetoglu, and Y. Lu, Appl. Phys. Lett. **80**, 2132 (2002)

[31] S. Kim, B. S. Kang, F. Ren, Y. W. Heo, K. Ip, D. P. Norton, and S. J. Pearton, Appl. Phys. Lett. **84**, 1904 (2004)

[32] S. Liang, H. Sheng, Y. Liu, Z. Huo, Y. Lu, and H. Shen, J. Cryst. Growth **225**, 110 (2001)

[33] N. Ohashi, J. Tanaka, T. Ohgaki, and H. Haneda, J. Mater. Res. **17**, 1529 (2002)

[34] A. Y. Polyakov, N. B. Smirnov, E. A. Kozhukhova, V. I. Vdovin, K. Ip, Y. W. Heo, D. P. Norton, and S. J. Pearton, Appl. Phys. Lett. **83**, 1575 (2003)

[35] S. H. Kim, H. K. Kim, and T. Y. Seong, Appl. Phys. Lett. **86**, 112101 (2005)

[36] K. Ip, B. P. Gila, A. H. Onstine, E. S. Lambers, Y. W. Heo, K. H. Baik, D. P. Norton, S. J. Pearton, S. Kim, J. R. LaRoche, and F. Ren, Appl. Phys. Lett. **84**, 5133 (2004)

[37] K. Ip, Y. W. Heo, K. H. Baik, D. P. Norton, S. J. Pearton, S. Kim, J. R. LaRoche, and F. Ren, Appl. Phys. Lett. **84**, 2835 (2004)

[38] W. Shockley, **28**, 435 (1949)

[39] J. Tersoff, Phys. Rev. B **30**, 4874 (1984)

[40] L. N. Pauling, *The Nature of the Chemical Bond*, (Cornell University Press, 1964).

[41] R. L. Anderson, Solid-State Electron. **5**, 341 (1962)

[42] W. R. Frensley and H. Kroemer, Phys. Rev. B **16**, 2642 (1977)

[43] L. L. Chang, Solid-State Electron. **8**, 721 (1965)

5. Semiconductor Surface Photovoltage

5.1 Introduction

The photovoltaic effect results from an illumination induced alteration of the distribution of charge within a material. An illumination induced change in the distribution of charge at the surface of a semiconducting material is known as the surface photovoltaic effect. This effect was first observed by Brattain in 1947 [1]. The photovoltaic effect is central to many devices that convert light into electrical charge. These include solar cells and photodetectors. Theoretical treatments of the photovoltaic effect are therefore well developed.

A theoretical treatment of surface photovoltage effects is made complicated by the range of different phenomena that must be considered. As the illumination penetration depth is finite, the density of electron-hole pairs decreases away from the semiconductor surface. Excess carriers will recombine within the space-charge region and at the surface. Surface recombination rates depend on the energy distribution of surface and interface states as well as their respective cross sections. A rigorous theoretical treatment will therefore include a large range of parameters many of which are not easily determined.

To simplify this treatment the properties of a semiconductor surface are considered where no appreciable voltage drop occurs in the quasi neutral bulk region. Moreover the penetration depth of the incident light is assumed much greater than the width of the space-charge region. Finally the width of the space-charge region is assumed to be smaller than the bulk diffusion length.

5.2 Above Band Gap Illumination

When a semiconductor is illuminated with above band gap light the probability of exciting transitions between the fundamental energy gap is much greater than that of transitions from defect or trap states. For steady state illumination the distribution of electrons and holes generally depart from equilibrium and are described quasi Fermi levels W_{Fn} and W_{Fp}. Recombination at the surface and in the space-charge region may be significantly larger than in the bulk causing the quasi Fermi levels to deviate more towards the surface. Applying Maxwell-Boltzmann statistics and considering equation (4.19) the excess carrier density $\Delta n(z)$ can be written in general as:

$$\begin{aligned} n_c(z)+\Delta n_c(z) &= N_c \exp\left(-\left[W_{cb}-W_{Fn}\right]/k_BT\right)\exp\left(-e_0\phi(z)/k_BT\right) \\ &= \gamma_n n_{cb} \exp(\upsilon(z)) \end{aligned} \tag{5.1}$$

$$\gamma_n \equiv \exp\left(\left[W_{Fn}-W_F\right]/k_BT\right) \tag{5.2}$$

$$\upsilon(z) = e_0\phi(z)/k_BT \tag{5.3}$$

Similarly for a p-type material:

$$p_c(z)+\Delta p_c(z) = \gamma_p p_{vb} \exp(-\upsilon(z)) \tag{5.4}$$

$$\gamma_p \equiv \exp\left(-\left[W_{Fp} - W_F\right]/k_B T\right) \tag{5.5}$$

Under certain conditions the quasi Fermi levels can be approximated as position independent throughout the space-charge region. The conditions for this approximation to be valid were first outlined by Garrett and Brattain [2] and are as follows. The space-charge region must be smaller than the electron and hole diffusion lengths so that the influence of non-uniform carrier excitation can be neglected. The depletion of carriers within the space-charge region must not be too extreme so that the variation in the quasi Fermi level is also negligible [3]. The flat quasi Fermi level approximation is generally acceptable provided that the illumination intensity is not large enough to cause a significant recombination current [4]. Under these assumptions the Poisson equation can be written as [5]:

$$\varepsilon \frac{d^2}{dz^2} \upsilon(z) = \frac{-e_0^2}{k_B T}\left\{n_{cb} - n_{cb}\gamma_n e^{\upsilon} - p_{vb} + p_{vb}\gamma_p e^{-\upsilon}\right\} \tag{5.6}$$

The space-charge density is then given by:

$$Q_{sc} = \varepsilon \frac{d\phi}{dz} = \varepsilon F_\gamma \tag{5.7}$$

$$F_\gamma^2 = -\frac{2k_B T}{\varepsilon}\left\{\upsilon(n_{cb} - p_{vb}) + n_{cb}\gamma_n(1 - e^{\upsilon}) + p_{vb}\gamma_p(1 - e^{-\upsilon})\right\} \tag{5.8}$$

In the absence of illumination ($\gamma_n = \gamma_p = 1$) equation (5.7) reduces to that of equation (4.31). Knowledge of the dependence of the space-charge density on the excess

carrier density is sufficient to study surface photovoltage phenomena where the surface state density is unaffected by illumination [3]. This therefore results in a fixed space-charge density for which the surface band bending decreases with increasing illumination intensity.

In a more general case the contribution from the surface states must be considered. Initial studies assumed that the surface states were in equilibrium with the semiconductor energy bands so that the Fermi-Dirac statistics apply [2]. The more complete theory based on the Shockley-Read-Hall statistics assumes a distribution of gap states [6-8] at the surface:

$$Q_{ss} = e_0\left[\sum_d \left(N_t^d - n_t^d\right) - \sum_a n_t^a\right] \tag{5.9}$$

For each surface state the electron charge carrier density n_t is given by:

$$n_t = \frac{c_n n_{cs} + c_p p_1}{c_n(n_{cs} + n_1) + c_p(p_{vs} + p_1)} N_t \tag{5.10}$$

$$n_1 = N_c \exp\left(\frac{W_t - W_c}{k_B T}\right) \tag{5.11}$$

$$p_1 = N_v \exp\left(\frac{W_v - W_t}{k_B T}\right) \tag{5.12}$$

In the above c_n (c_p) is the electron (hole) capture coefficient, $N_t = n_t + p_t$ is the surface state density and W_t is the surface state energy. Within the flat quasi Fermi level approximation, equation (5.10) can be written as:

$$n_t = \frac{c_n n_{cb} \gamma_n e^{\upsilon} + c_p p_1}{c_n (n_{cb} \gamma_n e^{\upsilon} + n_1) + c_p (p_{vb} \gamma_p e^{-\upsilon} + p_1)} N_t \tag{5.13}$$

This provides an explicit relationship between the surface potential, excess carrier density and the surface charge density. It can be seen that the change in the surface state density results form a change in the surface free carrier density. To obtain the surface potential the total charge can be considered through a perturbative treatment. Upon illumination both the surface and space-charge densities change due to carrier injection while the total charge remains constant. So we have:

$$dQ_{tot} = \frac{\partial Q_{tot}}{\partial \gamma_p} d\gamma_p + \frac{\partial Q_{tot}}{\partial \phi} d\phi = 0 \tag{5.14}$$

$\Rightarrow$

$$\Delta \phi_s \simeq -(\gamma_p - 1) \frac{\partial Q_{sc} / \partial \gamma_p + \partial Q_{ss} / \partial \gamma_p}{\partial Q_{sc} / \partial \phi_s + \partial Q_{ss} / \partial \phi_s} \tag{5.15}$$

The values within the numerator and denominator of equation (5.15) can be evaluated by considering (5.7). This dependence of the potential on the excess carrier density at the surface can be compared to experimental data provided the excess carrier density can be measured with the surface potential. A useful approximation that allows the excess minority carrier density to be obtained has been provided by Goodman [9] who

utilised the Moss equation. If the width of the space-charge region is assumed to be much smaller than the absorption α and diffusion L length and equations (C.7) and (C.12) are considered then:

$$\Delta n = \frac{I(\lambda)\alpha(\lambda)L}{(1+\alpha(\lambda)L)(S+D/L)} \tag{5.16}$$

where S is the effective drift velocity and D is the carrier diffusion coefficient. The effective photon flux I is defined as the product of the photon flux with the surface optical transmission and the quantum efficiency.

5.3 Sub band Gap Illumination

In the absence of multi-photon absorption the probability of photons with energy $h\nu < E_g$ exciting band transitions is essentially zero. It is however possible for both bulk and surface states to contribute to the surface potential. Electrons from occupied surface states below the Fermi level can be excited by sub band gap light into the conduction band. It is also possible for bulk impurity levels to be excited with sub band gap illumination. The challenge arises in separating bulk impurity state from surface state excitations. The origin of the energy states is generally determined only if the measured photovoltage is sensitive to surface properties or the crystal orientation.

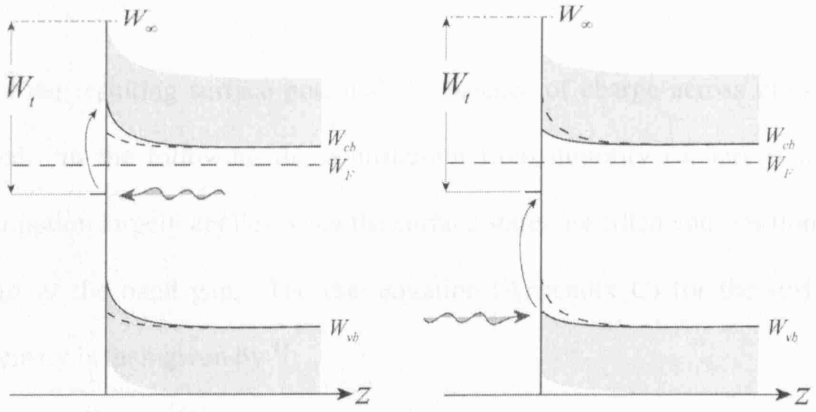

Figure 5.1. The depletion and population of surface states with sub band gap illumination for an n-type semiconductor.

In the following analysis an n-type semiconductor surface with depleted space-charge region will be considered for simplicity. The outlined methods are readily extended to p-type semiconductors and semiconductor interfaces. Figure 5.1 depict two kinds of processes that may occur under sub band gap illumination. Photons with energy $h\nu < E_c - E_t$ can cause transitions from the surface energy state E_t to the conduction band. As the potential within the space-charge region has a net positive charge the photo-excited electron is forced back into the bulk region. The result is a reduction in the surface state density and correspondingly the space-charge density. Illumination with photons of energy $h\nu > E_t - E_v$ can cause transitions from the valence band into a surface state energy level. In this case the surface state density increases and is accompanied by an increase in the space-charge density. For this process to occur some surface states must be vacant during excitation [10]. Moreover the photo generated holes tend to accumulate at the surface rather than being driven into the bulk. An understanding of the dynamics of the surface states is therefore required for quantitative analysis of this process.

To obtain the resulting surface potential the balance of charge across the surface is considered. In the following the contribution from minority carriers is neglected. This assumption largely applies when the surface states are filled and positioned in the upper part of the band gap. The rate equation (Appendix C) for the surface state charge density is then given by [11]:

$$\frac{dn_t}{dt} = -g_n^{th} - g_n^{opt} + r_n^{th} = -In_t\sigma_n^{opt} - c_n n_t n_1 + c_n(N_t - n_t)n_{cs} \tag{5.17}$$

where $g_n^{th} = c_n n_1$ is the thermal carrier generation rate, $g_n^{opt} = In_t\sigma_n^{opt}$ is the optical generation rate, $r_n^{th} = c_n n_{cs} p_t$ is the thermal recombination rate, σ_n^{opt} is the optical cross section, c_n is the electron capture coefficient and I is the photon flux. For steady state illumination conditions the surface states density due to acceptor states is then given by:

$$Q_{ss} = -e_0 n_t = -\frac{e_0 c_n n_{cs} N_t}{I\sigma_n^{opt} + c_n(n_1 + n_{cs})} \tag{5.18}$$

The surface states density is therefore obtained explicitly as a function of surface potential. Knowing this along with the space-charge density allows the surface potential to be calculated. As with above band gap illumination, the surface potential increases with increasing band bending. A larger surface state density results in an increase in the induced electron transitions and therefore a larger surface photovoltage.

5.4 Surface Photovoltage Spectroscopy

In most semiconductors there is a significant increase in the absorption coefficient near the band gap energy. A significant increase in this surface photovoltage can be expected at this energy. This has many advantages over absorption spectroscopy in that the sample can be arbitrarily thick and does not have to be grown on a transparent substrate. Surface photo Voltage spectroscopy (SPS) can also be used to determine the optimal annealing temperature of a semiconductor material. Measurements performed on CdZnTe films have showed that the surface photo voltage response increased with increasing temperature indicating an improvement in the film quality [12-14]. At a threshold temperature however the surface photo voltage began to reduce followed by a red shift in the band gap indicating that the quality of the film was degrading. Tong *et al.* have also used SPS to study the quantum size effect in nanocrystalline CdS and CdSe films [15].

Surfaces that are either depleted or inverted have their energy bands bent upward (downwards) for n-type (p-type) semiconductors. The equilibrium potential therefore differs in sign between the two types of semiconductor. As above band gap illumination generally causes a reduction in band bending, the resulting sign of the photovoltage can be used to determine the conductivity type. Measurements performed on porous p-Si have found that the conductivity type is dependent on the resistivity of the substrate used [16]. Conductivity measurement performed using SPS can be limited in their accuracy by contributions from energy states within the band

gap. Moreover if the semiconductor is not in significant depletion or inversion but has an accumulation layer the sign of the space-charge is reversed. This could quite easily lead to erroneous results.

The key advantage of surface photovoltage spectroscopy is that it is a contactless and non-destructive analysis tool that can be applied to real surfaces in the presence of an ambient atmosphere. It is therefore useful in determining the influence of the ambient on the surface properties. Studies of oxygen absorption using SPS have been reported for InP [17] and ZnO [18] surfaces. The effects of electron/ion bombardment and etching have also been studied using SPS techniques [19].

5.4.1 The Distinction between Surface and Bulk Energy States

Surface photovoltage spectroscopy (SPS) can also be used to study the relationship between surface states and interface electronic properties. This is particularly true for metal-semiconductor or Schottky junctions. The position of the Schottky barrier height is largely found to coincide with the position of the main surface and interface states observed using SPS. Effects such as Fermi level pinning by interfacial energy states are observed using SPS techniques. As bulk like energy states can be found at the semiconductor surface, SPS can be used in their study. Moreover the contribution of both bulk like states and surface states must be considered when SPS data is analysed. Distinguishing between bulk and surface states is however nontrivial. Various qualitative techniques have been suggested to overcome this problem. They include an observation of the surface potential before and after some surface treatment and a comparison with photoconductivity measurements.

A quantitative technique for distinguishing between surface and bulk like states proceeds as follows [20]. Considering equations (4.8), (4.31) and (4.35) the potential at the surface may be written as:

$$\phi_s = -\frac{Q_{ss}^2}{2\varepsilon\rho} \tag{5.19}$$

It can be assumed that illuminating the surface results in a change of the surface population density. We can therefore consider the incremental change in the surface state and space-charge density so that the surface photovoltage is given by:

$$(\phi_s^0 - \phi_s) = -\frac{1}{2\varepsilon}\left[\frac{(Q_{ss}+\delta Q_{ss})^2}{\rho+\delta\rho} - \frac{Q_{ss}^2}{\rho}\right] \tag{5.20}$$

If the illumination only influences the surface charge states while the bulk states are unaltered the space-charge density remains constant ($\delta\rho = 0$). Conversely if the surface state density is fixed and the space-charge density is altered by the illumination then $\delta Q_{ss} = 0$. It therefore follows that:

$$(\phi_s^0 - \phi_s) = -\frac{\delta Q_{ss}\left(2Q_{ss}+\delta Q_{ss}\right)}{2\varepsilon\rho}, \text{ for fixed bulk like states} \tag{5.21}$$

$$(\phi_s^0 - \phi_s) = \frac{\delta\rho\, Q_{ss}^2}{2\varepsilon\rho(\rho+\delta\rho)}, \qquad \text{for fixed surface states} \tag{5.22}$$

From the above it can be seen that the dependence of the surface photovoltage on the surface state density δQ_{ss} is super-linear (5.21) while the dependence on the charge-density $\delta\rho$ is sub-linear (5.22). As both quantities depend on the illumination intensity which may itself be sub-linear, an observation of sub-linear photovoltage does not provide a definitive indication of the presence of surface states. If however a super-linear dependence is observed over an interval of the SPV spectrum then surface states are present. Leibovitch *et al.* [20] have confirmed this model with measurements performed on InP samples. They used defective samples which are dominated by surfaces states along with Fe doped samples dominated by bulk states. Their results clearly show a super-linear increase in surface photovoltage due to surface states which cannot be observed for samples dominated by bulk states.

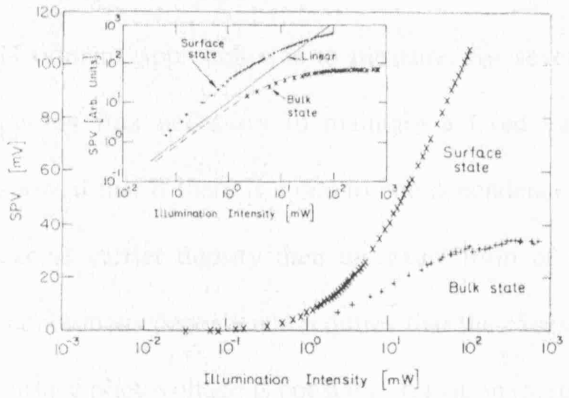

Figure 5.2. Dependence of the surface photovoltage on the illumination intensity for bulk InP with predominantly surface or bulk like states. The same data is shown on a logarithmic scale in the inset [20].

5.4.2 Carrier Diffusion Length

One of the most important applications for surface photovoltage spectroscopy is the measurement of the minority carrier diffusion length L . This technique relies on the Moss equation given in (5.16). Moss had originally suggested that L could be extracted for small signal levels where the surface photovoltage is proportional to the excess carrier density [9,21]. Moreover it was suggested that the excess carrier density was maximal when the absorption coefficient α is large. This occurs with short wavelength illumination. As the surface photovoltage is half its maximum value when $\alpha(\lambda)L = 1$, the value of L can be obtained by measuring α at that wave length. This technique however is limited in that the maximum value of the surface photovoltage must be known. This is often problematic as it is not always possible to accurately identify the maximum surface photovoltage. Moreover a large dynamic range of wave lengths may be required to identify the maximum and half maximum surface photovoltage.

Goodmans approach was to measure, for several above band gap wavelengths, the photon flux necessary to maintain a fixed value for surface photovoltage [9]. He showed that if there is a one to one dependence for the surface photovoltage with the excess carrier density then the exact form of this relation was not required. This monotonous dependence requires that the excess carrier density is constant when the surface photovoltage is constant. Equation (5.16) then becomes:

$$\frac{\alpha(\lambda)L}{1+\alpha(\lambda)L}\frac{1}{S+D/L}I(\lambda) = \text{const.} \tag{5.23}$$

This can be rewritten as:

$$I(\lambda) = \text{const} \cdot (\alpha^{-1}(\lambda) + L) \tag{5.24}$$

From the above evaluation of the intercept with the abscissa of a plot of $I(\lambda)$ against $\alpha^{-1}(\lambda)$ allows L to be determined. The advantage of using the surface photovoltage technique is that it provides a quasi equilibrium approach to determining the diffusion length which is not influenced by time constants brought about by bulk and surface processes. Changes brought about by such processes are manifested in the surface recombination velocity S. From equation (5.16) it can be seen that changes in S serve to alter the gradient of the curve used to obtain L but not the intercept with the abscissa.

This process for extracting the carrier diffusion length isn't without limitation. The Goodman equation assumes that the width of the space-charge region is accurately described by the approximation of equation (4.35). This assumption is however found to be valid for free surfaces and Schottky contacts. If the surface potential is very small, the space-charge region current components may be of the same order of magnitude as the minority diffusion current. Under the assumptions used in obtaining equation (5.23), this will lead to significant errors in the determination of the minority carrier diffusion length. The effective photon flux $I(\lambda)$ is composed of the photon flux with the surface optical transmission and the quantum efficiency. Variations in the optical transmission may lead to an inaccurate prediction of the effective photon flux and hence the carrier diffusion length. While this effect is usually negligible, its effect has been observed [22].

Surface photovoltage measurements have, however, been performed successfully on a number of important semiconductor materials including GaAs [9], CdSe [23], ZnSe [24] and ZnO [25].

Summary

In summary the surface photovoltage (SPV) of a semiconductor can be measured by illumination. This experimental method is however sensitive to the surface properties and the properties of the space-charge region beneath the surface. Information can therefore be gained on the electronic properties of both the surface and interfaces of a semiconductor material in addition to the bulk properties.

Reference List

[1] W. H. Brattain, Phys. Rev. **72**, 345 (1947)

[2] C. G. B. Garrett and W. H. Brattain, Phys. Rev. **99**, 376 (1955)

[3] A. Many, *Semiconductor Surfaces*, (North-Holland, 1971).

[4] D. R. Frankl, Surf. Sci. **3**, 101 (1965)

[5] W. Monch, *Semiconductor Surfaces and Interfaces*, pp. 67 (Springer-Verlag, 2001).

[6] C. G. B. Garrett and W. H. Brattain, **35**, 1041 (1956)

[7] W. H. Brattain and C. G. B. Garrett, **35**, 1019 (1956)

[8] W. Shockley and W. T. Read, Phys. Rev. **87**, 835 (1952)

[9] A. M. Goodman, J. Appl. Phys. **32**, 2550 (1961)

[10] J. Lagowski, C. L. Balestra, and H. C. Gatos, Surf. Sci. **27**, 547 (1971)

[11] L. Szaro, Appl. Phys. A **V29**, 201 (1982)

[12] A. Rohatgi, S. A. Ringel, R. Sudharsanan, P. V. Meyers, C. H. Liu, and V. Ramanathan, Solar Cells **27**, 219 (1989)

[13] A. Rothschild, A. Levakov, Y. Shapira, N. Ashkenasy, and Y. Komem, Surf. Sci. **532-535**, 456 (2003)

[14] M. Buchel and H. Luth, Surf. Sci. **50**, 451 (1975)

[15] Xiao Tong, *et al.*, High-pressure science and technology, AIP 309 , (1994), pp.1271-1274

[16] L. Burstein, Y. Shapira, J. Partee, J. Shinar, Y. Lubianiker, and I. Balberg, Phys. Rev. B **55**, R1930 (1997)

[17] S. M. Thurgate, K. Blight, and T. D. Laceusta, Surf. Sci. **310**, 103 (1994)

[18] J. Lagowski, J. Sproles, and H. C. Gatos, J. Appl. Phys. **48**, 3566 (1977)

[19] L. J. Brillson, Y. Shapira, and A. Heller, Appl. Phys. Lett. **43**, 174 (1983)

[20] M. Leibovitch, L. Kronik, E. Fefer, and Y. Shapira, Phys. Rev. B **50**, 1739 (1994)

[21] R. H. Bube, *Photoconductivity of Solids*, (Krieger, 1978).

[22] M. Hack, J. McGill, W. Czubatyj, R. Singh, M. Shur, and A. Madan, J. Appl. Phys. **53**, 6270 (1982)

[23] G. J. Storr and D. Haneman, J. Appl. Phys. **58**, 1677 (1985)

[24] S. Mora, N. Romeo, and L. Tarricone, Solid State Commun. **33**, 1147 (1980)

[25] L. Yanhong, W. Dejun, Z. Qidong, Y. Min, and Z. Qinglin, J. Phys. Chem. B **108**, 3202 (2004)

6. ZnO Tetrapod Nanocrystals

6.1 Introduction

The study of low-dimensional self assembled nanostructures has intensified in recent years due to significant advancements in their synthesis. Nanocrystals formed from metals, group III-V and II-VI semiconductors are readily synthesised using techniques ranging from chemical vapour transport to molecular beam epitaxy. Materials such as Au, Ag, InSnO, GaN, ZnS, ZnO, CdS, CdSe and CdTe have been grow as nanowires [1], nanorods [2-4], nanoribbons [5] and nanoscale branched structures [6-8]. It is hoped that these building blocks will form the basis of many novel materials and devices that exploit various physical effects, such as quantum confinement, which occur at the nanoscale. Semiconducting nanocrystals are expected to find applications ranging from drug delivery systems [9] to photovoltaic devices [10].

Branched nanostructures have been synthesised using CdSe, CdTe, ZnS and ZnO. The simplest of these structures is the tetrapod [7,8,11-13]. This consists of four rod shaped structures joined at tetrahedral angles to an octahedral core [14,15]. These nanocrystals therefore orientate spontaneously with one 'arm' directed normal to the plane of the substrate. Alivisatos and co workers have demonstrated the synthesis of branched CdTe tetrapod structures [16]. These structures result from nucleation of a cubic zincblende quantum dot with subsequent anisotropic growth of hexagonal wurtzite nanorods.

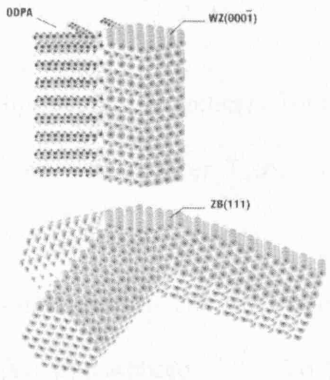

Figure 6.1. Proposed model of a CdTe tetrapod (Manna *et al.* [16]). Sectioned view of one arm illustrates the identical nature of the (111) zinc blende and (0001) wurtzite facets of the nucleus and the arms, respectively. Phosphonic acid molecules selectively bind to the lateral facets of the arms, as suggested in the figure (for clarity, only two facets are shown covered).

The ability to selectively grow branch points of a different material onto existing tetrapod structures has also been demonstrated. Using crystal phase control techniques for CdSe and CdTe, Milliron et al. [8] have also shown the ability to independently tune the separate components of the tetrapod nanostructure. This allowes branched or linear junctions to be formed at any point during the growth process.

ZnO forms a richly diverse family of nanostructures that also includes the tetrapod nanocrystal [5,7]. Much like their CdTe variant, ZnO tetrapods (ZnO-T) consist of a four hexagonal wurtzite rods joined at tetrahedral angles to a octahedral zincblende core. Many of the properties of ZnO-T are inherent from the bulk material. ZnO is however unique as it exhibits both piezoelectric and semiconducting properties.

6.2 The Synthesis of ZnO Tetrapod Nanocrystals

In this section a general route to the synthesis of ZnO tetrapod nanocrystals is outlined. In chapter 7 the method that we have used to synthesis ZnO tetrapod nanocrystals is described.

ZnO nanocrystals can be prepared through the evaporation of pure zinc powder in an oxygen atmosphere [13,17]. To gain more control over the growth conditions, ZnO tetrapods are more commonly synthesised in a horizontal tube furnace. In this setup, the source material, a mixture of C and a Zn containing compound, is placed in the centre of the furnace. The furnace is then heated to 900 °C in a flow of either Ar or N_2 with an O_2 partial of 0.5-5 %. At 900 °C a carbothermal reduction process releases supersaturated Zn which condenses downstream to form ZnO tetrapod nanocrystals. A Si substrate is mounted downstream at the 600 °C region to collect the growth constituents.

Yu *et al.* synthesised ZnO tetrapod nanocrystals using a 3:2 weight ratio of zinc carbonate and graphite powder and an Ar/O_2 gas flow rate of 500 sccm [18]. They placed a series of baffles in the downstream region of the quartz tube to assist in vapour mixing process. Figure 6.2 shows a region of the substrate after the growth process. Its can be seen that there is a high yield of tetrapod nanocrystals with large surface coverage.

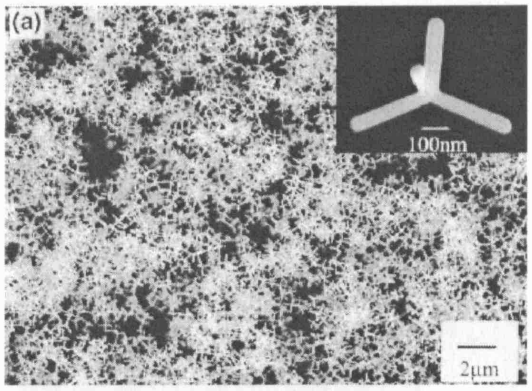

Figure 6.2. Scanning electron micrograph of ZnO tetrapod nanocrystals grown by Yu *et al.* [18]. Inset shows a single ZnO tetrapod nanocrystal.

Conversely Chen *et al.* have synthesised ZnO tetrapod nanocrystals at 950 °C using a 1:1 molar ratio of ZnO and graphite powder. Synthesis was carried out in an N_2/O_2 flow of 20-90 sccm. They found that more uniform tetrapod structures were formed with an increase in flow rate. Figure 6.3 shows an SEM image of ZnO tetrapods grown using this method. It can be seen that all the tetrapods are well facetted and have hexagonal cross-sectional arms. Moreover they found that by reducing the distance between the source material and the substrate by 20 mm, they were able to grow larger tetrapod nanocrystals. As there is little variation in the temperature of the sample at this length scale, the increase in the nanocrystal size is attributed to an increase in the supersaturated Zn.

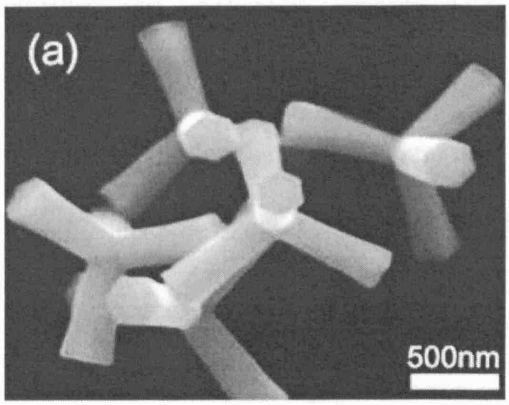

Figure 6.3. Scanning electron micrograph of ZnO tetrapod nanocrystals grown by Chen *et al.* [15].

It is generally accepted that the growth of ZnO nanocrystals occurs through a vapour-liquid-solid growth mechanism [14,19,20]. We understand the nucleation and growth of ZnO-T to occur in the vapour phase during synthesis. The growth process proceeds with the carbothermal reduction of zinc carbonate at elevated temperatures. This reaction has the following form:

$$ZnCO_3 \xrightarrow{heat} ZnO + CO_2 \tag{6.1}$$

The carbon within the mixture is then able to promote a deoxidisation reaction in which large amounts of sub-oxides of zinc are formed:

$$ZnC + C\,(CO) \rightarrow ZnO_x + CO_2 \tag{6.2}$$

For growth via ZnO source material, carbothermal reduction causes sub-oxides to form directly. This supersaturated zinc is then transported by the O_2 containing carrier gas toward the cooler region at which point the nucleation of ZnO nanocrystals is favoured. From these nuclei, cylindrical arms grow from the vapour phase along the (0001) axis.

6.3 Transmission Electron Microscopy Studies on ZnO Tetrapods

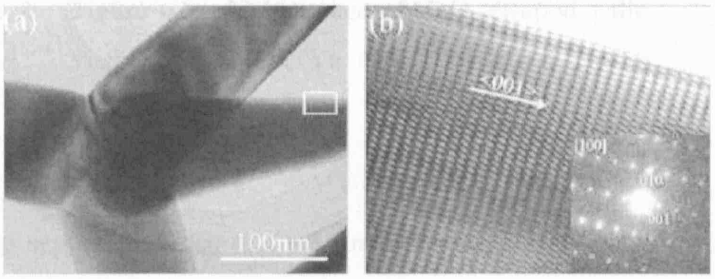

Figure 6.4. TEM and HRTEM image of ZnO tetrapod nanocrystal showing the growth direction along the (0001) axis (Wang et al. [13]).

High resolution transmission electron microscopy (TEM) studies were performed by Wang *et al.* on ZnO tetrapods grown using rapidly heating Zn powder in air [13]. Figure 6.4b shows a HRTEM image of the arm of a ZnO-T. From this image a lattice spacing of 2.59 Å is obtained which corresponds to the (0002) plane of wurtzite ZnO. This, along with the selected area diffraction (SAD) pattern shown in the inset, indicates that each arm grows preferentially along the (0001) direction.

Using transmission electron microscopy (TEM), Yu et. al.[18] have revealed the presence of a tetrahedral zinc blend core from which each arm of the tetrapod grows (Figure 6.5).

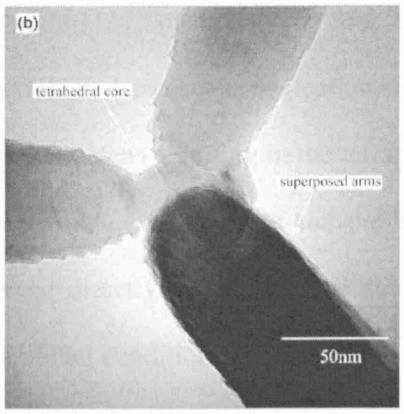

Figure 6.5. TEM image of ZnO tetrapod with visible core region (Yu et al. [18]).

These finding support the idea that the formation of the tetrapod structure proceeds via the nucleation of a zincblende core from which the tetrapod forms. Moreover it has been shown that ZnO tetrapods may be synthesized using pre-deposited nanocrystals as nuclei from which the tetrapod structure may grow. It has also been shown that nanocrystals deposited onto a substrate may act as nuclei for tetrapod synthesis [21].

6.4 The Crystal Structure of ZnO tetrapods

A number of models have appeared in the literature to describe the formation of ZnO tetrapods. It is commonly suggested that growth of the cylindrical arms proceeds via the nucleation of a core structure [22-24]. These models however differ in their choice

of the crystal structure of the core. Shiojiri *et al.* [22] have suggested a growth model in which the nucleus of the tetrapod is a single crystal zinc-blende octahedral nanocrystal terminated by eight [111] surfaces. The four Zn terminated surfaces are more reactive than the O terminated and act as nucleation sites for hexagonal wurtzite nanorods which overgrow the nucleus resulting in the tetrapod structure. This model is lacking in that the cubic structure of the core and the interface between the two phases has not been observed directly. Moreover the zinc-blende phase of ZnO is especially unstable under ambient conditions.

Probably the most successful model to date, owing to its agreement with crystallographic measurements [14], is the octa-twin model of Takeuchi *et al.* [25]. In this model the ZnO nucleus is formed from eight tetrahedral shaped crystals each with three $(11\bar{2}2)$ pyramid facets and one (0001) basal plane facet (Figure 6.6). These eight tetrahedrons can then be joined together to form a single octahedron where each basal plane forms a facet of the structure. The properties of each adjacent tetrahedron are antisymmetric with respect to their exchange. The basal planes thus alternate between both (0001) and $(000\bar{1})$ surfaces. As (0001) Zn terminated surfaces are the most reactive, preferential growth at these points is expected. It is however not possible to construct a perfect octahedral pyramid from such trigonal pyramids as the angle between each $(11\bar{2}2)$ plane is smaller than 90°. Although this model is able to adequately describe the observed crystal geometry, no measurements to date have directly shown that such an octahedral structure exists at the tetrapod core. It is therefore required that more detailed studies on the tetrapod crystal structure are carried out before any conclusion as to which is the correct model can be made.

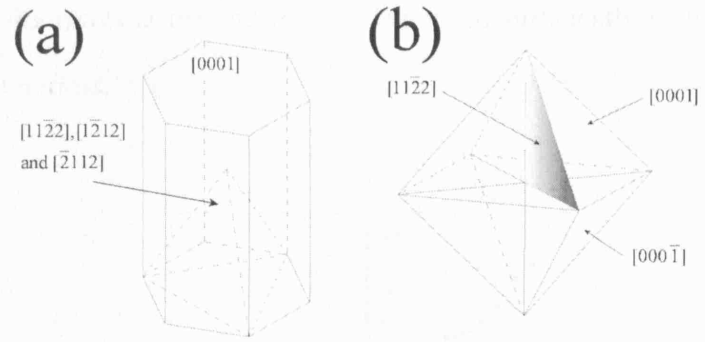

Figure 6.6. A pyramid formed by three $(11\bar{2}2)$ and one $(000\bar{1})$ facets (a). The octa-twin model consisting of eight antisymmetrised pyramidal crystals (b) (Dai *et al.* [14]).

6.5 Optical and Electronic Properties of ZnO Nanocrystals.

Among the most interesting features of ZnO nanocrystals are their optical properties. Optically pumped lasing has been observed in a number of ZnO nanocrystals [26-28] and was first demonstrated for ZnO nanorods by Huang *et al.* in 2001. They saw a simultaneous increase in photoluminescence intensity and decrease in line width at a wavelength of 385 nm when the optical pump energy exceeded a threshold, consistent with the onset of lasing in the ZnO nanorods.

Since then other groups have demonstrated optically-pumped stimulated emission from both clusters and individual ZnO tetrapods [29-31]. By measuring the wavelength spacing of adjacent optical resonant modes (Figure 6.7) Szarko *et al.* tentatively conclude that a Fabry-Perot resonant cavity for ultra-violet photons is formed by each individual arm of the single irradiated tetrapod [32]. This in turn suggests that the

$(000\bar{1})$ wurtzite facets at the end of each leg act as sufficiently high quality ultra-violet optical mirrors.

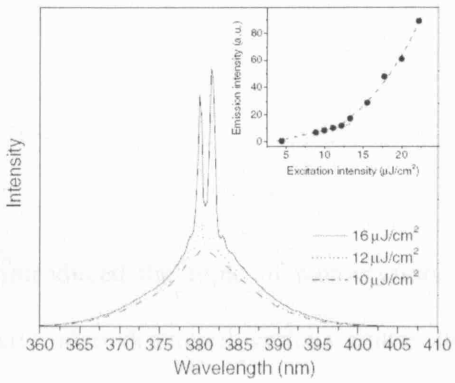

Figure 6.7. Excitation intensity dependence of the emission and lasing spectra of a ZnO tetrapod with 267 nm excitation. The broad photoluminescence is observed at low excitation intensity. As the excitation intensity increases above the lasing threshold, sharp lasing peaks grow at several wavelengths. The inset shows the super-linear increase of the emission intensity above the lasing threshold (Szarko *et al.* [32]).

In our own measurements of the photoluminescence spectra of ZnO tetrapods [7] we see quite a different response from a cluster of randomly-oriented tetrapods and a single tetrapod which has one arm aligned parallel with the incident laser beam. These results are discussed in later chapters.

The electronic transport properties of ZnO tetrapods are, by comparison with their optical properties, far less studied. This arises from technological difficulties in

making electrical contacts to the nanocrystals. In chapter 8 a route to fabricating a diode structure that employed a single ZnO tetrapod nanocrystal is described [33,34].

Summary

In summary we have introduced the topic of nanocrystals and the family of ZnO nanostructures. We have also discussed various routes to the synthesis of ZnO tetrapod nanocrystals. It has been shown that the size and morphology of these structures is sensitive to the growth parameters and may be controlled by varying parameters such as the oxygen partial pressure and the synthesis temperature. A number of models for the crystal structure of the ZnO tetrapod nanocrystal have been proposed. It however remains unclear as to which is correct owing to a lack of more rigorous measurements.

Reference List

[1] W. B. Zhao, J. J. Zhu, and H. Y. Chen, J. Cryst. Growth **258**, 176 (2003)

[2] Y. Q. Chen, J. Jiang, B. Wang, and J. G. Hou, J. Phys. D: Appl. Phys. **37**, 3319 (2004)

[3] C. M. Park, Y. S. Park, H. Im, and T. W. Kang, Nanotechnology **17**, 952 (2006)

[4] Y. W. Heo, D. P. Norton, L. C. Tien, Y. Kwon, B. S. Kang, F. Ren, S. J. Pearton, and J. R. LaRoche, Mater. Sci. Eng. Rep. **47**, 1 (2004)

[5] Z.L.Wang, X.Y.Kong, Y.Ding, P.Gao, W.L.Hughes, R.Yang, and Y.Zhang, Adv. Func. Mater. **14**, 943 (2004)

[6] M. Chen, Y. Xie, J. Lu, Y. J. Xiong, S. Y. Zhang, Y. T. Qian, and X. M. Liu, J. Mater. Chem. **12**, 748 (2002)

[7] M. C. Newton, S. Firth, T. Matsuura, and P. A. Warburton, J. Phys. Conf. Ser. **26**, 251 (2006)

[8] D. J. Milliron, S. M. Hughes, Y. Cui, L. Manna, J. Li, L. W. Wang, and A. Paul Alivisatos, Nature **430**, 190 (2004)

[9] T. Pellegrino, S. Kudera, T. Liedl, I. M. Javier, L. Manna, and W. J. Parak, Small **1**, 48 (2005)

[10] S. E. Shaheen, D. S. Ginley, and G. E. Jabbour, MRS Bulletin **30**, 10 (2005)

[11] L. Manna, E. C. Scher, and A. P. Alivisatos, J. Am. Chem. Soc. **122**, 12700 (2000)

[12] J. Gong, S. Yang, H. Huang, J. Duan, H. Liu, X. Zhao, R. Zhang, and Y. Du, Small **2**, 732 (2006)

[13] F. Z. Wang, Z. Z. Ye, D. W. Ma, L. P. Zhu, and F. Zhuge, Mater. Lett. **59**, 560 (2005)

[14] Y. Dai, Y. Zhang, and Z. L. Wang, Solid State Commun. **126**, 629 (2003)

[15] Z. Chen, Z. W. Shan, M. S. Cao, L. Lu, and S. X. Mao, Nanotechnology **15**, 365 (2004)

[16] L. Manna, D. J. Milliron, A. Meisel, E. C. Scher, and A. P. Alivisatos, Nature Mater. **2**, 382 (2003)

[17] Y. Dai, Y. Zhang, Q. K. Li, and C. W. Nan, Chem. Phys. Lett. **358**, 83 (2002)

[18] W. D. Yu, X. M. Li, and X. D. Gao, Chem. Phys. Lett. **390**, 296 (2004)

[19] Y. Y. Wu and P. D. Yang, J. Am. Chem. Soc. **123**, 3165 (2001)

[20] H. Yan, R. He, J. Pham, and P. Yang, Adv. Mater. **15**, 402 (2003)

[21] W. D. Yu, X. M. Li, and X. D. Gao, J. Cryst. Growth **270**, 92 (2004)

[22] M. Shiojiri and C. Kaito, J. Cryst. Growth **52**, 173 (1981)

[23] K. Nishio, T. Isshiki, M. Kitano, and M. Shiojiri, Philos. Mag. A **76**, 889 (1997)

[24] H. Iwanaga, M. Fujii, and S. Takeuchi, J. Cryst. Growth **134**, 275 (1993)

[25] S. Takeuchi, H. Iwanaga, and M. Fujii, Philos. Mag. A **69**, 1125 (1994)

[26] M. H. Huang, S. Mao, H. Feick, H. Q. Yan, Y. Y. Wu, H. Kind, E. Weber, R. Russo, and P. D. Yang, Science **292**, 1897 (2001)

[27] K. Bando, T. Sawabe, K. Asaka, and Y. Masumoto, J. Lumin. **108**, 385 (2004)

[28] H. Q. Yan, J. Johnson, M. Law, R. R. He, K. Knutsen, J. R. McKinney, J. Pham, R. Saykally, and P. D. Yang, Adv. Mater. **15**, 1907 (2003)

[29] Y. H. Leung, W. M. Kwok, A. B. Djurisic, D. L. Phillips, and W. K. Chan, Nanotechnology **16**, 579 (2005)

[30] W. M. Kwok, A. B. Djurisic, Y. H. Leung, W. K. Chan, and D. L. Phillips, Appl. Phys. Lett. **87**, 223111 (2005)

[31] A. B. Djurisic, W. M. Kwok, Y. H. Leung, W. K. Chan, D. L. Phillips, M. S. Lin, and S. Gwo, **17**, 244 (2006)

[32] J. M. Szarko, J. K. Song, C. W. Blackledge, I. Swart, S. R. Leone, S. H. Li, and Y. P. Zhao, Chem. Phys. Lett. **404**, 171 (2005)

[33] M. C. Newton, S. Firth, and P. A. Warburton, Appl. Phys. Lett. **89**, 072104 (2006)

[34] M. C. Newton, P. A. Warburton, and S. Firth, Nanotechnology, Sixth IEEE Conference on, IEEE 2 , (2006), pp.453-456

Experimental Work on ZnO Tetrapod Nanocrystals

7. Characterisation of ZnO Tetrapod Nanocrystals

7.1 Introduction

In the previous chapter the topic of semiconductor nanocrystals was introduced with particular emphasis on ZnO tetrapod nanocrystals. Here we focus on the work that we have carried out on ZnO tetrapod nanocrystals. This begins with the route that we have taken for the synthesis of ZnO tetrapods. We then move onto the characterization of ZnO tetrapod (ZnO-T) nanostructures that we have synthesised. A number of techniques for the study of both macroscopic clusters and individual nanocrystals are introduced.

7.2 A Route to the Synthesis ZnO Tetrapod Nanocrystals

In this section the method that we have used to synthesise ZnO tetrapod nanocrystals is reviewed. This is in many ways similar to that described in section 6.2 in that synthesis proceeds via a carbothermal reduction process.

To achieve control over the size and morphology of the constituents, the synthesis of ZnO tetrapods is routinely carried out in a horizontal quartz tube furnace via chemical vapour transport and deposition (CVTD) [1]. An image of the furnace is shown in figure 7.1. Figure 7.2 shows the temperature profile of the furnace as a function of distance form the central region. This measurement was performed using a thermocouple while maintaining a N_2 flow rate of 500 sccm. The source material

consists of a mixture of zinc carbonate powder ($ZnCO_3 \circ 2Zn(OH)_2 \circ H_2O$) and graphite powder. This is finely mixed in a weight ratio of 5:1. A crucible containing the mixture is placed in the central region of the quartz tube furnace. A bare Si substrate is then mounted in the down stream region to harvest the growth constituents. This corresponds to the 600°C region during the synthesis process. We have grown tetrapod nanocrystals with both Ar and N_2 carrier gas and have observed little difference in the growth constituents. We have therefore carried out our studies using a N_2 carrier gas with an oxygen content of 0.5 – 5%. This was maintained at a flow rate 500 sccm while the furnace is heated up to 900°C. At 900°C a carbothermal reduction process causes supersaturated Zn vapour to be released for subsequent oxidation. After 30 minutes reaction period, a thin layer of white fluffy material is visible on the substrate surface.

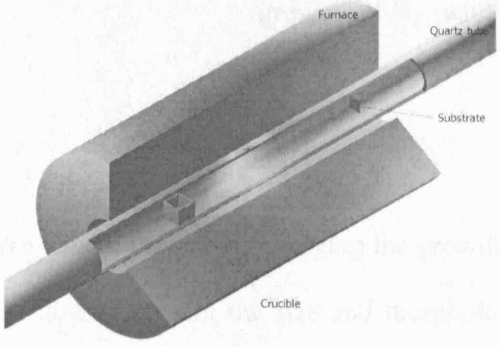

Figure 7.1. Schematic of CVTD synthesis apparatus. The gas flow is from left to right within the quartz tube.

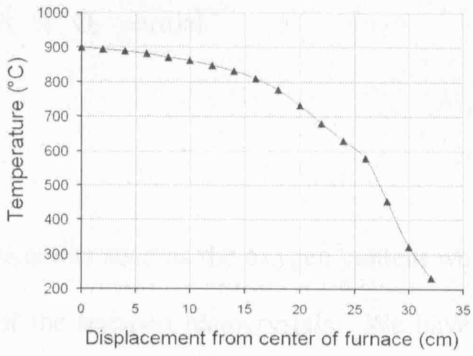

Figure 7.2. Temperature profile of horizontal quartz tube furnace at an Ar flow rate of 500 sccm.

Figure 7.3 shows a scanning electron micrograph image of a ZnO tetrapod nanocrystal grown in N_2 at 500 sccm with a 3% O_2 partial presure. From the image it can be seen that each arm is well faceted and is uniform in length and diameter. X-ray diffraction analysis confirms that our ZnO-T nanocrystals condense into the wurtzite crystal structure (Section 7.3).

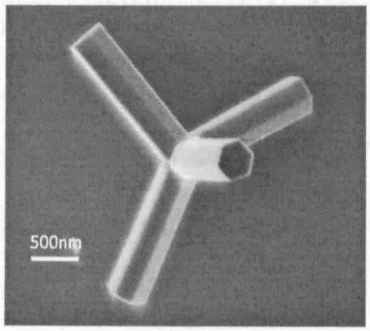

Figure 7.3. SEM image of ZnO tetrapod grown in N_2 with a 3 % O_2 paritial pressure.

We have found that by varying the growth parameters such as the oxygen content we are able to control the size and morphology of the tetrapod nanocrystals. We have synthesised uniform ZnO-T with arm lengths of 200 nm to 10 μm and cross sectional widths of 50 nm to 500 nm by varying the growth conditions. Figure 7.4 shows the various types of ZnO tetrapods that we have synthesised.

A zinc carbonate to carbon ratio of 5:1 is able to produce a high yield of ZnO-T. The arm diameters typically range from 100 – 500 nm. Tetrapods are found with longer arms and tend to have larger arm diameters (Fig. 7.4a) as the substrate is moved to a

higher temperature region. Beyond the temperature region of 750°C tetrapod structures are no longer formed and block-like structures persist. At temperatures below 600°C, a mixture of ZnO rods and tetrapods are formed. The amount of carbon available for the reaction greatly influences the vapour transport of ZnO within the quartz tube and hence the density of supersaturated Zn. At low oxygen content (< 1 %), tetrapods are grown with needle shaped arms as shown in figure 7.4b where an oxygen content of 5 sccm is used. At low oxygen content, smaller tetrapods tend to forms at lower temperature regions (Fig. 7.4c) and regain their cylindrical arm shape. As the oxygen content is increased from 0.5 – 10 %, ZnO-T are found with increased arm lengths (200 – 6000nm) and diameters (100 – 1000 nm). At higher temperature regions, tetrapods with trumpet shaped arms form under high oxygen content. This is shown in figure 7.4d for 700 sccm N_2 and 45 sccm O_2 at a temperature region of 700 °C. If the oxygen content is further increased, the majority of C used within the experiment becomes oxidised and the reaction will not proceed. Oxygen can be therefore introduced at elevated temperatures (600-700 °C) to limit the amount of carbon that is oxidised. Conversely more carbon can be used if the intention is to grow larger crystals. If the flow rate is increased above 700 sccm, ZnO dendrite structures are found on the substrate surface.

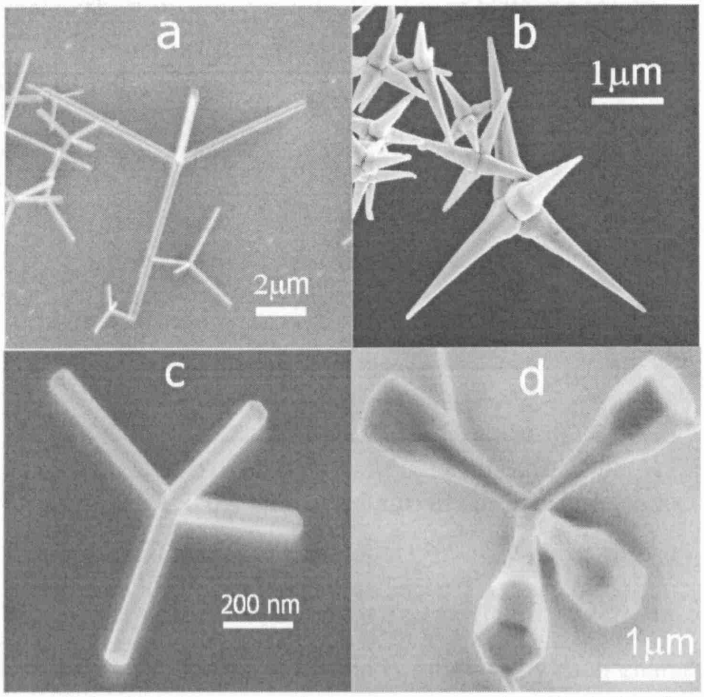

Figure 7.4. SEM images of ZnO nanocrystals. Variation in the growth constituents is achieved by altering the growth parameters.

7.3 X-Ray Diffraction

Electromagnetic X-rays have wavelengths of the order of a few angstroms, comparable to interatomic distances in crystalline solids. Incident x-rays can be diffracted by crystalline materials which by definition has regularly repeating atomic structures. When a monochromatic X-ray beam of wavelength λ is projected onto a crystalline material at an angle θ, diffraction occurs only when the distance travelled by the photon reflected from successive crystal planes differs by an integer n number of wavelengths. If this condition is not met, the reflected wave will interfere such that cancellation occurs. The condition for Bragg reflection may be written in its familiar form [2]:

$$n\lambda = 2d \sin\theta \tag{7.1}$$

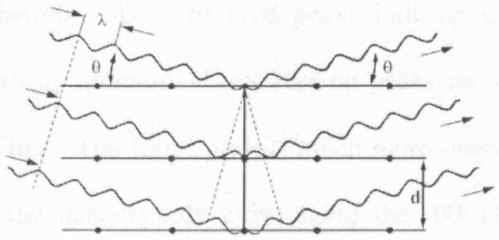

Figure 7.5. Schematic diagram of Bragg reflections from crystal planes of a material.

By varying the angle θ, the Bragg condition is satisfied by each characteristic crystal plane spacing of the material. When the angular position is plotted against the resulting diffracted peak intensities, a characteristic pattern of the sample is produced. Where a mixture of different phases is present, the diffraction pattern is formed by the addition of individual patterns. X-ray diffraction is therefore a non-destructive characterisation technique that provides information on the crystallographic structure of a material.

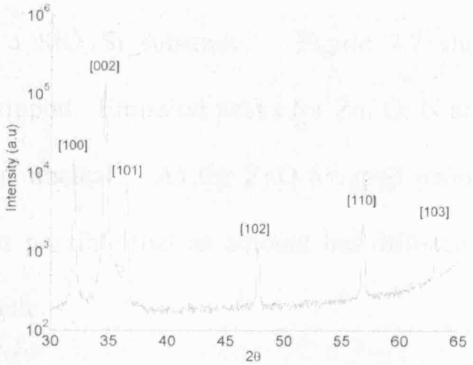

Figure 7.6. X-ray diffraction pattern of ZnO tetrapod nanocrystals (Newton *et al.* [1]).

Figure 7.6 shows the x-ray diffraction pattern obtained for dispersion of ZnO tetrapods on a Si substrate. The observed peaks indicate that the ZnO tetrapod nanocrystals have wurtzite structure. Moreover no peaks are observed that suggest the presence of impurities. The [002] peak is much more intense than the [100] and [101] indicating that the nanocrystals grow along the (0001) direction [3]. Similar results have been reported by Dai *et al.* and Chen *et al.* [4,5].

7.4 Energy Dispersive Spectroscopy

Energy dispersive spectroscopy (EDS) is a method for identifying and quantifying the elemental composition of material. The characteristic x-rays are produced when a material is bombarded with electrons from a source such as a scanning electron microscope (SEM). As each element has a unique electronic structure, the properties of the emitted x-rays can be used to determine the composition. Sample areas down to a few cubic micrometers can be analysed using this technique. ZnO tetrapods were mono-dispersed onto a SiO_2/Si substrate. Figure 7.7 shows the EDS spectrum obtained for a ZnO tetrapod. Emission peaks for Zn, O, N and Si are observed. The origin of the N peak is unclear. As the ZnO tetrapod nanocrystals are synthesised prominently in N_2 it is possible that an amount has diffused into the tetrapod along with the SiO_2/Si substrate.

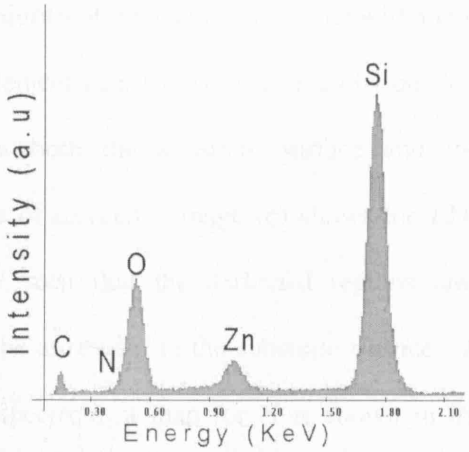

Figure 7.7. Energy dispersive X-ray spectrum of ZnO tetrapod nanocrystal on the surface of a SiO/Si substrate. Emission peaks for Zn, O, C, N and Si are observed.

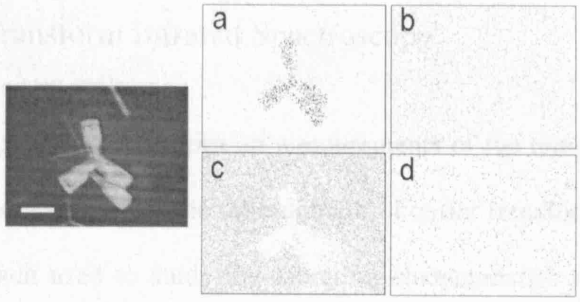

Figure 7.8. SEM image of a ZnO tetrapod nanocrystal (LHS). A 1 μm scale bar is shown. Four Energy dispersive spectroscopy maps for (a) Zn, (b) O, (c) Si and (d) N are shown on the RHS. The darker regions correspond to the presence of each element.

Figure 7.8 shows an SEM image of a ZnO tetrapod with EDS elemental mappings to the right. The darkened regions represent the presence of corresponding element. Image (a) shows the EDS map for Zn. By comparison with the SEM image, it is

clearly seen that the majority of the features coincide with the location of the tetrapod. Image (b) shows the element map for oxygen. No obvious localisation is visible and can be understood as both the substrate surface and the nanocrystal contain stoichiometric amounts of oxygen. Image (c) shows the EDS element map for Si. Once again it can be seen that the darkened regions are localised around the nanostructure and can be attributed to the substrate surface. As a small N peak was observed in the EDS spectrum, a map for N is shown in image (d). No obvious localisation of the darkened region can be seen. This suggests that an amount of N is present and distributed evenly across the map. This understood if the N is assumed to originate from the ambient.

7.5 Fourier Transform Infrared Spectroscopy

Fourier transform spectroscopy relies on measurements of the temporal coherence of electromagnetic radiation within the time-domain. Fourier transform infrared (FTIR) spectroscopy is often used to study the vibration characteristics of chemical bonds within a molecular species or material sample [6]. When infrared light interacts with a material chemical bonds are stretched, contracted and bent. Distinct chemical bonds tend to adsorb infrared radiation in a specific wave-number range largely independent of the structure of the rest of the material. A correlation between the wave-number position and a chemical structure can be used to identify a bonding configuration in a sample.

FTIR measurements were performed in reflection mode on ZnO tetrapods as grown on Si substrates. A bare Si substrate taken from the same wafer is used to subtract the

background spectrum. Figure 7.9 shows the FTIR spectrum in the range of 400 - 750 wave-numbers (cm^{-1}).

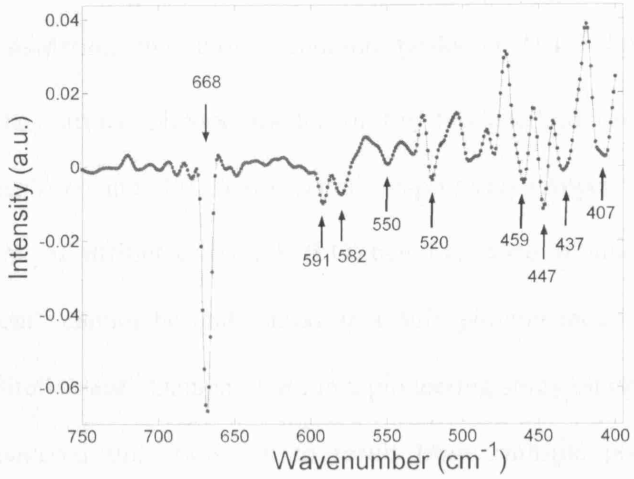

Figure 7.9. FTIR spectrum of ZnO tetrapod nanocrystals. Each label is shown in units of (cm^{-1}).

The absorption band centred at 407 cm^{-1} is attributed to the infrared active E_1 transverse optical (TO) phonon mode for ZnO (Appendix A). The absorption band centred at 447 cm^{-1} is split into three peaks at 459, 447 and 437 cm^{-1}. All three peaks can be attributed to the infrared and Raman active E_2 longitudinal optical (LO) phonon bending mode [7-9]. The observed broadening and splitting is due to the presence of impurity states from dopants, oxygen vacancies and zinc interstitials. Due to quantum confinement effects not all phonon modes observed are fundamental oscillations. Surface phonon modes can also be observed in the infrared spectrum. For a cylindrical structure the surface phonon frequency ω_s is given by [10]:

$$\omega_s^2 = \omega_\theta^2 \frac{\varepsilon_0^{\parallel} + \varepsilon_m}{\varepsilon_\infty^{\parallel} + \varepsilon_m} \tag{7.2}$$

where ω_θ is the fundamental phonon frequency and ε_m is the real part of the frequency dependent dielectric function . For wurtzite ZnO $\varepsilon_0^{\parallel} = 8.49$, $\varepsilon_\infty^{\parallel} = 3.72$ and $\varepsilon_m \simeq 2.36$. Considering the above equation peaks at 591, 550 and 520 cm^{-1} correspond to the surface phonon modes of the fundamental oscillations at 437 ($E_2(LO)$), 407 ($E_1(TO)$) and 380 ($A_1(TO)$) cm^{-1} respectively (Appendix A). The peak centred at 582 cm^{-1} is attributed to the $E_1(LO)$ bending mode in bulk ZnO. The peak centred at 668 cm^{-1} cannot be understood as a bulk phonon mode [11]. Its origin is therefore not entirely clear. Damen *et al.*, in a pioneering study on optical phonons in ZnO, have considered this transition to result from multiple phonon modes [12]. Similar results have been observed by Arguello *et al.* [13]. There however remains no consensus as to the exact nature of this peak.

7.6 Raman Spectroscopy

Raman scattering, like infrared spectroscopy, is an effective technique for observing phonons within a molecular species or material sample. An incident photon is absorbed forming an intermediate energy state. This energy state interacts with phonons and additional excitations either absorbing or emitting optical phonons. The incident photon is then scattered into a different energy state and emitted. This is therefore an inelastic scattering process. Crystals with inversion symmetry have optical phonons that are either infrared or Raman active. Crystals such as ZnO that lack inversion symmetry have optical phonons that can be both infrared and Raman active. Infrared active phonons modulate the electric dipole moment while Raman active phonons modulate the polarisability of the material. A detailed theoretical

study of Raman scattering has be provided by Cardona *et al.* [14]. ZnO tetrapods, mono-dispersed from methanol solution onto a SiO_2 substrate, were used for vibrational mode measurements. Individual ZnO tetrapods were excited by a 515 nm Ar ion laser focussed at the sample surface.

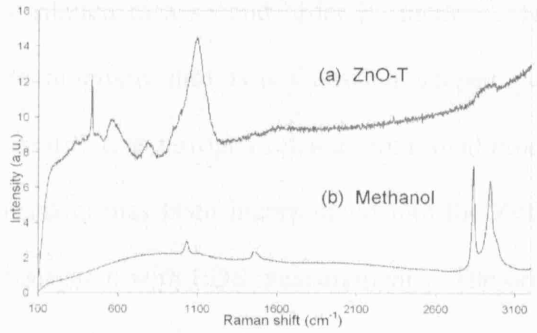

Figure 7.10. Raman spectra of individual ZnO tetrapod (ZnO-T) dispersed from methanol suspension (a) and that of methanol (b).

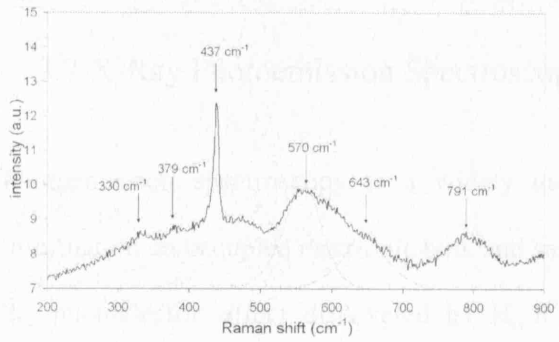

Figure 7.11. Raman spectrum of individual ZnO tetrapod nanocrystal. Data taken from figure 7.6 (a).

Figure 7.10 (a) and (b) shows the Raman spectra of an individual ZnO tetrapod (ZnO-T) and methanol respectively. Peaks characteristic of methanol and centred at 1029, 1450, 2836, 2944 cm^{-1} are visible in the ZnO-T spectrum where the 1029 cm^{-1} peak is

most intense. Adsorption of methanol at the tetrapod surface adequately explains the presence of corresponding peaks between the two spectra.

Figure 7.11 shows an expanded view of the same Raman spectrum as in figure 7.6 (a) at low wave-number. When considering the Wurtzite structure of ZnO-T, phonon modes E_2 (low and high frequency), A_1 (TO and LO) and E_1 (TO and LO) are expected. The high frequency E_2 mode is clearly visible at 437 cm^{-1} while the peak at 379 cm^{-1} can be attributed to the A_1 (TO) mode. The small peak at 330 cm^{-1} has been attributed to a second order E_2 mode [11]. The asymmetric peak at 570 cm^{-1} can be decomposed into two Gaussian shaped curves at 570 and 643 cm^{-1}, previously identified as nitrogen related vibrational modes [15-17]. This suggests that an amount of nitrogen has been incorporated into the ZnO tetrapods during the synthesis process, consistent with EDS measurements. The origin of the remaining peak centred at 791 cm^{-1} is however unclear.

7.7 X-Ray Photoemission Spectroscopy

Photoemission spectroscopy is a widely used experimental technique to obtain information on occupied electronic bulk and surface states. Its mechanism is based on the photoelectric effect discovered by H. R. Hertz. When a material surface is exposed to electromagnetic radiation above a certain threshold frequency, specific to the type of surface and material, the photons are absorbed at the surface. When the material relaxes from the excited state an electron is emitted with energy E_B proportional the absorbed photons. With large enough coupling of the photo-excited hole to the surrounding electrons in the material, additional excitations such as

phonons, plasmons and inter-band transitions can occur during the relaxation process. The emitted electron will receive only a portion of the relaxation energy E_R. Photoelectrons of this kind occur at 'satellite' peaks in the photoemission spectrum.

When a monochromatic beam of soft x-rays (Al-K_α ~1486 eV) is focussed onto a sample the x-rays penetrate ~1 μm into the sample producing photoelectrons throughout the penetration region. The energies of the emitted electrons are characteristic of their original electronic states and provide information on the bonding state, configuration interactions and polarization effects of atoms within the vicinity. The kinetic energy of the photoelectrons can be converted into binding energy values which are independent of the x-ray source. This can be achieved by considering the Einstein relation:

$$E_k = h\nu - E_B \tag{7.3}$$

The experimentally obtained binding energy values are characteristic of the material and can be used to identify the chemical nature, electronic state and element species localized within the bulk of the sample. When X-Ray Photoemission Spectroscopy (XPS) is combined with Ar-ion milling, bulk states are more easily studied. As the mean free path of electrons emitted is typically of the order of a few nanometres, the majority of electrons are excited near to the surface. XPS is therefore used for chemical analysis of surface states and adsorbents at the surface.

X-Ray Photoemission Spectroscopy measurements were performed on ZnO tetrapod nanocrystals grown in both Ar and N_2 atmospheres with an O_2 partial pressure. Comparable quantities of tetrapod nanocrystals from each growth process were spin

coated from methanol suspension onto separate Si (111) substrates for use in XPS measurements. Figures 7.12 and 7.13 show the XPS spectra for each type of nanocrystal:

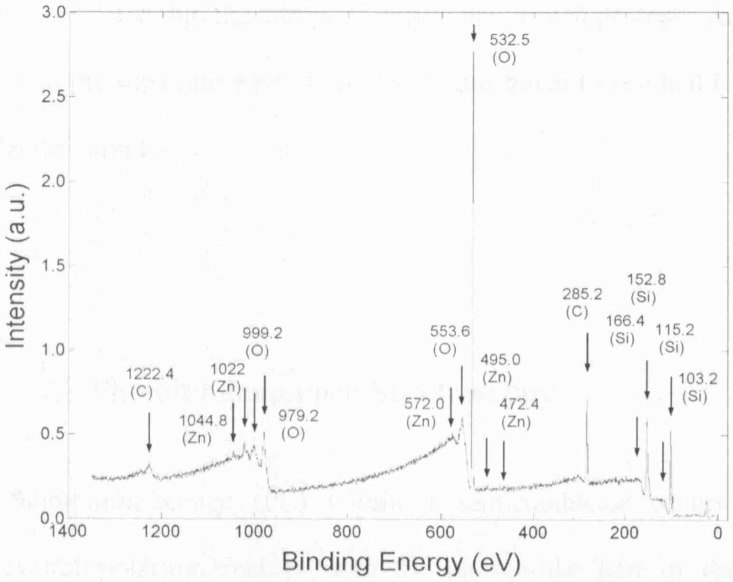

Figure 7.12. XPS spectrum of ZnO tetrapod nanocrystals grown in Ar and O_2 atmosphere.

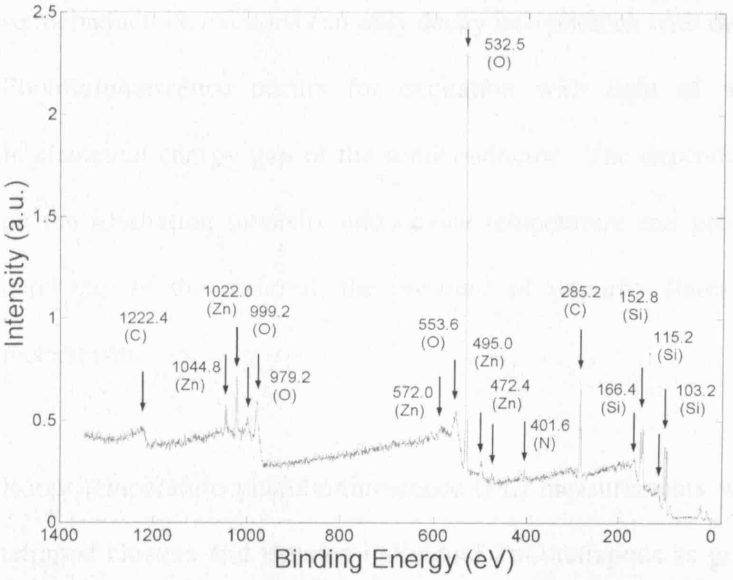

Figure 7.13. XPS spectrum of ZnO tetrapod nanocrystals grown in N_2 and O_2 atmosphere.

XPS and Auger peaks due Zn and O are clearly visible throughout the spectrum and are consistent for ZnO tetrapods grown in Ar and N_2. ZnO tetrapods grown in N_2 however show an additional peak at 401.6 eV that is not present in the Ar grown tetrapod spectrum. This peak is attributed to N and suggests that an amount of N is incorporated into the tetrapods during the growth process. Additional peaks for Si are from the substrate while C peaks are attributed to residual C within the chamber and in the samples.

7.8 Photoluminescence Spectroscopy

Photoluminescence (PL) within a semiconductor occurs when a photo-excited exciton-polariton relaxes onto the photon-like part of the lower polariton band, recombines and ultimately leaves the material as a photon. This process is often accompanied by other fundamental excitations. For example, in indirect semiconductors, excitons can only decay into photons with the assistance of a phonon. Photoluminescence occurs for excitation with light of wavelengths around the fundamental energy gap of the semiconductor. The dependence of the PL spectrum on the irradiation intensity and device temperature can provide information on the band gap of the material, the presence of impurity states and the recombination mechanism.

Room temperature photoluminescence (PL) measurements were carried out on ZnO tetrapod clusters and isolated individual ZnO tetrapods as grown. Light from a 325 nm He-Cd continuous-wave laser was used as an excitation source and was focussed

onto the sample surface. Figure 7.14 shows the PL spectrum for an isolated individual ZnO-T and a cluster of ZnO-T nanocrystals. Both graphs show a broad peak centred around 2.3 eV and a more narrow peak at 3.2 eV. Randomly orientated tetrapod clusters exhibit emission dominated by the broad peak at 2.3 eV while the spectrum of the isolated ZnO-T is dominated by the peak centred at 3.2 eV. ZnO tetrapod nanocrystals orientate spontaneously with one arm normal to the substrate. As the single optical axis is aligned along the arm (see chapter 6), band edge emission is expected to be most intense in this direction. Enhancement of the UV peak for an isolated ZnO tetrapod is therefore understood, as the UV emission points toward the detector normal to the substrate.

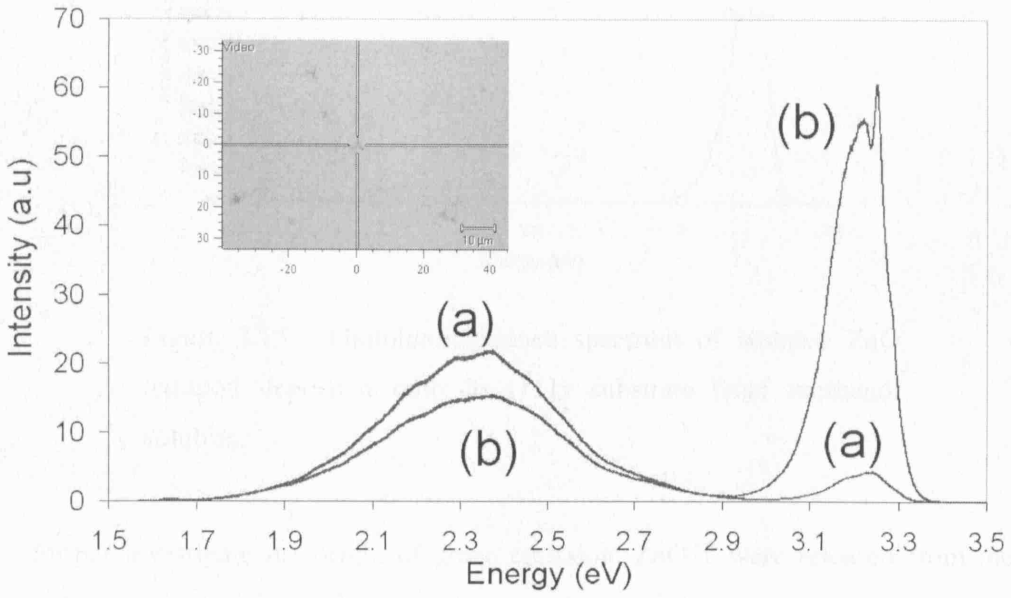

Figure 7.14. Room temperature photoluminescence of ZnO tetrapod cluster (a) and isolated (b) ZnO tetrapod. Inset shows an optical image of a ZnO tetrapod at the centre of the crosshair.

The peak centred at 3.2 eV is close in energy to the band gap of ZnO and can be attributed to free exciton recombination [1,18,19]. The broad peak centred at 2.3 eV can be attributed to defect emission due to O vacancies and Zn interstitials [20,21]. The relative intensity of band edge and defect related emission was found to depend on the size of the nanostructure [22,23]. The types of defect states responsible for green emission ($h\nu \sim 2.3\,\text{eV}$) have not been conclusively identified. Djurišic *et al.* showed that coating ZnO nanostructures with a surfactant suppressed green emission [18]. There is therefore convincing evidence that it is surface related.

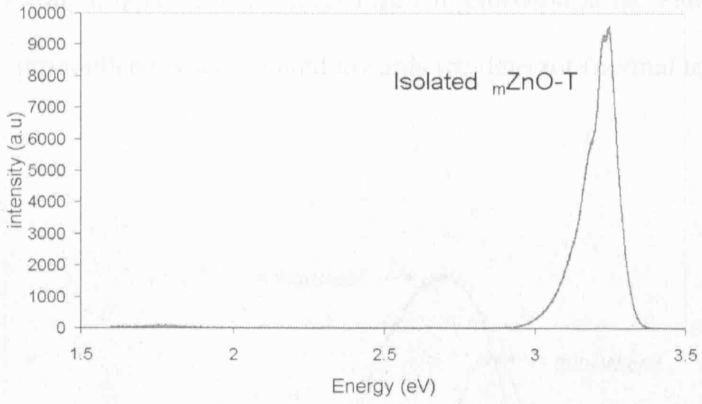

Figure 7.15. Photoluminescence spectrum of isolated ZnO tetrapod deposited onto Si (111) substrate from methanol solution.

To further investigate the origin of green emission, ZnO-T were released from the substrate by sonication in methanol and subsequently dispersed onto a clean Si <111> substrate. Figure 7.15 shows PL data obtained from ZnO-T clusters injected onto a Si substrate. It is evident that the broad green emission peak measured on as grown ZnO-T is completely suppressed. Moreover, when these samples were placed in a vacuum and PL measurements repeated the green emission peak did not return. This

effect may be attributed to hydrogen electron passivation of radiative recombination at the nanocrystal surface [24]. We therefore conclude that the observed green emission is directly related to the surface properties of these nanocrystals.

When the excitation source is focused on an individual ZnO-T spontaneously orientated on the substrate surface, the emission at 3.2 eV is greatly increased over that of the emission at 2.3 eV. This amplification can be attributed to resonant cavity effects coupled with wave-guiding occurring along the vertical arm of each ZnO-T which aligns with the crystal optical axis. This also implies that some reflection occurs at the tetrapod core. Such effects result in emission at the ends of each arm which is more pronounced when pointed towards the detector (normal to the surface).

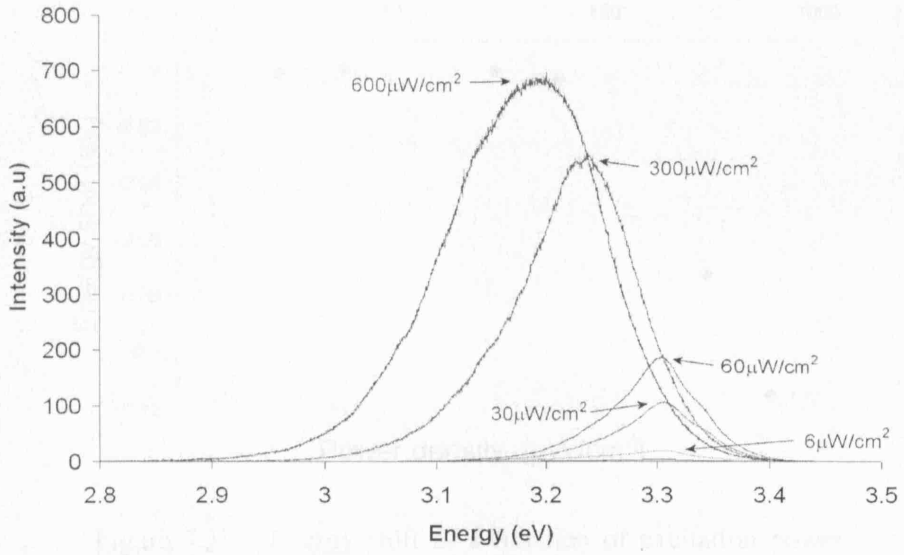

Figure 7.16. Photoluminescence spectra of a single ZnO tetrapod with varying excitation power.

Figure 7.16 shows PL data for an isolated ZnO-T in which the power of the He-Cd (325 nm) laser excitation source is steadily increased from 3 $\mu W/cm^2$ to 600 $\mu W/cm^2$. At lower excitation powers, peaks centred on 3.3 eV are present and can be attributed to radiative recombination of electron-hole pairs near the band edge. As the power is further increased excitons are no longer weakly coupled and a collective electron hole plasma (EHP) phase begins to form [25]. This effect is evident in the remaining emission peaks which have their maxima red shifted as far as 3.19 eV. Heating effects within the ZnO-T are also likely to cause a red shift of resonant modes within the structure due to an increased refractive index. This effect is more pronounced in low dimensional nanostructures where confinement effects further limit the number of available states near the band edge.

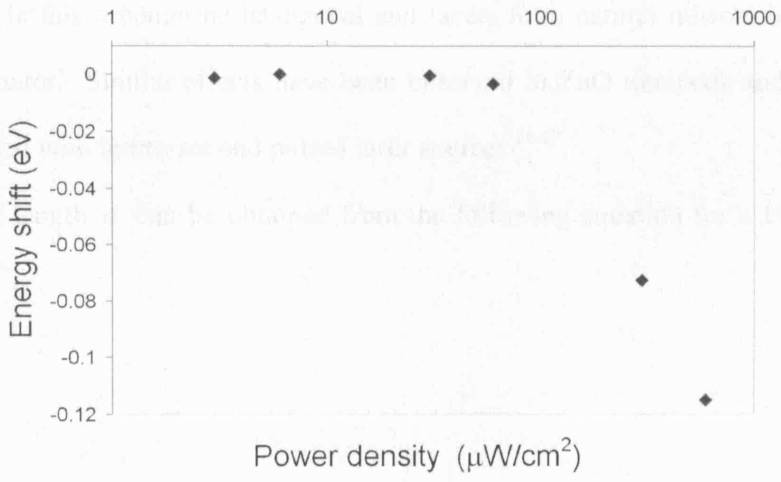

Figure 7.17. Energy shift as a function of excitation power. Data points are taken from the maximum of each curve in figure 7.16.

Figure 7.17 depicts the energy shift of the PL peak as a function of the excitation power. As the excitation power density is increased above 60 $\mu W/cm^2$, the band gap begins to reduce rapidly, indicating a transition into the electron-hole plasma phase.

Photoluminescence measurements performed on relatively large ZnO tetrapod nanocrystals often revealed the presence of evenly spaced peaks superimposed on band edge emission peak. Figure 7.18 shows the photoluminescence spectrum of a ZnO-T with arm lengths of 10 μm. A series of peaks are clearly seen on the lower energy side of the band edge emission. These modes are attributed to constructive interference of the emission. The longitudinal component of the emission is understood to form resonant cavity modes along the length of each arm of the tetrapod structure. In this scheme the hexagonal end facets form natural mirrors of a Fabry-Perot resonator. Similar effects have been observed in ZnO tetrapods and nanorods when excited with femto-second pulsed laser sources [26,27].

The cavity length d can be obtained from the following equation for a Fabry-Perot resonator [25]:

$$\Delta\nu = \frac{c}{2dn} \tag{7.4}$$

where $\Delta\nu$ is the frequency of the mode spacing, c is the speed of light in a vacuum and n is the refractive index. A mode spacing of 1.58 nm is obtained from figure 7.18 and corresponds to a cavity length of 21 μm. As this is approximately twice the length of each arm shown in the figure, it seems feasible that cavity mode resonance spans across two or more arms of the tetrapod.

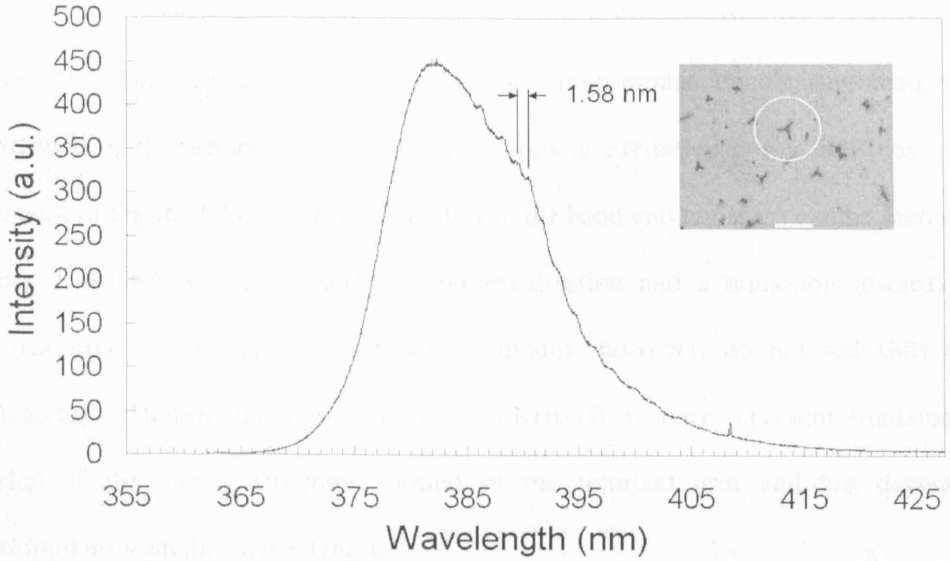

Figure 7.18. Photoluminescence spectrum of single ZnO tetrapod nanocrystal. Resonant cavity modes are superimposed on the band edge emission and have a mode spacing of 1.58 nm. Inset shows the ZnO tetrapod used in the measurements. A 20 μm scale bar is shown.

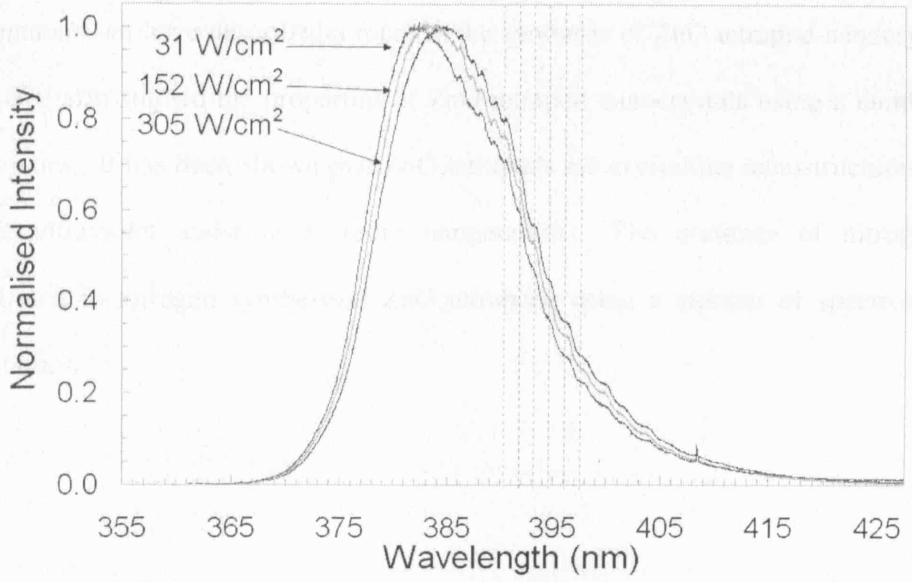

Figure 7.19. Photoluminescence spectra of ZnO tetrapod nanocrystal. The band edge emission is seen to red shift with increasing excitation intensity while the resonant cavity modes remain largely unperturbed. The dotted lines are shown as a guide.

To confirm that the observed peaks are due to cavity modes, PL measurements were performed on the tetrapod nanocrystal at a series of excitation power densities. This is shown in Figure 7.19. A clear Mott shift in the band end emission can be seen as in figure 7.18 and is due to band gap renormalisation and a transition towards the electron-hole plasma phase. The cavity modes, however, do not red shift with increasing excitation intensity. This is understood as they represent fundamental modes of the cavity structure formed in the tetrapod arm and are dependent predominantly on the cavity length.

Summary

In summary we have described a route to the synthesis of ZnO tetrapod nanocrystals. We have also studied the properties of ZnO tetrapod nanocrystals using a number of techniques. It has been shown that ZnO tetrapods are crystalline nanostructures with stable ultraviolet emission at room temperature. The presence of nitrogen is confirmed in nitrogen synthesised ZnO tetrapods using a number of spectroscopic techniques.

Reference List

[1] M. C. Newton, S. Firth, T. Matsuura, and P. A. Warburton, J. Phys. Conf. Ser. **26**, 251 (2006)

[2] N. W. Ashcroft and N. D. Mermin, *Solid State Physics*, (Brooks Cole, 1976).

[3] F. Z. Wang, Z. Z. Ye, D. W. Ma, L. P. Zhu, and F. Zhuge, Mater. Lett. **59**, 560 (2005)

[4] Y. Dai, Y. Zhang, Q. K. Li, and C. W. Nan, Chem. Phys. Lett. **358**, 83 (2002)

[5] Z. Chen, Z. W. Shan, M. S. Cao, L. Lu, and S. X. Mao, Nanotechnology **15**, 365 (2004)

[6] B. C. Smith, *Fundamentals of Fourier Transform Infrared Spectroscopy*, (CRC, 1995).

[7] M. Tzolov, N. Tzenov, D. mova-Malinovska, M. Kalitzova, C. Pizzuto, G. Vitali, G. Zollo, and I. Ivanov, Thin Solid Films **379**, 28 (2000)

[8] E. M. Bachari, G. Baud, S. Ben Amor, and M. Jacquet, Thin Solid Films **348**, 165 (1999)

[9] M. Zerdali, S. Hamzaoui, F. H. Teherani, and D. Rogers, Mater. Lett. **60**, 504 (2006)

[10] K. Yamamoto, C. D. Tran, H. Shimizu, and K. Abe, J. Phys. Soc. Jpn. **42**, 587 (1977)

[11] J. M. Calleja and M. Cardona, Phys. Rev. B **16**, 3753 (1977)

[12] T. C. Damen, S. P. S. Porto, and B. Tell, Phys. Rev. **142**, 570 (1966)

[13] C. A. Arguello, D. L. Rousseau, and S. P. S. Porto, Phys. Rev. **181**, 1351 (1969)

[14] M. Cardona, *et al.*, *Light Scattering in Solids VIII: Fullerenes, Semiconductor Surfaces, Coherent Phonons*, (Springer, 2000).

[15] U. Haboeck, A. Hoffmann, C. Thomsen, A. Zeuner, and B. K. Meyer, Phys. Status Solidi B **242**, R21-R23 (2005)

[16] A. Kaschner, U. Haboeck, M. Strassburg, M. Strassburg, G. Kaczmarczyk, A. Hoffmann, C. Thomsen, A. Zeuner, H. R. Alves, D. M. Hofmann, and B. K. Meyer, Appl. Phys. Lett. **80**, 1909 (2002)

[17] Y. G. Wang, S. P. Lau, X. H. Zhang, H. W. Lee, H. H. Hng, and B. K. Tay, J. Cryst. Growth **252**, 265 (2003)

[18] A. B. Djurisic, W. C. H. Choy, V. A. L. Roy, Y. H. Leung, C. Y. Kwong, K. W. Cheah, T. K. Gundu Rao, W. K. Chan, H. Fei Lui, and C. Surya, Adv. Func. Mater. **14**, 856 (2004)

[19] W. D. Yu, X. M. Li, and X. D. Gao, Chem. Phys. Lett. **390**, 296 (2004)

[20] B. X. Lin, Z. X. Fu, and Y. B. Jia, Appl. Phys. Lett. **79**, 943 (2001)

[21] X. Q. Meng, D. Z. Shen, J. Y. Zhang, D. X. Zhao, Y. M. Lu, L. Dong, Z. Z. Zhang, Y. C. Liu, and X. W. Fan, Solid State Commun. **135**, 179 (2005)

[22] M. H. Huang, Y. Wu, H. Feick, TranN., E. Weber, and P. Yang, Adv. Mater. **13**, 113 (2001)

[23] I. Shalish, H. Temkin, and V. Narayanamurti, Phys. Rev. B **69**, 245401 (2004)

[24] N. Ohashi, T. Ishigaki, N. Okada, H. Taguchi, I. Sakaguchi, S. Hishita, T. Sekiguchi, and H. Haneda, J. Appl. Phys. **93**, 6386 (2003)

[25] C. Klingshirn, *Semiconductor Optics*, (Springer, Berlin, 2005).

[26] J. M. Szarko, J. K. Song, C. W. Blackledge, I. Swart, S. R. Leone, S. H. Li, and Y. P. Zhao, Chem. Phys. Lett. **404**, 171 (2005)

[27] M. H. Huang, S. Mao, H. Feick, H. Q. Yan, Y. Y. Wu, H. Kind, E. Weber, R. Russo, and P. D. Yang, Science **292**, 1897 (2001)

8. ZnO Tetrapod Schottky Diodes

8.1 Introduction

The use of zinc oxide in ultraviolet optoelectronic devices has attracted considerable interest mainly due to its large exciton binding energy of 60 meV and high thermal and chemical stability [1-4]. Photodetectors based on the Schottky junction are desirable due to their ability to operate at high switching speeds. Progress in their development is often limited by the difficulty in reproducibly fabricating high quality rectifying contacts to ZnO films [5-8]. There are however a number of recent studies addressing the interfacial properties of ZnO [6,9,10].

More recently reports have been made on Schottky diodes based on ZnO rods that show photoresponse when subject to UV excitation [11,12]. In the following a route to fabricating an ultraviolet sensitive diode based on a single ZnO tetrapod nanocrystal is described. Focussed ion-beam (FIB) assisted metal deposition is a powerful technique for creating device prototypes and employed here to fabricate ZnO tetrapod Schottky diodes. The response of the device is measured with above and below band gap continuous wave laser illumination and is shown to vary with the illumination intensity. A model for the response of the device is developed and shown to adequately explain the response of the device to above band gap illumination.

8.2 Introduction to Focussed Ion-Beam (FIB) Metal Deposition

The focused ion beam (FIB) system uses a beam of Ga ions to raster over a surface of a sample in much the same way as the electron beam in a scanning electron microscope (SEM). The secondary electrons generated by the incident electrons or ions on a sample are collected and used to form an image of the surface of the sample. The focused ion beam can also be used for the milling of small features into a sample at localized sites. This allows cross-sectional images of the structure or modifications in the structure to be made. FIB milling is often used for transmission electron microscopy (TEM) sample preparation [13]. In this process a cross section on the sample is thinned down to form an electron transparent lamella. This can then be removed and transferred to a TEM sample stage for further imaging. FIB imaging and milling techniques have the disadvantage that they are inherently destructive. Samples imaged using FIB will to some extent have Ga and other local impurities implanted into the surface. With increased irradiation intensity, the FIB will begin to mill into the sample possibly destroying features. For this reason FIB milling is often combined with SEM imaging. Figure 8.1 shows a schematic diagram of the SEM-FIB 'Cross Beam' system used in this work.

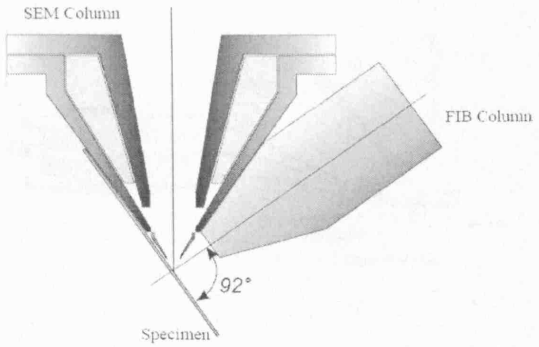

Figure 8.1. Geometrical layout of the LEO 1540 Cross Beam system. The electron and the ion beam coincide at a crossover point 5 mm below the objective lens of the SEM. The geometrical properties of the two columns allow ion milling on large samples (wafers) at angles up to 92° (with respect to the ion beam). Images courtesy of Carl Zeiss NTS.

The focused ion beam can also be used as a direct writing tool. Metals such as Pt and W can be deposited by metallo-organic chemical vapour deposition of dimethyl-methyl-cyclopentadienyl-Pt and hexacarbonyl-W gas phase precursors respectively. In this process, the precursor is injected into the vicinity of the focal point of the FIB near to the surface of the sample. At a sufficient beam current, the precursor is broken down resulting in metal deposition at the surface. An amount of hydrocarbons from the precursor are also released into the chamber during the deposition process. The deposited metal therefore contains an amount of Ga from the ion beam and C from the precursor and chamber. If the current from the FIB is too large the beam will begin to mill into the sample. If it is too small there will be insufficient energy to break down the metallo-organic precursor. It is therefore important to obtain the correct conditions for metal deposition.

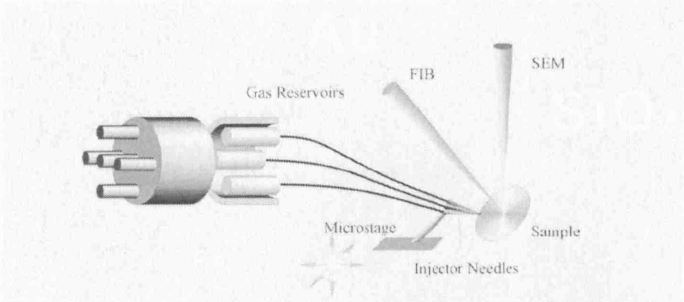

Figure 8.2. Schematic of the gas injection system (GIS). Five gas reservoirs provide up to five different gases. The gases are applied to the sample by a set of five injector needles that are positioned by a computer controlled micro stage. Images courtesy of Carl Zeiss NTS.

Ga ion beam deposited Pt and W was characterised by measuring the resistivity of the deposited material. Microscopic Pt and W contacts were made between pre-patterned macroscopic Au contacts on SiO_2/Si substrates. Figure 8.3 shows an SEM image of a typical Pt contact made between two Au contacts.

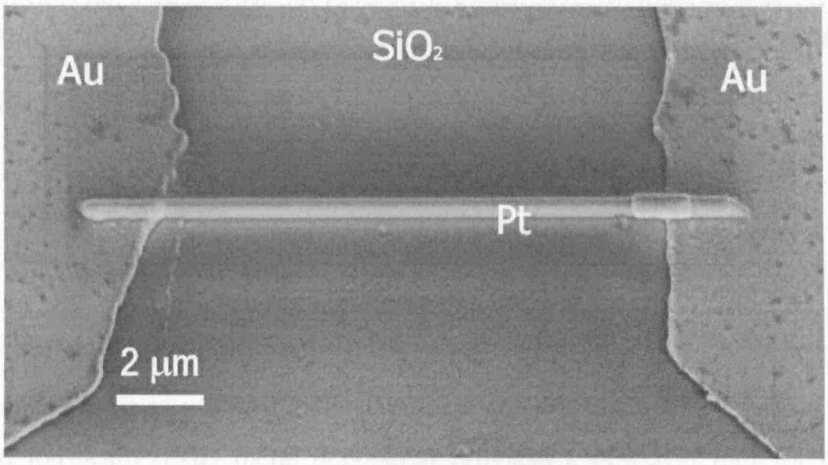

Figure 8.3. SEM image of Ga ion-beam deposited Pt between two Au contacts.

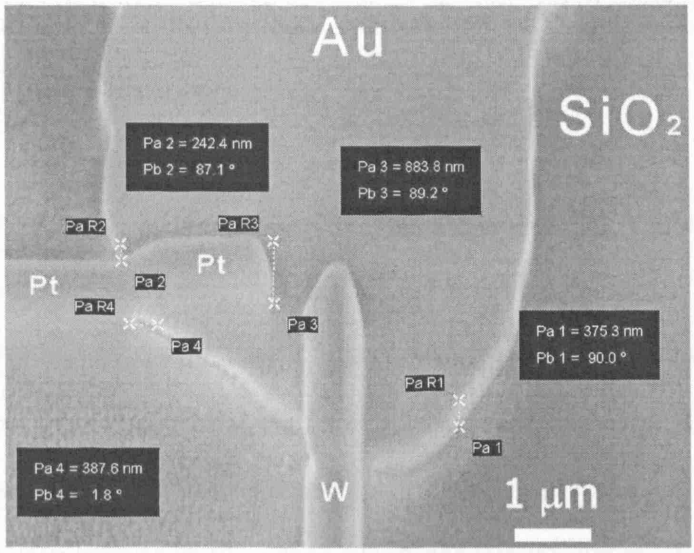

Figure 8.4. Dimensions of deposited Pt or W can be measured in situ allowing the resistivity to be estimated.

The height of the deposited Pt is estimated at 500 nm. By considering the geometry of the deposited Pt wire the resistivity can be estimated at 2×10^{-3} Ohm cm. By similar means, the resistivity of W was estimated at 3×10^{-4} Ohm cm. The dimensions of each structure that is deposited can be measured in situ as shown above. From these values it can be seen that W is an order of magnitude more conductive than Pt.

8.3 Fabrication of ZnO Tetrapod Schottky Diode

Focussed ion-beam (FIB) metal deposition provides a powerful tool for prototype device fabrication and making electrical contact to nanoscale structures. In the

following a method of fabricating metal contacts both of Pt and W to a single ZnO tetrapod nanocrystal is described.

ZnO tetrapod (ZnO-T) nanocrystals were synthesised using a chemical vapour transport technique as previously reported[14-18] and described in chapter 7. A summary is given here for brevity. A mixture of zinc carbonate powder and graphite powder is placed in a crucible at the central region of a quartz tube furnace. A bare Si [001] substrate is mounted in the downstream region of the quartz tube. Nitrogen carrier gas with an oxygen content of 3% is then introduced into the quartz tube at a flow rate of 500 sccm while the temperature of the furnace is brought up to 900°C. After a 15 minute reaction period a thin white layer of material is visible on the surface of the substrate.

ZnO tetrapod clusters were then released from the substrate by sonication in methanol to form a suspension. This solution was subsequently spun onto an oxidised Si substrate pre-patterned with Au electrodes. ZnO tetrapod nanocrystals then appear randomly placed across the surface of the substrate. At certain sites on the substrate the Au electrodes are in close proximity allowing electrical contact to easily be made between them. Figure 8.6 shows an example of this.

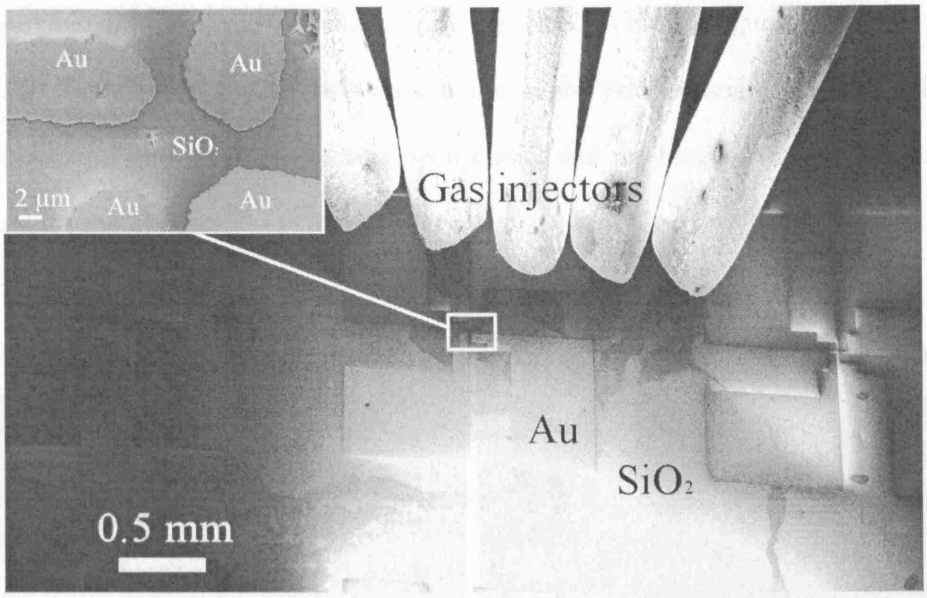

Figure 8.5. SEM image of substrate pre-patterned with Au electrodes. Five gas injector needles are also visible. The inset shows the location where four macroscopic Au pads and a single ZnO tetrapod are in close proximity.

Due to their four fold symmetric structure, ZnO tetrapods spontaneously orientate with three arms on the substrate surface and one pointing vertically away from the substrate. This allows electrical contact to be made to the three arms on the surface. As FIB deposition of metals is a serial process, the time taken to deposit a metal wire is directly proportional to the size of that wire. It is therefore desirable to have tetrapods land in the close proximity region for Au contacts (Figure 8.5 inset) so that metal contacts need not be excessively long.

Electrical contacts were made to a single ZnO tetrapod using FIB deposited Pt and W. Figure 8.6 shows the various stages in the device fabrication. Some hazing around each contact is visible and occurs as some of the metal is also deposited within the immediate vicinity of the focal point of the FIB. To ensure that this would not affect

measurements of the ZnO-T contacts were deposited in the configuration required for making contact to a ZnO-T but without the nanocrystal present. Current voltage measurements showed that this was open circuit and the haze of material deposited around the metal contact was non-conductive.

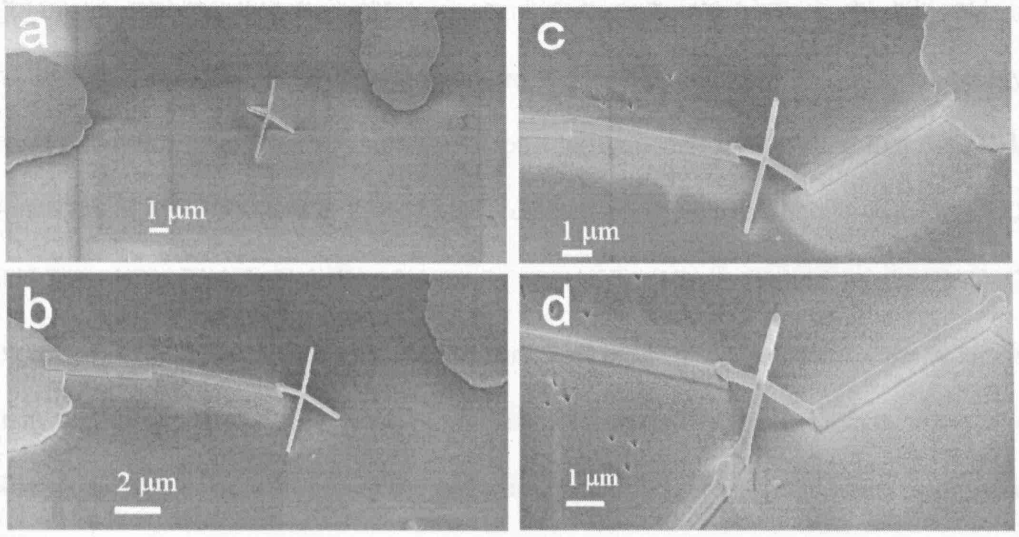

Figure 8.6. SEM images of ZnO tetrapod at various stages during metal deposition.

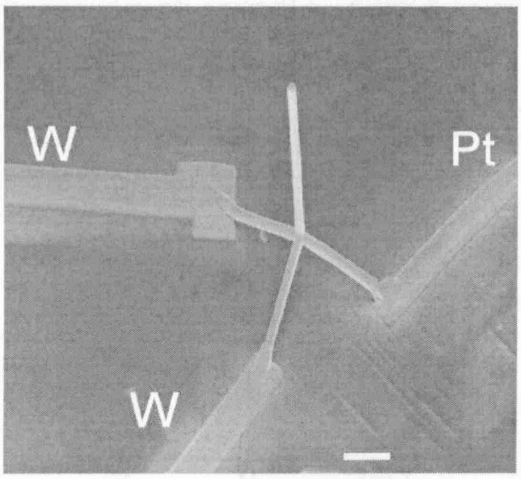

Figure 8.7. SEM image of ZnO tetrapod Schottky diode.

Both W and Pt are deposited using a 50 pA FIB ion current and an accelerating voltage of 30K V. It has generally been found that contacts made to a ZnO-T nanocrystal that are well defined more frequently produce device like characteristics. Figure 8.7 shows an SEM image of a ZnO tetrapod nanocrystal with two W and one Pt contact made to each arm of the structure on the substrate surface. In doing this a metal-semiconductor-metal device structure is formed. Figure 8.8 shows the energy band diagram of the Pt-ZnO interface. Considering equation (4.6) and that the work functions of W (4.55) and Pt (5.65), the predicted energy barrier height at the Pt-ZnO interface is $\phi_{Bn} = 1.3\,\text{eV}$. By the same means the barrier height at the W-ZnO interface is predicted as 0.2 eV. As the barrier at the Pt-ZnO interface is much larger than that at the W-ZnO interface, some rectification is expected to occur when this diode structure is biased. Given the non-zero barrier height at W-ZnO interface, some leakage in the reverse bias current-voltage characteristics is expected even for ideal contacts. In the following section the electronic properties of this device structure are explored.

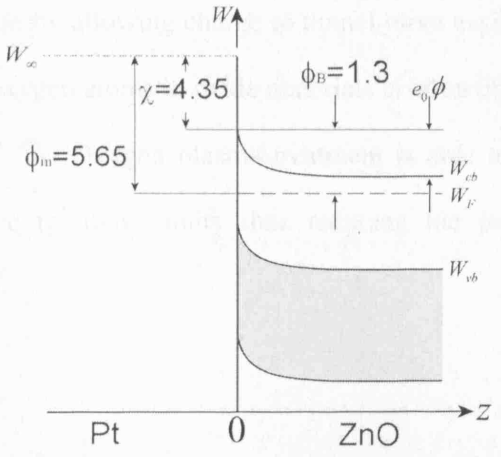

Figure 8.8. Energy band diagram of Pt-ZnO interface. All units in eV.

8.4 Electronic Properties of ZnO Tetrapod Schottky Diodes

Ex-situ dark current-voltage measurements were performed on a single ZnO tetrapod Schottky diode. Pt contacts made to the arm of a ZnO-T generally exhibit ohmic behaviour. A number of studies have shown that as-grown ZnO films contain defects such as O vacancies and Zn interstitials (see chapter 4). Moreover it has been shown that O atoms from the surface of ZnO are removed when placed in a vacuum [6]. This causes surface conductive channels which effectively short circuit the device. These effects can be avoided by pre-treatment with O plasma [8]. Samples were therefore prepared with and without O plasma pre-treatment. It was found that the treatment of the deposited ZnO tetrapod in oxygen plasma for 60 minutes at room temperature prior to the deposition of metal electrodes consistently formed a Schottky contact at the Pt-ZnO interface (Figure 8.9). Here the plasma treatment reduces the conductance of the Pt-ZnO junction by around three orders of magnitude and causes rectification. It is known that conductive channels exist due to oxygen vacancies and Zn interstitials at the semiconductor surface when ZnO films are placed *in vacuo* [6]. This is known to hinder barrier formation by allowing charge to tunnel more easily across the interface. A high diffusivity of oxygen atoms in oxide materials is often observed and occurs due to oxygen vacancies [19,20]. Oxygen plasma treatment is able to increase the ratio of O:Zn near the surface to above unity thus reducing the presence of conductive channels [8].

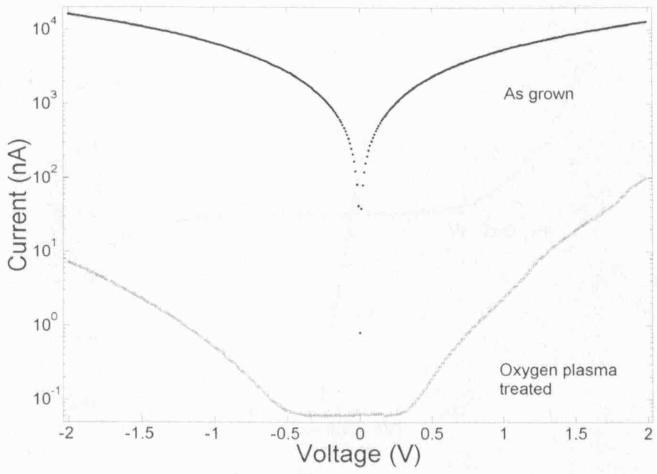

Figure 8.9. Log plot of the current-voltage characteristics of ZnO-T Schottky diodes fabricated using as-grown ZnO-T and ZnO-T treated for 60 minute in oxygen plasma at room temperature.

Figure 8.10 shows the two-terminal dark I-V measurements made between each pair of contacts at room temperature. The W-ZnO-W I-V curve shows ohmic properties while the Pt-ZnO-W curve exhibits non-linearity and rectification. The additional Pt-ZnO-W curve closely matches that of the latter and is omitted for clarity. We conclude therefore that W-ZnO contacts are ohmic while Pt-ZnO contacts are rectifying. The depletion of majority carriers results in an upward band bending of the energy bands at the interface and a positive space-charge region in the ZnO tetrapod.

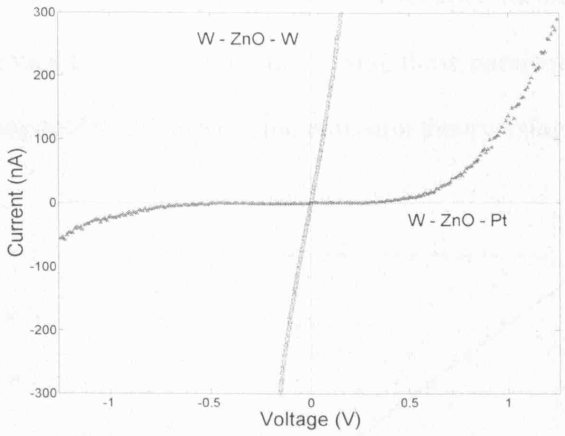

Figure 8.10. Room temperature dark I-V curves of W–ZnO–W and W–ZnO–Pt junctions.

In the absence of interfacial surface states the forward bias dark I-V data at saturation is fitted to the following equation that describes the thermionic emission of charge over the barrier at the Pt-ZnO interface:

$$J_{fb} = J_s \exp\left(\frac{e_0 V}{nkT}\right) \tag{8.1}$$

$$J_s = A^* T^2 \exp\left(-\frac{e_0 \phi_B}{kT}\right) \tag{8.2}$$

Here J_{fb} is current density in forward bias, $A^* = 4\, e_0 m^* k_B^2 / h^3$ is the effective Richardson constant, T the absolute temperature, ϕ_B the effective barrier height, n the ideality factor [21] and m^* the effective electron mass. Equation (8.1) is an approximation to that of equation (4.54) valid when $e_0 V / k_B T \gg 1$. It allows the barrier height and ideality factor to be more easily calculated. By taking $m^* = 0.29\, m_0$, where m_0 is the electron rest mass, the fit to the data shown in Fig 8.11 yields a Pt-

ZnO Schottky barrier height of 0.43 eV and an ideality factor of 11. In this the contact area is assumed to be 500x500 nm^2. Using these parameters, the Pt-ZnO-W I-V curve can be compared to the thermionic emission theory using equation (4.54).

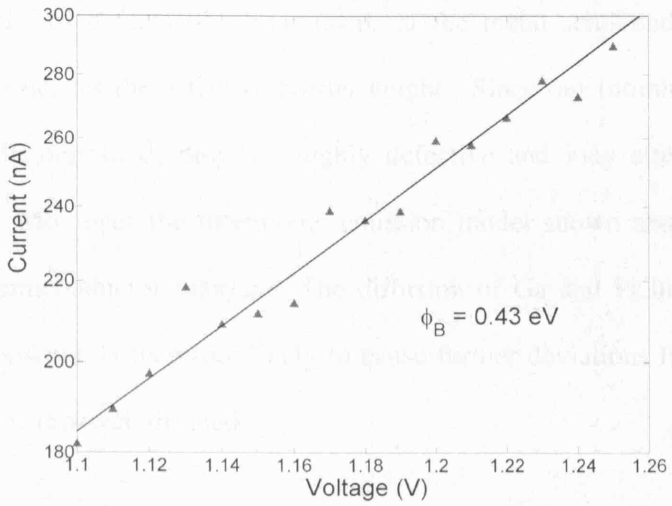

Figure 8.11. Forward bias dark IV curve at saturation for the Pt-ZnO-W junction, with the current shown on a logarithmic axis. The data points are taken from figure 8.10.

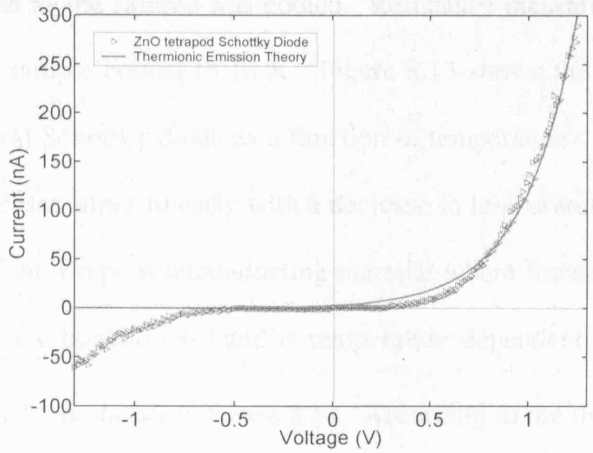

Figure 8.12. Comparison of ZnO tetrapod Schottky diode I-V curve with prediction of the thermionic emission theory. The barrier height and ideality factor are used as fitting parameters.

The obtained barrier height is in good agreement with measurements performed by Ip *et al.* on Pt contacts to ZnO thin films [22]. It is however smaller than the theoretical prediction and some previous reports made on Pt contacts to ZnO [7]. It is well known that the presence of defects or contaminants at the metal semiconductor interface significantly influences the effective barrier height. Since our (nominally) platinum contacts are FIB-deposited, they are highly defective and may alter the Schottky barrier height. Moreover the thermionic emission model shown above assumes an abrupt metal-semiconductor interface. The diffusion of Ga and Pt into the tetrapod arm during deposition is therefore likely to cause further deviations from this model as the interface is less well defined.

Measurements of the I-V characteristics were also performed at low temperatures down to 18 K. A single ZnO tetrapod diode was attached to a probe station and lowered into liquid He. The device was held at a fixed current in forward bias and the resistance measured as the sample was cooled. Resistance measurements were taken at intervals as the sample cooled to 18 K. Figure 8.13 shows the resistance R of a typical ZnO tetrapod Schottky diode as a function of temperature. It can be seen that the resistance increases super-linearly with a decrease in temperature. Such behaviour is characteristic of an n-type semiconducting material where the density of thermally excited carriers in the conduction band is temperature dependent. A plot of ln(R) against $(\ln(T^2)+1/T)$ is shown in figure 8.14. According to the thermionic emission theory of equation (4.54) this curve will appear as a straight line. This was found to be the case and therefore confirms that the model of thermionic emission adequately explains the observed I-V characteristics within the given temperature range.

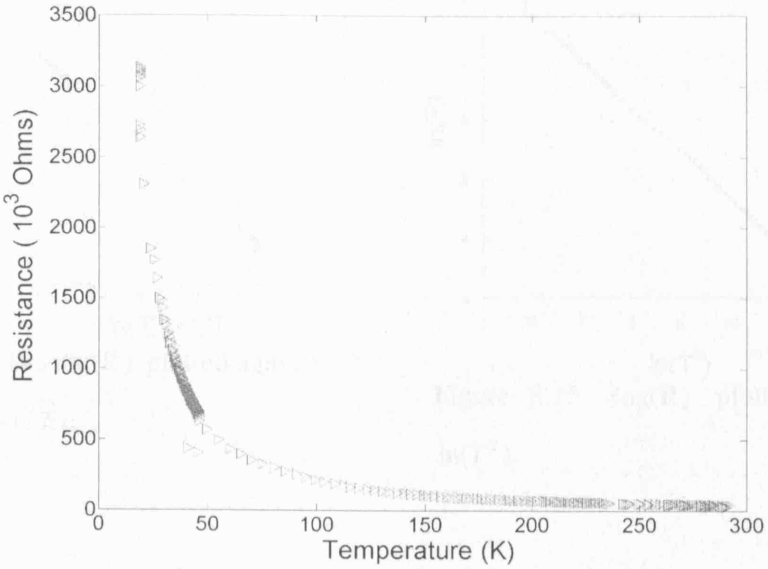

Figure 8.13. Temperature dependence of the resistance R of a ZnO tetrapod Schottky diode held at fixed current in forward bias.

Plots made of $\log(R)$ separately against $(\ln(T^2)+1/T)$ in figure 8.14 and $\ln(T^2)$ in figure 8.15 revealed that the $(1/T)$ dependence can be neglected as its influence on the linearity of the curve in figure 8.14 is minimal. The gradient of the curve in figure 8.15 is estimated as -0.70. This is reasonably close to -1 as deduced from the relationship in equation (4.54).

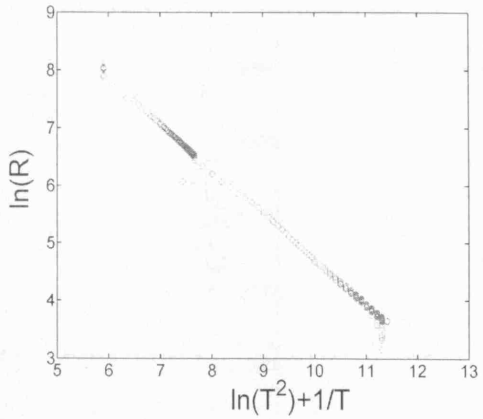

Figure 8.14. log(R) plotted against $(\ln(T^2)+1/T)$.

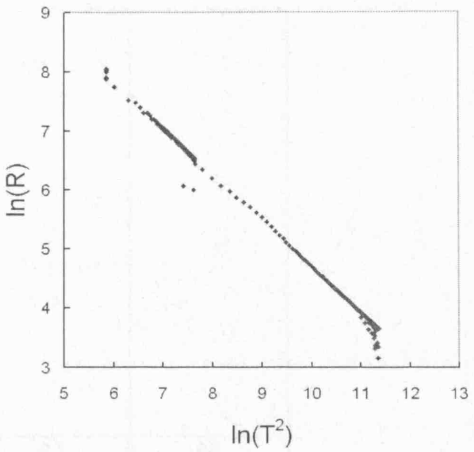

Figure 8.15. log(R) plotted against $\ln(T^2)$.

Capacitance voltage measurements can also be used to characterise the barrier height of a Schottky diode. C-V measurements were performed on ZnO tetrapod Schottky diodes at 100 kHz ac voltage. The superimposed ac voltage on a dc bias induces charge of one sign on the metal and the other on the semiconductor. This can be measured to obtain the capacitance of the Schottky junction as a function of applied bias and in turn used to calculate the barrier height. This method is reviewed in chapter 4. Figure 8.16 shows a Schottky-Mott plot of the voltage V against $1/C^2$.

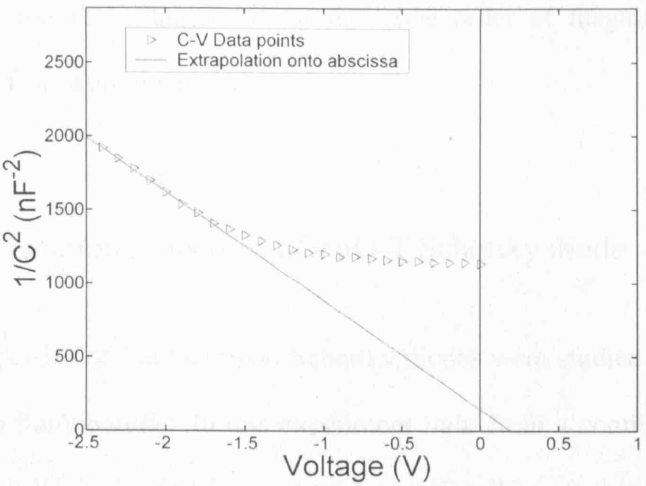

Figure 8.16. Schottky-Mott plot showing variation in the inverse square capacitance with voltage. Measurements performed using 100 KHz ac voltage at room temperature.

A fit to this curve is made at larger bias voltage where the change in capacitance is more accurately measured. Deviation from the extrapolation curve is observed at lower voltages and is a technical restraint that often causes difficulty when attempting to resolve the capacitance at lower voltages. Considering equation (4.68) which is shown below for brevity, extrapolation onto the abscissa yields $\phi - k_B T / e_0 = 0.19$ eV.

$$C_{sc} = \frac{\partial Q_{sc}}{\partial V_{sc}} = \left\{ \frac{e_0^2 \varepsilon \left(n_{cb} + p_{vb} \right)}{2\left(e_0 \phi - k_B T - e_0 V_{sc} \right)} \right\}^{1/2} \tag{4.68}$$

The band bending or potential is therefore given by $\phi = 0.22$ eV. Using the tabulated value for $\left(W_{cb} - W_F \right)$ found in appendix A and the results of figure 8.16, the barrier height is obtained as $\phi_{Bn} = 0.51$ eV. Barrier heights obtained from C-V measurements

are generally found to be larger but of the same order of magnitude than those obtained from I-V measurements [23].

8.5 Photo-detection properties of ZnO-T Schottky diode

The optical properties of ZnO tetrapod Schottky diodes were studied with above and below band gap illumination. In this experiment light from a continuous wave 325 nm UV laser (6 mW) and a 514.5 nm green laser (10 mW) is focussed into a micron sized spot which is then used to illuminate the tetrapod diode structure. Locating the tetrapod is made possible with confocal microscopy. Figure 8.17 shows the photoluminescence (PL) spectrum of a ZnO tetrapod Schottky diode. Characteristic peaks also seen in the PL spectrum of individual ZnO tetrapods and tetrapods clusters can be seen. As before the broad peak centred at 2.3 eV is attributed to surface defect states while the peak 3.2 eV is due to free exciton luminescence. The spectrum is noticeably weaker than that of an isolated ZnO-T and peak at 3.2 eV is less intense than the broad peak at 2.3 eV. Attaching metal contacts to the ZnO-T has therefore reduced the luminescence efficiency of the nanocrystal. Damage due to ion bombardment during the metal deposition process is a likely cause of the reduced efficiency. As the space-charge region extends approximately 100 nm into the nanocrystal (Section 4.4.2), it is also possible that this built in potential influences the efficiency of exciton recombination.

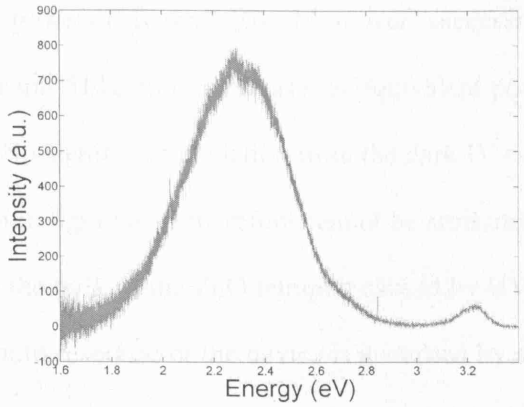

Figure 8.17. Photoluminescence spectrum of an unbiased ZnO tetrapod Schottky diode.

The response of the ZnO-T Schottky diode to above band gap illumination was studied by varying the power density of the light incident on the tetrapod nanocrystal. This was achieved by varying the distance of the nanocrystal from the focal point of the laser beam. The UV and green lasers were measured as having a beam spread (angular extent of the beam from the focal point) of $\pi/18$ and $\pi/3$ radians respectively. Figure 8.18 shows the I-V characteristics measured between Pt and W contacts as a function of UV illumination power density. Increasing the incident power density steadily caused the device to vary from rectifying to a more ohmic behaviour. This is further confirmed by the linear increase in current with illumination power density at 1V in reverse bias as shown figure 8.19. By assuming that the illumination is uniform over the whole tetrapod we obtain a responsivity of 10.6 A/W. Similar results of Schottky to ohmic conversion have been reported by Heo *et al.* and Keem *et al.* [11,12] for Schottky diodes employing ZnO nanorods. Little explanation however was provided for the operational mechanism.

For completeness we performed I-V measurements between both W contacts under UV illumination and observed minimal changes in the IV characteristics within the

same range of laser powers (Figure 8.20). Moreover, successive measurements were repeated with an Ar ion 514.5 nm green laser at equivalent power densities using the Schottky contacts. No significant deviation from the dark IV curve was observed. The response shown in figure 8.18 therefore cannot be attributed simply to an increase in carrier density in the bulk of the ZnO tetrapod caused by UV photo-excitation. We conclude that the photo response of the device is governed by a photo induced change in the electronic properties of the device at the metal semiconductor interface.

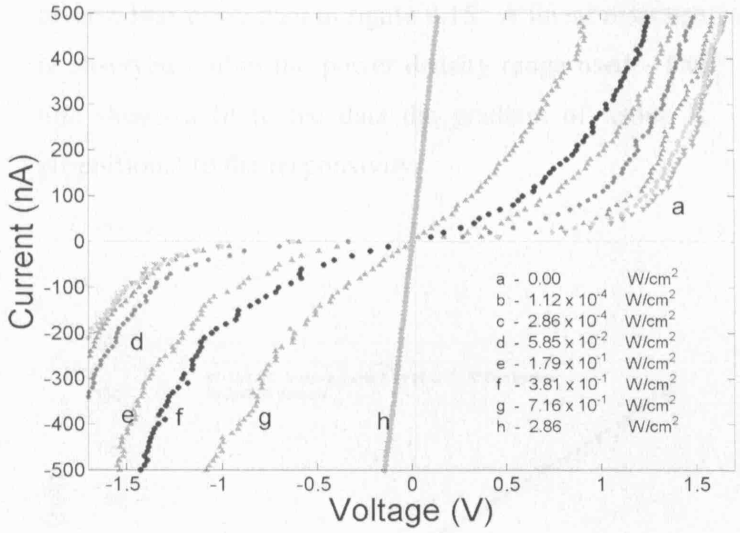

Figure 8.18. Photoresponse of ZnO tetrapod Schottky diode under 325 nm continuous wave illumination. Curve 'a' is the dark I-V. Curve 'h' is the I-V at high illumination.

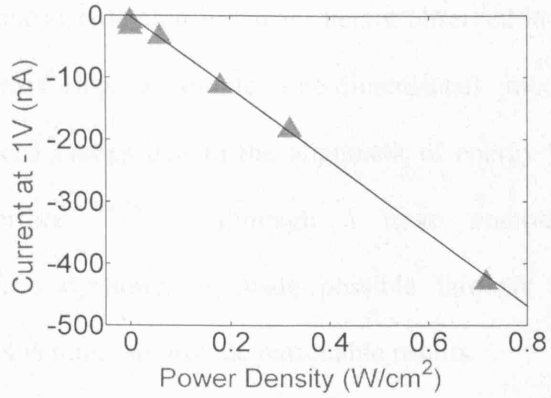

Figure 8.19. Photo generated current as a function illumination power density. Values are taken at 1 V in reverse bias using data in figure 8.15. A linear response is observed within the power density range used. The line shows a fit to the data the gradient of which is proportional to the responsivity.

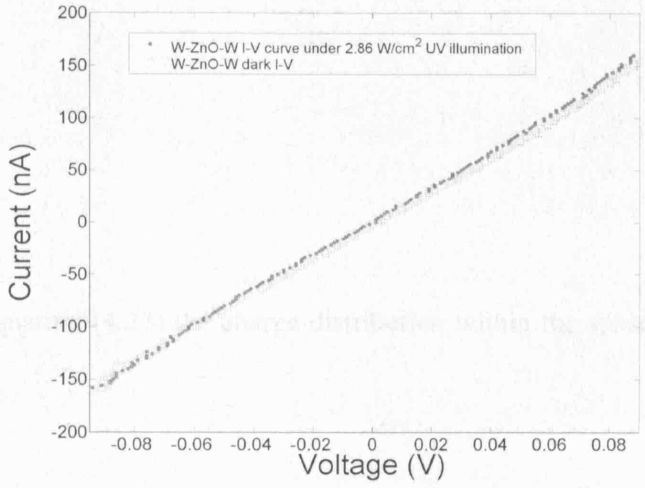

Figure 8.20. Photoresponse measured between two W contacts made to a ZnO tetrapod nanocrystal (W-ZnO-W).

The illumination induced reduction in barrier height observed in figure 8.15 may be understood by considering a simple one-dimensional model describing the distribution of induced charge due to the alignment of energy bands at the metal-semiconductor interface [24-26]. Although a more complete description of semiconductor surface dynamics is made possible through Shockley-Read-Hall statistics[27] this model is found to provide reasonable results.

In this model the fractional increase in electron and hole populations are taken to be spatially constant (flat quasi-Fermi levels approximation). This allows photo excited carrier densities Δn and Δp to be defined with reference to the thermal carrier concentrations in the bulk (see chapter 5). Hence normalised photo-excited electron and hole densities are defined as:

$$\gamma_n = \frac{n_0 + \Delta n}{n_0} \tag{8.3}$$

$$\gamma_p = \frac{p_0 + \Delta p}{p_0} \tag{8.4}$$

Considering equation (4.23) the charge distribution within the space-charge region is then given by:

$$\rho(z) = e_0 \left\{ n_c \left(1 - \gamma_n \exp(\upsilon)\right) - p_v \left(1 - \gamma_p \exp(-\upsilon)\right) \right\} \tag{8.5}$$

where z is the distance from the metal-semiconductor interface (with $z > 0$ in the semiconductor). The density of thermally excited electrons n_c and holes p_v in the bulk

are derived using a conduction and valence band density of states of 3.7×10^{24} and 3.4×10^{25} respectively[3,28]. The normalised potential is given by $\upsilon(z)=e_0\phi(z)/k_BT$ where $\phi(z)$ is the potential, k_B is the Boltzmann constant, T the absolute temperature and e_0 the charge on the electron. In the absence of photo illumination, equation (8.5) reduces to the standard expression for the charge distribution in the space-charge region of a Schottky diode. Substituting the charge density back into the Poisson equation and integrating yields the following space-charge distribution at the metal-semiconductor interface:

$$Q_{sc}=\eta\left(2\varepsilon_b\varepsilon_0 kT\right)^{1/2}\left(n_c\gamma_n(\exp(\upsilon)-1)-n_c\upsilon+p_v\gamma_p(\exp(-\upsilon)-1)+p_v\upsilon\right)^{1/2} \tag{8.6}$$

$$\eta=\begin{cases}-1 & \upsilon>0\\ +1 & \upsilon<0\end{cases} \tag{8.7}$$

Charge neutrality requires that $\Delta n=\Delta p$. The total charge within the space-charge region is therefore unaltered by illumination. The condition for charge neutrality at the metal semiconductor interface is therefore given as:

$$\begin{aligned}&p_v\left(\exp(-\upsilon_0)-\gamma_p\exp(-\upsilon)-1+\gamma_p\right)\\&-n_c\left(\gamma_n\exp(\upsilon)-\exp(\upsilon_0)-\gamma_n+1\right)+(\upsilon-\upsilon_0)(n_c-p_v)=0\end{aligned} \tag{8.8}$$

where υ_0 and υ represent the initial and resulting potential caused by above band gap illumination at the interface. For a given Δn, equation (8.8) can be solved self-consistently to obtain $\upsilon(0)$, the normalised potential at the metal-semiconductor

interface when illuminated. In order to obtain an estimate of Δn it is assumed that carriers are uniformly photo-excited in the ZnO up to a depth equal to the photon absorption length, d, from the surface. Hence Δn is equal to $\tau P / dh\nu$ where P is the irradiated power density, h is Planck's constant, ν the frequency of the UV photons and τ is the carrier lifetime. For the 325 nm photons used in this experiment, d is taken as 60 nm [29].

The results of this model are shown in figure 8.21. The results are plotted for carrier lifetimes τ in the range of 0.1 to 0.5 ns. In the model the value of the activation energy or barrier height at zero illumination is a free parameter and is taken as the initial barrier height of 0.43 eV. From the fit to the data we can conclude that band-flattening is indeed the photoresponse mechanism in our ZnO nanocrystal Schottky diodes, and that the lifetime of excited carriers is in the range 0.2 to 0.3 ns, consistent with previous reported measurements on ZnO films[30-32]. For larger power densities the activation energy tends to 0.25 eV. This suggests that the ZnO tetrapod contains deep donors arising from defect states, in agreement with previous measurements carried out for ZnO films.

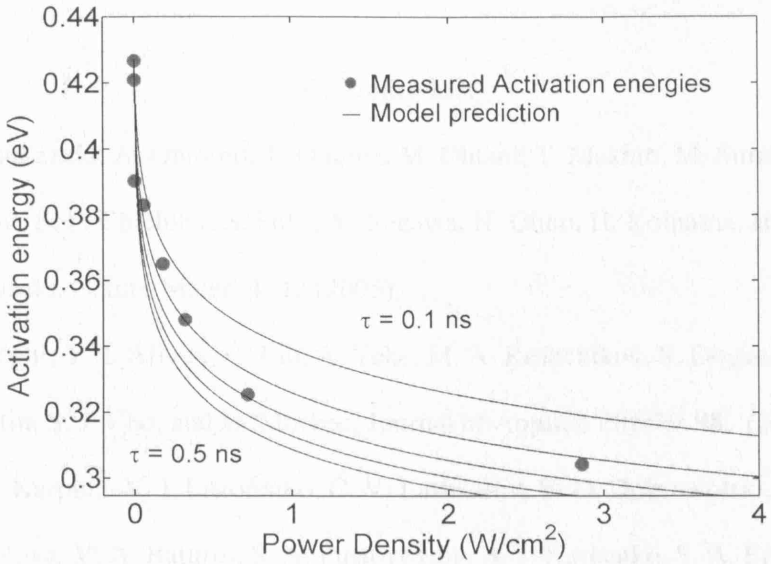

Figure 8.21. Activation energies, calculated from the thermionic emission theory, plotted as a function of illumination power density for τ = 0.1, 0.2, 0.3, 0.4, and 0.5 ns. Barrier heights at each illumination intensity show in figure 8.15 are also shown for comparison.

Summary

In conclusion, techniques for the deposition of both ohmic and Schottky contacts to ZnO nanocrystal tetrapods have been developed. From this ZnO tetrapod Schottky ultraviolet photodiodes were fabricated. The current-voltage characteristics of the device are altered from a rectifying nonlinear behaviour to a more ohmic behaviour under UV illumination. Focussed ion-beam assisted nanoscale fabrication methods are ideal for making prototype devices and measure the electronic properties of nanoscale structures.

Reference List

[1] A. Tsukazaki, A. Ohtomo, T. Onuma, M. Ohtani, T. Makino, M. Sumiya, K. Ohtani, S. F. Chichibu, S. Fuke, Y. Segawa, H. Ohno, H. Koinuma, and M. Kawasaki, Nature Mater. **4**, 42 (2005)

[2] U. Ozgur, Y. I. Alivov, C. Liu, A. Teke, M. A. Reshchikov, S. Dogan, V. Avrutin, S. J. Cho, and H. Morkoc, Journal of Applied Physics **98**, (2005)

[3] V. A. Karpina, V. I. Lazorenko, C. V. Lashkarev, V. D. Dobrowolski, L. I. Kopylova, V. A. Baturin, S. A. Pustovoytov, A. J. Karpenko, S. A. Eremin, P. M. Lytvyn, V. P. Ovsyannikov, and E. A. Mazurenko, Cryst. Res. Technol. **39**, 980 (2004)

[4] D. C. Look, B. Claflin, Y. I. Alivov, and S. J. Park, Phys. Status Solidi A **201**, 2203 (2004)

[5] Z.L.Wan, X.Y.Ko, Y.Di, P.G, W.L.Hug, s, R.Y, g, and Y.Zh, Adv. Func. Mater. **14**, 943 (2004)

[6] O. Schmidt, P. Kiesel, C. G. Van de Walle, N. M. Johnson, J. Nause, and G. H. Dohler, Jpn. J. Appl. Phys. ,Part 1 **44**, 7271 (2005)

[7] S. H. Kim, H. K. Kim, and T. Y. Seong, Appl. Phys. Lett. **86**, 112101 (2005)

[8] H. L. Mosbacker, Y. M. Strzhemechny, B. D. White, P. E. Smith, D. C. Look, D. C. Reynolds, C. W. Litton, and L. J. Brillson, Appl. Phys. Lett. **87**, 012102 (2005)

[9] O. Dulub, U. Diebold, and G. Kresse, Phys. Rev. Lett. **90**, 016102 (2003)

[10] W. Monch, Appl. Phys. Lett. **86**, 162101 (2005)

[11] K. Keem, H. Kim, G. T. Kim, J. S. Lee, B. Min, K. Cho, M. Y. Sung, and S. Kim, Appl. Phys. Lett. **84**, 4376 (2004)

[12] Y. W. Heo, L. C. Tien, D. P. Norton, S. J. Pearton, B. S. Kang, F. Ren, and J. R. LaRoche, Appl. Phys. Lett. **85**, 3107 (2004)

[13] T. Ishitani, *et al.*, Papers from the Japan/U.S.workshop on formation of ion nanobeams, AVS 16 , (1998), pp.2532-2537

[14] M. C. Newton, S. Firth, T. Matsuura, and P. A. Warburton, Journal of Physics: Conference Series , 251 (2006)

[15] W. D. Yu, X. M. Li, and X. D. Gao, Chem. Phys. Lett. **390**, 296 (2004)

[16] Z. Chen, Z. W. Shan, M. S. Cao, L. Lu, and S. X. Mao, Nanotech. **15**, 365 (2004)

[17] Y. C. Kong, D. P. Yu, B. Zhang, W. Fang, and S. Q. Feng, Appl. Phys. Lett. **78**, 407 (2001)

[18] Y. Zhang, H. Jia, X. Luo, X. Chen, D. Yu, and R. Wang, J. Phys. Chem. B **107**, 8289 (2003)

[19] R. Freer, J. Mater. Sci. **V15**, 803 (1980)

[20] H. Hajime, S. Isao, W. Akio, I. Takamasa, and T. Junzo, J. Electroceramics **V4**, 41 (1999)

[21] S. M. Sze, *Physics of Semiconductor Devices*, (Wiley, 1981).

[22] K. Ip, Y. W. Heo, K. H. Baik, D. P. Norton, S. J. Pearton, S. Kim, J. R. LaRoche, and F. Ren, Appl. Phys. Lett. **84**, 2835 (2004)

[23] D. M. Taylor and H. L. Gomes, J. Phys. D: Appl. Phys. **28**, 2554 (1995)

[24] M. C. Newton, S. Firth, and P. A. Warburton, Appl. Phys. Lett. **89**, 072104 (2006)

[25] C. G. B. Garrett and W. H. Brattain, Phys. Rev. **99**, 376 (1955)

[26] D. R. Frankl, Surf. Sci. **3**, 101 (1965)

[27] W. Shockley and W. T. Read, Phys. Rev. **87**, 835 (1952)

[28] J. A. Aranovich, D. Golmayo, A. L. Fahrenbruch, and R. H. Bube, J. Appl. Phys. **51**, 4260 (1980)

[29] J. F. Muth, R. M. Kolbas, A. K. Sharma, S. Oktyabrsky, and J. Narayan, J. Appl. Phys. **85**, 7884 (1999)

[30] A. Teke, U. Ozgur, S. Dogan, X. Gu, H. Morkoc, B. Nemeth, J. Nause, and H. O. Everitt, Phys. Rev. B **70**, 195207 (2004)

[31] X. J. Zhang, W. Ji, and S. H. Tang, J. Opt. Soc. Am. B **14**, 1951 (1997)

[32] C. K. Sun, S. Z. Sun, K. H. Lin, K. Y. Zhang, H. L. Liu, S. C. Liu, and J. J. Wu, Appl. Phys. Lett. **87**, 023106 (2005)

9. Conclusions and Future Prospects

9.1 Conclusions

We have reviewed the current status of research into ZnO materials and devices. ZnO is a wide band gap semiconductor that shows a rich variety of optical properties at room temperature largely mediated by its large exciton binding energy of 60 meV. ZnO may therefore play a key role in future optoelectronic devices. We have also reviewed the properties of polar and non-polar ZnO surfaces. Polar ZnO surfaces were found to be remarkably stable in ambient conditions. The mechanism by which this occurs, however, remains unclear.

The aim of this work was to synthesise and study the properties of ZnO tetrapod nanocrystals and to fabricate diodes based on a single ZnO tetrapod nanocrystal. ZnO tetrapod nanocrystals were fabricated using a chemical vapour transport and deposition process. A degree of control over their size and morphology was achieved. ZnO tetrapods were characterised mainly using optical techniques such as FTIR, Raman and photoluminescence (PL) spectroscopy. FTIR measurements revealed the presence of bulk and surface phonon modes while Raman measurements revealed fundamental phonon modes. All PL measurements on ZnO were found to be highly sensitive to the surface composition. PL measurements of ZnO tetrapods showed both defect and band edge emission. Moreover, we have demonstrated that the broad defect related emission peak originates from defects at the surface of the nanocrystal and is not due to bulk impurities as is often suggested within the literature. We have shown that with the correct surface treatment, defect related emission can be suppressed.

In studying free standing ZnO tetrapods, resonant cavity modes were observed in a single ZnO tetrapod nanocrystal under continuous wave illumination. This finding demonstrates for the first time that a single ZnO nanocrystal can operate as a Fabry-Perot resonant cavity. This is an important finding as it shows that although these structures are nanoscale in size, certain macroscopic properties remain and can be observed. It was found that the characteristic length of the cavity modes corresponds to that of the length of two arms of the tetrapod suggesting that these modes propagate throughout the tetrapod nanocrystal. A study of the dependence of the cavity modes on the size and morphology of the tetrapod crystal would shed some light on the exact nature of the resonance. Questions such as 'how many of the arms couple to the resonance' remain unanswered.

Finally, electrical contacts were also made to a single ZnO tetrapod nanocrystal using focussed ion-beam (FIB) assisted deposition of W and Pt metals. This device configuration was shown to function as a photosensitive Schottky diode. Similar device structures had recently appeared in the literature employing other ZnO nanocrystal structures. Little explanation has however been provided for the mechanism by which this device structure operates leading to a series of conflicting ideas within the literature. In this work we have explicitly shown that the UV sensitive device like characteristics are a direct result of the illumination induced reduction in the Schottky barrier height formed at the metal-semiconductor interface.

9.2 Future prospects

Research into ZnO has recently intensified due to the realisation of reliable techniques for thin film deposition. ZnO is therefore a viable contender to the industry standard of GaN for UV optoelectronic devices. Moreover ZnO has been shown to form a

wide variety of nanoscale crystalline structures which are readily synthesised. There are a number of applications for which these structures may find use including piezoelectric transducers, gas sensors and optical sensors. The ability to manipulate nanoscale structures is a major hurdle to be overcome if they are to be employed as functional materials in devices. In this work we have made significant progress into the study of individual nanostructures. Moreover we have shown that a single ZnO nanoscale crystal can be utilised as a functional material within a device structure. The observation of high performance operational characteristics of this device structure is a significant advancement as it demonstrates that the unique properties of an individual nanoscale structure can indeed be exploited. Further studies into fundamental optical properties that occur at the nanoscale are also encouraged by our observation of resonant cavity modes within a single tetrapod nanocrystal.

The surface properties of the tetrapod nanocrystal were shown to influence the luminescence spectrum. A study of the interfacial properties of the tetrapod nanocrystal with metal contacts may shed some light on the transport mechanisms at each interface and the role of defect states. This may however be limited by the fact that most spectroscopic and microscopy techniques are not amenable to characterising non-planar surface at the nanoscale. Wavelength dependent surface photovoltage spectroscopy does however provide a means of indirectly determining the presence of surface states at the metal-semiconductor interface.

The integration of nanoscale structures into devices is ever approaching as research intensifies and new techniques for the control and manipulation of nanoscale structures emerge. The field of nanoscale structures and devices is one that promises to provide revolutionary changes and hopefully improvements to the modern world.

Appendices

Appendix A

A.1 Electronic Properties of Wurtzite ZnO

Property	Symbol	Value	Units	Ref.
Electronic band gap	E_g	3.37	eV	1
A-B valence band separation	E_{AB}	4.9	meV	2
B-C valence band separation	E_{BC}	43.7	meV	2
Electron effective mass	m_e^*	0.24	m_0	1
Hole effective mass	m_h^*	0.79	m_0	3
Electron hall mobility	μ_e	120	cm^2/Vs	4
Electron carrier concentration	n	1.2×10^{17}	cm^{-3}	4
Work Function $(10\bar{1}0)$	W_F	4.64	eV	5
Electron affinity	χ	4.35	eV	6
Ionisation energy	I	7.72	eV	
Branch point energy	W_{bp}	3.04	eV	7
Exciton binding energy	E_{ex}^b	60	meV	1
Biexciton binding energy	E_{xx}^b	15	meV	8,9
Exciton Bohr Radius	a_{ex}	2.34	nm	10
Electron polaron Radii	R_e	14.8	Å	11
Hole polaron Radii	R_h	8.28	Å	11

A.2 Optical Properties of Wurtzite ZnO

Property	Symbol	Value	Units	Ref.
Refractive index ($\hbar\omega = 3.3$ eV)	η	2.4	~	12
Polarisability	$\tilde{\alpha}$	7.7×10^{-3}	cm^{-3}	13
Static dielectric constants	$\varepsilon_0^{\parallel}$	8.49	ε_0	12
	$\varepsilon_0^{\perp}$	7.40	ε_0	12
Optical dielectric constants	$\varepsilon_\infty^{\parallel}$	3.72	ε_0	12
	$\varepsilon_\infty^{\perp}$	3.68	ε_0	12
TO (E_2) phonon mode	E_2^{low}	101	cm^{-1}	2
LO (E_2) phonon mode	E_2^{high}	437	cm^{-1}	2
LO (A_1) phonon mode	A_1^{LO}	574	cm^{-1}	14
TO (A_1) phonon mode	A_1^{TO}	380	cm^{-1}	2
LO (E_1) phonon mode	E_1^{LO}	583	cm^{-1}	15
TO (E_1) phonon mode	E_1^{TO}	407	cm^{-1}	15
Free A-Exciton	$FX_A^{n=1}$	3.3771	eV	16
Free B-Exciton	$FX_B^{n=1}$	3.3898	eV	16
Free C-Exciton	$FX_C^{n=1}$	3.435	eV	16
LPB M-bands	M_1	3.362	eV	14
	M_2	3.348	eV	14
	M_3	3.322	eV	14
UPB T-bands	T	3.412	eV	14
Photo excited carrier lifetime	τ	10^{-9}	s	17

Reference List

[1] V. A. Karpina, V. I. Lazorenko, C. V. Lashkarev, V. D. Dobrowolski, L. I. Kopylova, V. A. Baturin, S. A. Pustovoytov, A. J. Karpenko, S. A. Eremin, P. M. Lytvyn, V. P. Ovsyannikov, and E. A. Mazurenko, Cryst. Res. Technol. **39**, 980 (2004)

[2] B. K. Meyer, H. Alves, D. M. Hofmann, W. Kriegseis, D. Forster, F. Bertram, J. Christen, A. Hoffmann, M. Strassburg, M. Dworzak, U. Haboeck, and A. V. Rodina, Phys. Status Solidi B **241**, 231 (2004)

[3] B. Enright and D. Fitzmaurice, J. Phys. Chem. **100**, 1027 (1996)

[4] K. Miyamoto, M. Sano, H. Kato, and T. Yao, J. Cryst. Growth **265**, 34 (2004)

[5] W. Gopel, L. J. Brillson, and C. F. Brucker, Journal of Vacuum Science and Technology **17**, 894 (1980)

[6] H. Moormann, D. Kohl, and G. Heiland, Surf. Sci. **80**, 261 (1979)

[7] W. Monch, Appl. Phys. Lett. **86**, 162101 (2005)

[8] H. J. Ko, Y. F. Chen, T. Yao, K. Miyajima, A. Yamamoto, and T. Goto, Appl. Phys. Lett. **77**, 537 (2000)

[9] H. D. Sun, Y. Segawa, T. Makino, C. H. Chia, M. Kawasaki, A. Ohtomo, K. Tamura, and H. Koinuma, Phys. Status Solidi B **229**, 867 (2002)

[10] Y. Gu, I. L. Kuskovsky, M. Yin, S. O'Brien, and G. F. Neumark, Appl. Phys. Lett. **85**, 3833 (2004)

[11] R. T. Senger and K. K. Bajaj, Phys. Rev. B **68**, 045313 (2003)

[12] H. Yoshikawa and S. Adachi, **36**, 6237 (1997)

[13] J. J. Hopfield and D. G. Thomas, J. Phys. Chem. Solids **12**, 276 (1960)

[14] T. V. Butkhuzi, T. G. Chelidze, A. N. Georgobiani, D. L. Jashiashvili, T. G. Khulordava, and B. E. Tsekvava, Phys. Rev. B **58**, 10692 (1998)

[15] T. C. Damen, S. P. S. Porto, and B. Tell, Phys. Rev. **142**, 570 (1966)

[16] A. Teke, U. Ozgur, S. Dogan, X. Gu, H. Morkoc, B. Nemeth, J. Nause, and H. O. Everitt, Phys. Rev. B **70**, 195207 (2004)

[17] X. J. Zhang, W. Ji, and S. H. Tang, J. Opt. Soc. Am. B **14**, 1951 (1997)

Appendix B

B.1 Multiplication table for the irreducible representation of the group in the C_{6v} symmetry.

$\otimes$	Γ_1	Γ_2	Γ_3	Γ_4	Γ_5	Γ_6	Γ_7	Γ_8	Γ_9
Γ_1	Γ_1	Γ_2	Γ_3	Γ_4	Γ_5	Γ_6	Γ_7	Γ_8	Γ_9
Γ_2		Γ_1	Γ_4	Γ_3	Γ_5	Γ_6	Γ_7	Γ_8	Γ_9
Γ_3			Γ_1	Γ_2	Γ_6	Γ_5	Γ_8	Γ_7	Γ_9
Γ_4				Γ_1	Γ_6	Γ_5	Γ_8	Γ_7	Γ_9
Γ_5					$\Gamma_1+\Gamma_2+\Gamma_6$	$\Gamma_3+\Gamma_4+\Gamma_5$	$\Gamma_7+\Gamma_9$	$\Gamma_8+\Gamma_9$	$\Gamma_7+\Gamma_8$
Γ_6						$\Gamma_1+\Gamma_2+\Gamma_6$	$\Gamma_8+\Gamma_9$	$\Gamma_7+\Gamma_9$	$\Gamma_7+\Gamma_8$
Γ_7							$\Gamma_1+\Gamma_2+\Gamma_5$	$\Gamma_3+\Gamma_4+\Gamma_6$	$\Gamma_3+\Gamma_4$
Γ_8								$\Gamma_1+\Gamma_2+\Gamma_5$	$\Gamma_5+\Gamma_6$
Γ_9									$\Gamma_1+\Gamma_2$
									$\Gamma_3+\Gamma_4$

B.2 Compatibility table of the irreducible representation of angular momentum $L_z \le 6$ and $J_z \le 13/2$ with the C_{6v} symmetry group. Odd and even parity are represented by – and + respectively.

D_0^+	Γ_1	D_0^-	Γ_2
D_1^+	$\Gamma_2+\Gamma_5$	D_1^-	$\Gamma_1+\Gamma_5$
D_2^+	$\Gamma_1+\Gamma_5+\Gamma_6$	D_2^-	$\Gamma_2+\Gamma_5+\Gamma_6$
D_3^+	$\Gamma_2+\Gamma_3+\Gamma_4+\Gamma_5+\Gamma_6$	D_3^-	$\Gamma_1+\Gamma_3+\Gamma_4+\Gamma_5+\Gamma_6$
D_4^+	$\Gamma_1+\Gamma_3+\Gamma_4+\Gamma_5+\Gamma_6$	D_4^-	$\Gamma_2+\Gamma_3+\Gamma_4+\Gamma_5+\Gamma_6$
D_5^+	$\Gamma_2+\Gamma_3+\Gamma_4+\Gamma_5+\Gamma_6$	D_5^-	$\Gamma_1+\Gamma_3+\Gamma_4+\Gamma_5+\Gamma_6$
D_6^+	$2\Gamma_1+\Gamma_2+\Gamma_3+\Gamma_4+2\Gamma_5+2\Gamma_6$	D_6^-	$\Gamma_1+2\Gamma_2+\Gamma_3+\Gamma_4+2\Gamma_5+2\Gamma_6$

$D_{1/2}^{+}$	Γ_7	$D_{1/2}^{-}$	Γ_7
$D_{3/2}^{+}$	$\Gamma_7+\Gamma_9$	$D_{3/2}^{-}$	$\Gamma_7+\Gamma_9$
$D_{5/2}^{+}$	$\Gamma_7+\Gamma_8+\Gamma_9$	$D_{5/2}^{-}$	$\Gamma_7+\Gamma_8+\Gamma_9$
$D_{7/2}^{+}$	$\Gamma_7+2\Gamma_8+2\Gamma_9$	$D_{7/2}^{-}$	$\Gamma_7+2\Gamma_8+2\Gamma_9$
$D_{9/2}^{+}$	$\Gamma_7+2\Gamma_8+\Gamma_9$	$D_{9/2}^{-}$	$\Gamma_7+2\Gamma_8+\Gamma_9$
$D_{11/2}^{+}$	$2\Gamma_7+2\Gamma_8+2\Gamma_9$	$D_{11/2}^{-}$	$2\Gamma_7+2\Gamma_8+2\Gamma_9$
$D_{13/2}^{+}$	$3\Gamma_7+2\Gamma_8+2\Gamma_9$	$D_{13/2}^{-}$	$3\Gamma_7+2\Gamma_8+2\Gamma_9$

B.3 Selection Rules

In going from an initial state $|i\rangle$ with symmetry Γ_i to a final states $\langle f|$ with symmetry Γ_f under the operator H_s that transforms according the symmetry state Γ_s, the transmission matrix elements M_{if} are given as:

$$M_{if} \propto \langle f|H_s|i\rangle \tag{B.1}$$

A matrix element is either zero or non-zero according to the following:

$$\langle f|H_s|i\rangle \begin{cases} \neq 0 & \text{if } \Gamma_f \subset \Gamma_i \otimes \Gamma_s \\ \neq 0 & \text{if } \Gamma_1 \subset \Gamma_f \otimes \Gamma_i \otimes \Gamma_s \\ = 0 & \text{otherwise} \end{cases} \tag{B.2}$$

Optical selection rules can be calculated on this basis. For crystals with C_{6v} symmetry the dipole operator has Γ_1 symmetry for $\boldsymbol{E} \parallel \boldsymbol{c}$ and Γ_5 symmetry for $\boldsymbol{E} \perp \boldsymbol{c}$. For wurtzite ZnO in the tight binding approximation the upper most valence band is formed from the filled 2p shell of O^{-2} while the conduction band is formed from emptied 4s shell of Zn^{+2}. Considering the compatibility table shown above the following band symmetries apply for C_{6v} asymmetry:

Conduction band : $4s \Rightarrow D_{1/2} \Rightarrow \Gamma_7$ (B.3)

Valence band : $2p \Rightarrow \begin{cases} D_{3/2} \Rightarrow \Gamma_7 + \Gamma_9 \\ D_{1/2} \Rightarrow \Gamma_7 \end{cases}$ (B.4)

So, for one photon transitions, traversing from a ground state with symmetry Γ_7 to a state Γ_7 with $E \| c$ polarisation, the transition is allowed. If the initial state has Γ_9 symmetry, the transition is however forbidden [1,2].

Reference List

[1] C. Klingshirn, *Semiconductor Optics*, (Springer, Berlin, 2005).

[2] J. L. Birman, Phys. Rev. **114**, 1490 (1959)

Appendix C

Electronic Charge Transport Equations for Semiconductor Devices

The application of an external field to a semiconducting material results in a deviation from the equilibrium static and dynamical behaviour of electronic charge carriers. The equations that govern this behaviour can be categorised as Maxwell's equations, current density equations and continuity equations [1-3].

C.1 Maxwell's Equations

$$\nabla \times \boldsymbol{E} = -\dot{\boldsymbol{B}} \tag{C.1}$$

$$\nabla \times \boldsymbol{H} = \boldsymbol{J} + \dot{\boldsymbol{D}} \tag{C.2}$$

$$\nabla \cdot \boldsymbol{D} = \rho(\boldsymbol{x}) \tag{C.3}$$

$$\nabla \cdot \boldsymbol{B} = 0 \tag{C.4}$$

$$\boldsymbol{B} = \mu_0 \boldsymbol{H} + \boldsymbol{M} \tag{C.5}$$

$$\boldsymbol{D} = \varepsilon_0 \boldsymbol{E} + \boldsymbol{P} = \varepsilon \boldsymbol{E} \tag{C.6}$$

The various symbols have the following meaning:

$\boldsymbol{E}$ = Electric field strength	(V m^{-1} = m kg s^{-3} A^{-1})
$\boldsymbol{D}$ = Electric displacement	(A s m^{-2})
$\boldsymbol{H}$ = Magnetic field strength	(A m^{-1})
$\boldsymbol{B}$ = Magnetic flux density	(V s m^{-2})
$\boldsymbol{M}$ = Magnetisation density	(V s m^{-2})
$\boldsymbol{P}$ = Polarisation density	(A s m^{-2})
$\boldsymbol{J}$ = Current density	(A m^{-2})
ε = Dielectric tensor	(A s V^{-1} m^{-1})

ε_0 = Permittivity of free space (A s V^{-1} m^{-1})

ρ = Charge density (A s m^{-3})

μ_0 = Permeability of free space (V s A^{-1} m^{-1})

C.2 Current Density Equations

$$\boldsymbol{J}_n = e_0 \mu_n n E + e_0 D_n \nabla n \tag{C.7}$$

$$\boldsymbol{J}_p = e_0 \mu_p p E + e_0 D_p \nabla p \tag{C.8}$$

$$\boldsymbol{J} = \boldsymbol{J}_p + \boldsymbol{J}_p \tag{C.9}$$

$$n = \int_{W_c}^{W_-} dW \cdot g_c(W) f_0(W) \tag{C.10}$$

$$D_i = \left(\frac{kT}{e_0}\right)\mu_i \quad , i = n, p \tag{C.11}$$

$$v_d = \mu E \tag{C.12}$$

The various symbols have the following meaning:

$\boldsymbol{J}_n$ = Electron current density (A m^{-2})

$\boldsymbol{J}_p$ = Hole current density (A m^{-2})

n = Electron concentration (cm^{-3})

p = Hole concentration (cm^{-3})

μ_n = Electron mobility (cm^2 V^{-1} s^{-1})

μ_p = Hole mobility (cm^2 V^{-1} s^{-1})

D_i = Carrier diffusion coefficient (cm^2 s^{-1})

v_d = Drift velocity (cm s^{-1})

C.3 Continuity Equations

$$\frac{\partial n}{\partial t} = \frac{1}{e_0}\nabla \cdot \boldsymbol{J}_n + G_n - U_n \qquad \text{(C.12)}$$

$$\frac{\partial p}{\partial t} = \frac{1}{e_0}\nabla \cdot \boldsymbol{J}_p + G_p - U_p \qquad \text{(C.13)}$$

$$G_i = \frac{\Delta i}{\tau_i} \quad , i = n, p \qquad \text{(C.14)}$$

The various symbols have the following meaning:

G_n = Electron generation rate ($cm^{-3}\ s^{-1}$)

G_p = Hole generation rate ($cm^{-3}\ s^{-1}$)

U_n = Electron recombination rate ($cm^{-3}\ s^{-1}$)

U_p = Hole recombination rate ($cm^{-3}\ s^{-1}$)

τ_i = Excited carrier lifetime (s)

Δn = Excited electron density (cm^{-3})

Δp = Excited hole density (cm^{-3})

Reference List

[1] S. M. Sze, *physics of semiconductor devices*, (Wiley, 11981).

[2] P. Morse and H Feshbach, *methods of theoretical physics*, (McGraw Hill, 1953).

[3] H. Lüth, *solid surfaces, interfaces and thin films*, (Springer, 2001).

Appendix D

The following text is Matlab code used to calculate the change in activation energy with illumination power density for a Pt-ZnO Schottky diode.

```
% Calculates the surface band bending as a function of illumination power
% density

clear all

% Density of states constants:
m_0 = 9.1*10^-31;
m_e = 0.28*m_0;
m_h = 0.59*m_0;
M_c = 1;
M_v = 3;
K  = 1.38*10^-23;
T  = 300;
h  = 6.6*10^-34;

% Density of states for n and p:
N_c = 2*M_c*(2*pi*m_e*K*T/h^2)^(1.5);
N_v = 2*M_v*(2*pi*m_h*K*T/h^2)^(1.5);

% photoexcited carrier density constants:
e_0 = 1.6*10^-19;
E  = 3.8 * e_0;     % photon energy for 3.8eV (325nm) source
tau = 0.5*10^-9;     % carrier lifetime
d  = 60*10^-9;      % penetration depth of UV light

% Carrier density n and p:
W_c_ZnO_eV = -4.35;  %energy level (not work function)
W_v_ZnO_eV = -7.82;  %energy level (not work function)
W_F_ZnO_eV = -4.65   % work function of ZnO (eV) - This value will directly affect the surface band
bending

W_c_ZnO = W_c_ZnO_eV * e_0;   %energy level (not work function)
W_v_ZnO = W_v_ZnO_eV * e_0;   %energy level (not work function)
W_F_ZnO = W_F_ZnO_eV * e_0;   %work function of ZnO (joules)


n_c = N_c*exp((W_F_ZnO - W_c_ZnO)/(K*T));
n_v = N_v*exp((W_v_ZnO - W_F_ZnO)/(K*T));

% Band bending:
barrier_height =  - 0.427; % negative value for n-type semiconductor
ofset = 0.25 %2975;
thi = barrier_height + ofset;         % *band bending* (not barrier height!) in electron volts (negative
value for n-type semiconductor)
v  = e_0*thi/(K*T);

% spacially varying carrier densities:
n_0 = n_c; %  " exp(v)" cancels out in small signal analysis
```

```
p_0 = n_v; %  " exp(-v)" cancels out in small signal analysis



% Power interval array:
max_power_factor = 4;
interval_factor = 0.01;
scale  = 1;
max_power = max_power_factor * scale;                  % power in W/cm*cm
interval = interval_factor * scale;                  % power in W/cm*cm
power_density = 0:interval:max_power;                  % power in W/cm*cm
power_density_muW = 0:interval_factor:max_power_factor; % power in micro W/cm*cm (used for
plot)


options = optimset('Display','iter','TolFun',1e-9); % passes display and convergence tollerence
parameters to fzero function

f_1 = inline('n_v*( exp(-v) - y_p*exp(-u) + y_p - 1 ) - n_c*( y_n*exp(u) - exp(v) - y_n  + 1 ) + (n_c -
n_v)*(u-v)','u','n_c', 'n_v', 'v', 'y_n','y_p');

u_last=v;

% band bending calculation:
for step = 1:(max_power_factor/interval_factor + 1),

   G      = power_density(step)*(10^4)/(E*d);  % extra factor of 10^4 to comply with SI units
   delta_n = G * tau;

   y_n    = (n_0 + delta_n)/n_0;
   y_p    = (p_0 + delta_n)/p_0;

   u=fzero(f_1,(u_last),options,n_c,n_v,v,y_n,y_p); % The value of u_last is used as location of initial
solution

   u_last = u;

   u_array(step)=  (-(K*T/e_0)*u); %negative value for graphical perposes


end


plot(power_density_muW,u_array,'k');
```

Appendix E

X-ray Photoelectron Spectroscopy Lookup Table

| | | |

82.0	Br	loss	101.8	Si	Almand.	119.4	Ga	loss	137.8	Pb	2O3	158.9	Y	2(CO3)3	181.0	Ge	3s	204.1	Nb	NbO	235.3	Mg	Auger
82.0	Mn	3s	101.9	Hg	4f	119.4	Tl	CO3	137.8	Se	Auger	159.2	Bi	Ntv Ox	181.1	Zr	3d3	205.0	Nb	3d3	237.0	Pm	4p3
82.7	Pb	5p3	102.0	Pt	5s	120.0	Hg	5s	138.3	Pb	4f	159.6	Ho	4d5	181.2	Br	3p3	205.1	S	loss	237.6	Ta	4d3
84.0	Au	4f7	102.0	Si	3N4	120.0	Tl	4f	138.5	Ge	loss	160.0	Bi	5s	182.0	Br	3p	205.8	Lu	4d3	237.9	Rb	3p3
84.0	Ba	4d3	102.6	Si	O	121.0	Pm	4d	138.8	Pb	Ntv Ox	161.2	S	PbS	182.0	Fr	5p1	206.1	Nb	NbO2	238.0	Cs	4s
84.7	Ba	4d	102.9	Zn	loss	121.1	I	4p	139.0	Pb	CO3	161.3	Ho	2O3	182.1	Yb	4d5	207.0	Ce	4p3	238.0	Rn	4f
85.0	Au	4f	103.0	Ga	3p	122.0	Ge	3p3	139.0	Xe	4p	161.5	S	CuS, TaS2	182.4	Zr	O2	207.0	Xe	4s	238.9	Mo	loss
85.0	Th	5d5	103.0	Ga	3p3	122.1	Tl	4f5	139.5	Zn	3s	161.7	Se	3p3	182.8	Er	Auger	207.3	P	loss	241.8	Ar	2p3
86.0	Ba	4d5	103.0	Pt	loss	122.4	Cu	3s	140.0	Fr	5p3	161.9	S	HgS	183.7	Si	loss	207.4	Nb	Nb2O5	242.0	Ar	2p
86.9	Kr	3d5	103.0	Si	O2	122.4	In	4s	140.3	Gd	4d5	162.2	S	MoS2	184.0	Po	4f	207.4	Nb	Ntv Ox	243.1	W	4d5
87.2	Kr	3d	103.0	U	5d3	127.0	Rn	5p3	140.7	As	3p3	162.3	Bi	4f5	184.9	Yb	2O3	208.0	Kr	3p3	243.9	Ar	2p1
87.7	Au	4f5	103.5	Si	O2-nH2O	128.2	Eu	4d5	141.2	Gd	2O3	162.4	S	Na2S2O3	185.3	S	loss	210.0	At	4f	245.0	Nd	4p1
88.0	Al	loss	103.7	Al	loss	128.3	Tl	loss	141.7	Pb	4f5	162.6	S	FeS2	185.5	I	4s	210.8	Hf	4d5	248.0	Ba	4s
88.1	Au	2O3	103.9	Hg	4f5	128.6	P	InP etch	142.0	As	3p	163.9	S	2p3	187.8	Br	3p1	210.9	Dy	Auger	248.0	Rb	3p1
88.2	Kr	3d3	104.0	La	4d	129.0	Ge	3p1	145.9	Tb	4d5	164.0	Rn	5p1	187.9	B	CrB	213.0	B	loss	249.6	S	loss
88.2	Pd	4s	104.0	Po	5p3	129.0	P	InP etch	146.0	Sr	loss	164.0	S	2p	188.0	B	1s	213.0	La	4p1	250.0	Sm	4p3
88.3	Zn	3p	106.3	Pb	5p1	129.0	Sm	4d	147.0	As	3p1	164.0	Sr	loss	188.0	B	MoB, LaB6	214.0	Rn	5s	253.0	Mo	loss
89.0	Os	5s	107.0	Ga	3p1	129.3	P	GaP etch	148.0	At	5p1	165.1	S	2p1	188.1	B	WB	217.5	Cl	loss	253.0	Tc	3d
89.1	Mg	2s	108.0	Au	5s	130.0	Be	loss	148.0	Pb	5s	166.6	S	Na2SO3	188.2	B	Ni3B	218.0	Pr	4p3	253.0	Tc	3d5
90.6	Sn	4p	109.7	Rb	3d5	130.0	Ho	Auger	148.5	Tb	F3	167.3	Er	4d5	188.9	B	Ntv Ox	220.5	Se	Auger	254.0	Ra	5s
91.0	Fe	3s	109.7	Rb	OAc	130.1	P	2p3	148.8	Al	loss	167.3	Se	3p1	189.0	P	2s	221.3	Hf	4d3	255.0	Br	3s
92.8	Bi	5p3	109.9	Cd	4s	130.6	P	2p	149.8	Pb	loss	167.6	Si	loss	189.2	Tm	Auger	223.0	Ce	4p1	255.0	Eu	4p3
93.0	Th	5d3	110.0	Ce	4d	131.4	P	2p1	149.9	P	loss	168.5	Er	2O3	190.8	B	N	225.7	As	3s	255.0	Pm	4p1
94.0	U	5d5	110.0	Rb	3d	132.0	Po	5p1	149.9	Tb	3O7	168.5	S	Na2SO4	190.9	Yb	4d3	226.1	Ta	4d5	255.1	Se	Auger
94.6	Tl	5p1	110.5	Ni	3s	132.7	Ga	loss	150.5	Si	2s	168.5	S	Na2S2O3	194.0	B	2O3	228.0	Mo	3d5	255.6	W	4d3
95.2	Ir	5s	110.6	Mg	loss	133.4	Al	loss	152.0	Zn	loss	168.6	P	loss	195.0	At	5s	228.0	Nd	4p3	257.0	Tc	3d3
96.0	Br	loss	111.2	Rb	3d3	133.6	Si	loss	152.3	Dy	4d5	168.8	Y	loss	195.0	U	5p3	229.0	S	2s	260.0	Re	4d5
97.0	Ag	4s	111.8	Be	1s	133.7	Sr	3d5	152.9	Sb	4s	169.1	Te	4s	196.0	Lu	4d5	229.4	Mo	O2 (?)	260.0	U	5p1
98.7	Er	Auger	112.6	Te	4p	133.7	Sr	CO3	153.0	Ra	5p3	169.3	Er	4d3	196.1	Zr	loss	229.5	Mo	3d	261.0	As	Auger
99.8	Si	2p3	113.6	Be	O	134.0	Sr	3d	155.8	Y	3d5	173.0	Ba	4p	197.0	La	4p3	229.7	Mo	S2	261.5	Tb	Auger
99.8	Mg	loss	114.7	Be	Ntv Ox	134.9	Sm	2O3	156.1	Dy	2O3	173.3	Ga	loss	197.5	Ge	Auger	229.9	Se	3s	264.3	Rb	loss
99.9	Hg	4f7	115.0	At	5p3	135.5	Sr	3d3	156.6	Y	2O3	175.4	Tm	4d	198.4	Se	Auger	230.0	As	Auger	267.5	S	loss
100.1	Si	2p	115.0	Pr	4d	135.6	Eu	2O3	157.0	Bi	4f7	175.9	Tb	loss	198.7	Cl	2p	231.1	Mo	3d3	267.7	W	loss
100.2	Si	O	115.5	Se	Auger	136.8	Pb	O2	157.0	Bi	4f	176.3	Tm	2O3	198.9	Cl	2p3	232.6	Mo	Ntv Ox	268.0	Fr	4f
100.4	Si	2p1	116.2	Si	loss	136.8	Rb	loss	157.0	Bi	loss	177.0	Po	5s	198.9	Cl	MCl	232.9	Tb	Auger	268.4	Sr	3p3
100.4	Si	C	117.7	Tl	4f7	136.9	Pb	4f7	157.0	Y	3d	177.0	Th	5p3	199.8	Cl	C-Cl	233.0	Kr	3p1	270.0	Cl	2s
100.6	Sb	4p	117.9	Al	2s	137.0	Tl	5s	157.9	Y	3d3	178.7	Se	Auger	200.0	Ra	5p1	233.1	Mo	O3	271.3	Gd	4p3
100.7	Hg	O	118.0	Nd	4d	137.1	Sn	4s	158.5	Cs	4p3	178.7	Zr	3d5	200.5	Cl	2p1	234.0	Fr	5s	273.5	Re	4d3
100.9	Co	3s	118.2	Bi	5p1	137.5	Pb	O	158.8	Bi	2O3	179.9	Zr	3d	201.4	Nb	3d	234.0	Pr	4p1	274.5	Er	Auger
100.9	Hg	S	118.2	Tl	2O3	137.6	Pb	3O4	158.9	Ga	3s	180.9	Cs	4p1	202.3	Nb	3d5	234.0	Th	5p1	275.0	La	4s

| | | |

| | | |

Appendix F

List of Publications

[1] M. C. Newton, S. Firth, T. Matsuura, and P. A. Warburton, '*Synthesis and characterisation of zinc oxide tetrapod nanocrystals*', J. Phys. Conf. Ser. **26**, 251 (2006).

[2] M. C. Newton, S. Firth, and P. A. Warburton, '*Ultraviolet Photoresponse of ZnO tetrapod nanocrystal Schottky diodes*', Proc. IEEE Conf. Nano. 2006 (**2**), 453 .

[3] *M. C. Newton, S. Firth, and P. A. Warburton, 'ZnO tetrapod Schottky photodiodes', Appl. Phys. Lett.* ***89****, 072104 (2006).*
This paper was also selected for publication in the *Virtual Journal of Nanoscale Science and Technology* **14**(9), 2006.